Cell Journal (Yakhteh)

Guide for Authors

Aims and Scope: The "Cell Journal (Yakhteh)" is a peer review and monthly English publication of Royan Institute of Iran. The aim of the journal is to disseminate information by publishing the most recent scientific research studies based on medical and developmental biology including cell therapy and regenerative medicine, stem cell biology reproductive medicine, medical genetics, immunology, oncology, clinical biochemistry, neuroscience, and tissue engineering. **Cell J**, has been certified by the Ministry of Culture and Islamic Guidance since 1999 and accredited as a scientific and research journal by HBI (Health and Biomedical Information) Journal Accreditation Commission since 2000 which is an open access journal. **This journal holds the membership of the Committee on Publication Ethics (COPE).**

1. Types of articles

The articles in the field of Cellular and Molecular can be considered for publications in **Cell J.** These articles are as below:

A. Original articles

Original articles are scientific reports of the original research studies. The article consists of English Abstract (structured), Introduction, Materials and Methods, Results, Discussion, Conclusion, Acknowledgements, Author's Contributions, and References **(Up to 40).**

B. Review articles

Review articles are the articles written by well experienced authors and those who have excellence in the related fields. The corresponding author of the review article must be one of the authors of at least three published articles appearing in the references. The review article consists of English Abstract (unstructured), Introduction, Conclusion, Author's Contributions, and References **(Up to 90).**

C. Systematic Reviews

Systematic reviews are a type of literature review that collect and critically analyzes multiple research studies or papers. The Systematic reviews consist of English Abstract (unstructured), Introduction, Materials and Methods, Results, Discussion, Conclusion, Acknowledgements, Author's Contributions, and References **(Up to 90).**

D. Short communications

Short communications are articles containing new findings. Submissions should be brief reports of ongoing researches. The short communication consists of English Abstract (unstructured), the body of the manuscript (should not hold heading or subheading), Acknowledgements, Author's Contributions, and References **(Up to 30).**

E. Case reports

Case reports are short discussions of a case or case series with unique features not previously described which make an important teaching point or scientific observation. They may describe novel techniques or use equipment, or new information on diseases of importance. It consists of English Abstracts (Unstructured), Introduction, Case Report, Discussion, Acknowledgements, Author's Contributions, and References **(Up to 30).**

F. Editorial

Editorials are articles should be written in relevant and new data of journals' filed by either the editor in chief or the editorial board.

G. Imaging in biology

Images in biology should focus on a single case with an interesting illustration such as a photograph, histological specimen or investigation. Color images are welcomed. The text should be brief and informative.

H. Letter to the editors

Letter to the editors are in response to previously published **Cell J** articles, and may also include interesting cases that do not meet the requirement of being truly exceptional, as well as other brief technical or clinical notes of general interest.

I. Debate

Debates are articles which show a discussion of the positive and negative view of the author concerning all aspect of the issue relevant to scientific research.

2. Submission process

It is recommended to see the guidelines for reporting different kinds of manuscripts. This guide explains how to prepare the

manuscript for submission. Before submitting, we suggest authors to familiarize themselves with **Cell J** format and content by reading the journal via the website (www.celljournal.com). The corresponding author ensures that all authors are included in the author list and agree with its order, and they must be aware of the manuscript submission.

A. Author contributions statements

It is essential for authors to include a statement of responsibility in the manuscript that specifies all the authors' contributions. This participation must include: Conceptualization, Methodology, Software, Validation, Formal analysis, Investigation, Resources, Data Curation, Writing - Original Draft, Writing - Review & Editing, Visualization, Supervision, Project administration, and Funding acquisition. Authors who do not meet the above criteria should be acknowledged in the Acknowledgments section.

B. Cover letter and copyright

Each manuscript should be accompanied by a cover letter, signed by all authors specifying the following statement: "The manuscript has been seen and approved by all authors and is not under active consideration for publication. It has neither been accepted for publication nor published in another journal fully or partially (except in abstract form). **Also, no manuscript would be accepted in case it has been pre-printed or submitted to other websites.** I hereby assign the copyright of the enclosed manuscript to **Cell J.**" The corresponding author must confirm the proof of the manuscript before online publishing. It is needed to suggest three peer reviewers in the field of their manuscript.

C. Manuscript preparation

Authors whose first language is not English encouraged to consult a native English speaker in order to confirm his manuscripts to American or British (not a mixture) English usage and grammar. It is necessary to mention that we will check the plagiarism of your manuscript by iThenticate Software. The manuscript should be prepared in accordance with the "International Committee of Medical Journal Editors (ICMJE)". Please send your manuscript in two formats word and PDF (including: title, name of all the authors with their degree, abstract, full text, references, tables and figures) and also send tables and figures separately in the site. The abstract and text pages should have consecutive line numbers in the left margin beginning with the title page and continuing through the last page of the written text. Each abbreviation must be defined in the abstract and text when they are mentioned for the first time. Avoid using abbreviation in the title. Please use the international and standard abbreviations and symbols

It should be added that an essential step toward the integration and linking of scientific information reported in published literature is using standardized nomenclature in all fields of science and medicine. Species names must be italicized (*e.g., Homo sapiens*) and also the full genus and species written out in full, both in the title of the manuscript and at the first mention of an organism in a paper.

It is necessary to mention that genes, mutations, genotypes, and alleles must be indicated in italics. Please use the recommended name by consulting the appropriate genetic nomenclature database, e.g., HUGO for human genes. In another words; if it is a human gene, you must write all the letters in capital and italic (*e.g., OCT4, c-MYC*). If not, only write the first letter in capital and italic (*e.g., Oct4, c-Myc*). **In addition, protein designations are the same as the gene symbol but are not italicized.**

Of note, Cell J will only consider publishing genetic association study papers that are novel and statistically robust. Authors are advised to adhere to the recommendations outlined in the STREGA statement (http://www.strega-statement.org). The following criteria must be met for all submissions:

1. Hardy-Weinberg Equilibrium (HWE) calculations must be carried out and reported along with the P-values if applicable [see Namipashaki et al. 2015 (Cell J, Vol 17, N 2, Pages: 187-192) for a discussion].

2. Linkage disequilibrium (LD) structure between SNPs (if multiple SNPs are reported) must be presented.

3. Appropriate multiple testing correction (if multiple independent SNPs are reported) must be included.

Submissions that fail to meet the above criteria will be rejected before being sent out for review.

Each of the following manuscript components should begin in the following sequence:

Authors' names and order of them must be carefully considered (full name(s), highest awarded academic degree(s), email(s), and institutional affiliation(s) of all the authors in English. Also, you must send mobile number and full postal address of the corresponding author).

Changes to Authorship such as addition, deletion or rearrangement of author names must be made only before the manuscript has been accepted in the case of approving by the journal editor. In this case, the corresponding author must explain the reason of changing and confirm them (which has been signed by all authors of the manuscript). If the manuscript has already been published in an online issue, an erratum is needed. Please contact us via info@celljournal.org in case of any changes (corrections, retractions, erratum, etc.).

Title is providing the full title of the research (do not use abbreviations in title).

Running title is providing a maximum of 7 words (no more than 50 characters).

Abstract must include Objective, Materials and Methods, Results, and Conclusion (no more than 300 words).

Keywords, three to five, must be supplied by the authors at the foot of the abstract chosen from the Medical Subject Heading (MeSH). Therefore; they must be specific and relevant to the paper.

The following components should be identified after the abstract:

Introduction: The Introduction should provide a brief background to the subject of the paper, explain the importance of the study, and state a precise study question or purpose.

Materials and Methods: It includes the exact methods or observations of experiments. If an apparatus is used, its manufacturer's

name and address should be stipulated in parenthesis. If the method is established, give reference but if the method is new, give enough information so that another author can perform it. If a drug is used, its generic name, dose, and route of administration must be given. Standard units of measurements and chemical symbols of elements do not need to be defined.

Statistical analysis: Type of study and statistical methods should be mentioned and specified by any general computer program used.

Ethical considerations*:* Please state that informed consent was obtained from all human adult participants and from the parents or legal guardians of minors and include the name of the appropriate institutional review board that approved the project. It is necessary to indicate in the text that the maintenance and care of experimental animals complies with National Institutes of Health guidelines for the humane use of laboratory animals, or those of your Institute or agency.

Clinical trial registration: All of the Clinical Trials performing in Iran must be registered in Iranian Registry of Clinical Trials (www.irct.ir). The clinical trials performed abroad, could be considered for publication if they register in a registration site approved by WHO or www.clinicaltrials.gov. If you are reporting phase II or phase III randomized controlled trials, you must refer to the CONSORT Statement for recommendations to facilitate the complete and transparent reporting of trial findings. Reports that do not conform to the CONSORT guidelines may need to be revised before peer-reviewing.

Results: They must be presented in the form of text, tables, and figures. Take care that the text does not repeat data that are presented in tables and/or figures. Only emphasize and summarize the essential features of the main results. Tables and figures must be numbered consecutively as appeared in the text and should be organized in separate pages at the end of the manuscript while their location should be mentioned in the main text.

Tables and figures: If the result of your manuscript is too short, it is better to use the text instead of tables & figures. Tables should have a short descriptive heading above them and also any footnotes. Figure's caption should contain a brief title for the whole figure and continue with a short explanation of each part and also the symbols used (no more than 100 words). All figures must be prepared based on cell journal's guideline in color (no more than 6 Figures and Tables) and also in TIF format with 300 DPI resolution.

Of Note: Please put the tables & figures of the result in the results section not any other section of the manuscript.

Supplementary materials would be published on the online version of the journal. This material is important to the understanding and interpretation of the report and should not repeat material within the print article. The amount of supplementary material should be limited. Supplementary material should be original and not previously published and will undergo editorial and peer review with the main manuscript. Also, they must be cited in the manuscript text in parentheses, in a similar way as when citing a figure or a table. Provide a caption for each supplementary material submitted.

Discussion: It should emphasize the present findings and the variations or similarities with other researches done by other researchers. The detailed results should not be repeated in the discussion again. It must emphasize the new and important aspects of the study.

Conclusion: It emphasizes the new and important aspects of the study. All conclusions are justified by the results of the study.

Acknowledgements: This part includes a statement thanking those who contributed substantially with work relevant to the study but does not have authorship criteria. It includes those who provided technical help, writing assistance and name of departments that provided only general support. You must mention financial support in the study. Otherwise; write this sentence "There is no financial support in this study".

Conflict of interest: Any conflict of interest (financial or otherwise) and sources of financial support must be listed in the Acknowledgements. It includes providers of supplies and services from a commercial organization. Any commercial affiliation must be disclosed, regardless of providing the funding or not.

Of Note: If you have already any patent related to the subject of your manuscript, or you are going to apply for such a patent, it must be mentioned in this part.

References: The references must be written based on the Vancouver style. Thus the references are cited numerically in the text and listed in the bibliography by the order of their appearance. The titles of journals must be abbreviated according to the style used in the list of Journals Indexed in PubMed. Write surname and initials of all authors when there are six or less. In the case of seven or more authors, the names of the first six authors followed by "et al." must be listed. You can download Endnote file for Journal references style: endnote file

The reference of information must be based on the following order:

Article:

Surname(s) and first letter of name &middle name(s) of author(s) .Manuscript title. Journal title (abbr).publication date (year); Volume & Issue: Page number.

Example: Manicardi GC, Bianchi PG, Pantano S, Azzoni P, Bizzaro D, Bianchi U, et al. Presence of endogenous nicks in DNA of ejaculated human spermatozoa and its relationship to chromomycin A3 accessibility. Biol Reprod. 1995; 52(4): 864-867.

Book:

Surname(s) and first letter of name & middle name(s) of author(s).Book title. Edition. Publication place: publisher name; publication date (year); Page number.

Example: Edelman CL, Mandle CL. Health promotion throughout the lifespan. 2nd ed. ST Louis: Mosby; 1998; 145-163.

Chapter of book:

Surname(s) and first letter of name & middle name(s) of author(s).Chapter title. In: Surname(s) and first letter of name & middle name(s) of editor(s), editors. Book title. Edition. Publication place: publisher name; publication date (year); Page number.

Example: Phillips SJ, Whisnant JP. Hypertension and stroke. In: Laragh JH, Brenner BM, editors. Hypertension: pathophysiology, diagnosis, and management. 2nd ed. New York: Raven Press; 1995; 465-478.

Abstract book:

Example: Amini rad O.The antioxidant effect of pomegranate juice on sperm parameters and fertility potential in mice. Cell J. 2008;10 Suppl 1:38.

Thesis:

Name of author. Thesis title. Degree. City name. University. Publication date (year).

Example: Eftekhari Yazdi P. Comparison of fragment removal and co-culture with Vero cell monolayers on development of human fragmented embryos. Presented for the Ph.D., Tehran. Tarbiyat Modarres University. 2004.

Internet references

Article:

Example: Jahanshahi A, Mirnajafi-Zadeh J, Javan M, Mohammad-Zadeh M, Rohani M. Effect of low-frequency stimulation on adenosineA1 and A2A receptors gene expression in dentate gyrus of perforant path kindled rats. Cell J. 2008; 10 (2): 87-92. Available from: http://www.celljournal.org. (20 Oct 2008).

Book:

Example: Anderson SC, Poulsen KB. Anderson's electronic atlas of hematology.[CD-ROM]. Philadelphia: Lippincott Williams & Wilkins; 2002.

D. Proofs are sent by email as PDF files and should be checked and returned within 72 hours of receipt. It is the authors' responsibility to check that all the text and data as contained in the page proofs are correct and suitable for publication. **We are requested to pay particular attention to author's names and affiliations as it is essential that these details be accurate when the article is published.**

E. Pay for publication: Publishing an article in **Cell J** requires Article Processing Charges (APC) that will be billed to the submitting author following the acceptance of an article for publication. For more information please see www.celljournal.org.

F. Ethics of scientific publication: Manuscripts that have been published elsewhere with the same intellectual material will refer to duplicate publication. If authors have used their own previously published work or work that is currently under review, as the basis for a submitted manuscript, they are required to cite the previous work and indicate how their submitted manuscript offers novel contributions beyond those of the previous work. Research and publication misconduct is considered a serious breach of ethics.

The Journal systematically employs iThenticate, plagiarism detection and prevention software designed to ensure the originality of written work before publication. Plagiarism of text from a previously published manuscript by the same or another author is a serious publication offence. Some parts of text may be used, only where the source of the quoted material is clearly acknowledged.

3. General information

A. You can send your manuscript via online submission system which is available on our website. If the manuscript is not prepared according to the format of **Cell J**, it will be returned to authors.

B. The order of article appearance in the Journal is not demonstrating the scientific characters of the authors.

C. Cell J has authority to accept or reject the manuscript.

D. Corresponding authors should send the manuscripts via the Online Manuscript Submission System. All submissions will be evaluated by the associated editor in order to check scope and novelty. If the manuscript suits the journal criteria, the associated editor would select the single-blind peer-reviewers. The reviewers of the manuscript must not share information about the review with anyone without permission of the editors and authors. If three reviewers pass their judgments on the manuscript, it will be presented to the associated editor of **Cell J**. In the case of having a favorable judgment on the manuscript, reviewers' comments will be presented to the corresponding author (the identification of the reviewers will not be revealed). After receiving the revision, the associated editor would choose the final reviewer among the previous ones. The final decision will be taken by editor-in-chief based on the final reviewer's comments. The review process takes between 2 to 4 months in **Cell J**. The executive member of journal will contact the corresponding author directly within 3-4 weeks by email. If authors do not receive any reply from journal office after the specified time, they can contact the journal office. Finally, the executive manager will respond promptly to authors' request.

After receiving the acceptance letter, the abstract of the paper would be published electronically. The paper will be in a queue to be published in one Cell J. At last, the corresponding author should verify a proof copy of the paper in order to be published.

The Final Checklist

The authors must ensure that before submitting the manuscript for publication, they have to consider the following parts:

1. The first page of manuscript should contain title, name of the author/coauthors, their academic qualifications, designation & institutions they are affiliated with, mailing address for future correspondence, email address, phone, and fax number.

2. Text of manuscript and References prepared as stated in the "guide for authors" section.

3. Tables should be on a separate page. Figures must be sent in color and also in JPEG (Jpg) format.

4. Cover Letter should be uploaded with the signature of all authors.

5. An ethical committee letter should be inserted at the end of the cover letter.

The Editor-in-Chief: Ahmad Hosseini, Ph.D.

Cell Journal *(Yakhteh)*

P.O. Box: 16635-148, Iran

Tel/Fax: + 98-21-22510895

Emails: info@celljournal.org

journals@celljournal.org

Dr. Saeed Kazemi Ashtiani

IN THE NAME OF GOD

Gone But not Forgotten

In the memory of the late Director of Royan Institute, Founder of Stem Cells Research in Iran and Chairman of ***Cell Journal*** *(Yakhteh)*. May he rest in peace.

PUBLISHED & SPONSORED BY:
Publication of Royan Institute (ACECR)

Indexed in:
1. Thomson Reuters (ISI)
2. PubMed
3. PubMed Central (PMC)
4. National Library Medicine (NLM)
5. Biosis Preview
6. Index Medicus for the Eastern Mediterranean Region (IMEMR)
7. Regional Information Center for Sciences and Technology (RICeST)
8. Index Copernicus International
9. Cambridge Scientific Abstract (CSA)
10. EMBASE
11. Scopus
12. Cinahl Database
13. Google Scholar
14. Chemical Abstract Service (CAS)
15. Proquest
16. Directory of Open Access Journals (DOAJ)
17. Open Academic Journals Index (OAJI)
18. Directory of Research Journals Indexing (DRJI)
19. Scientific Information Database (SID)
20. Iranmedex
21. Islamic World Science Citation Center (ISC)
22. Magiran
23. Science Library Index
24. Biological Abstracts
25. Essential Science Indicators
26. EuroPub

Editorial Office Address (Dr. Ahmad Hosseini):
Royan Institute, P.O.Box: 16635-148,
Tehran, Iran
Tel & Fax: (+9821)22510895
Website: www.celljournal.org
Emails: info@celljournal.org
journals@celljournal.org

Printing Company:
Naghshe e Johar Co.
No. 103, Fajr alley, Tehranpars Street,
Tehran, Iran.

Cell Journal$_{(Yakhteh)}$, Vol 25, No 1, January 2023, Serial Number: 108, Pages: 1-75

CONTENTS

Original Articles

Letter to The Editor

Cell J
Cell Journal(Yakhteh) Homepage: https://www.celljournal.org/
Original Article Vol 25, No 1, January 2023, Pages: 1-10

Expression of Long Non-Coding RNA *H19* in Acute Lymphoblastic Leukemia

Marjan Asadi, M.Sc.[1], Mohammad Ali Gholampour, Ph.D.[2], Farzad Kompani, M.D.[3], Shaban Alizadeh, Ph.D.[1]*

1. Hematology Department, School of Allied Medicine, Tehran University of Medical Science, Tehran, Iran
2. Hematology Department, Faculty of Medical Sciences, Tarbiat Modares University, Tehran, Iran
3. Division of Hematology and Oncology, Children's Medical Center, Pediatrics Center of Excellence, Tehran University of Medical Science, Tehran, Iran

**Corresponding Address: P.O.Box: 1417935840, Hematology Department, School of Allied Medicine, Tehran University of Medical Science, Tehran, Iran*
Email: alizadehs@tums.ac.ir

Received: 12/October/2021, Revised: 05/March/2022, Accepted: 26/April/2022

Abstract

Objective: Long non-coding RNA (lncRNA) H19 has essential roles in growth, migration, invasion, and metastasis of most cancers. H19 dysregulation is present in a large number of solid tumors and leukemia. However, the expression level of H19 in acute lymphoblastic leukemia (ALL) has not been elucidated yet. The current study aimed to explore *H19* expression in ALL patients and cell lines.

Materials and Methods: This experimental study was conducted in bone marrow (BM) samples collected from 25 patients with newly diagnosed ALL. In addition, we cultured the RPMI-8402, Jurkat, Ramos, and Daudi cell lines and assessed the effects of internal (hypoxia) and external (chemotherapy medications L-asparaginase [ASP] and vincristine [VCR]) factors on *h19* expression. The expressions of *H19*, *P53*, *c-Myc*, *HIF-1α* and *β-actin* were performed using quantitative real-time polymerase chain reaction (qRT-PCR) method.

Results: There was significantly increased *H19* expression in the B-cell ALL (B-ALL, P<0.05), T-cell ALL (T-ALL, P<0.01) patients and the cell lines. This upregulation was governed by the *P53*, *HIF-1α*, and *c-Myc* transcription factors. We observed that increased *c-Myc* expression induced *H19* expression; however, *P53* adversely affected *H19* expression. In addition, the results indicated that chemotherapy changed the gene expression pattern. There was a considerable decrease in *H19* expression after exposure to chemotherapy medications; nonetheless, hypoxia induced *H19* expression through *P53* downregulation.

Conclusion: Our findings suggest that *H19* may have an important role in pathogenesis in ALL and may act as a promising and potential therapeutic target.

Keywords: Acute Lymphoblastic Leukemia, lncRNA, H19, Hypoxia

Citation: **Asadi M, Gholampour MA, Kompani F, Alizadeh Sh. Expression of long non-coding RNA H19 in acute lymphoblastic leukemia. Cell J. 2023; 25(1): 1-10. doi: 10.22074/cellj.2022.8315.**

Introduction

Acute lymphoblastic leukemia (ALL) is the most prevalent leukemia in childhood. It is characterized by overproduction and accumulation of lymphoblasts in the bone marrow (BM) (1). In addition, ALL relapse is the fundamental cause of treatment failure in 15-20% of patients (2, 3). Therefore, the exploration of novel functional molecules that play a role in ALL pathogenesis could be effective therapeutic targets for this disease.

Long non-coding RNAs (lncRNAs) are non-protein-coding transcripts longer than 200 nucleotides. The results from recent studies have revealed various functions of lncRNAs in molecular mechanisms of biological and pathological processes (4-7). H19 was the first lncRNA to be discovered and submitted for genomic imprinting (8-10). H19 has a role in embryogenesis and tumorigenesis (11). H19 acts as a molecular sponge for miRNA-138 and miRNA-200a, the precursors of microRNA675 , which interact with epigenetic polycomb proteins. H19 has an indispensable role in enhancing cell proliferation, differentiation, migration, invasion, and chemoresistance (12, 13). Initially, H19 was reported to be a tumor suppressor (14, 15), however, recent evidence has shown that H19, as an oncogene, is overexpressed in breast (16-18), liver (18), endometrial (19), lung, cervical, and esophageal cancers (5). A similar pattern of H19 expression is observed in various types of leukemia, including chronic myeloid leukemia (CML) (20, 21) and acute myeloid leukemia (AML) (22), as well. These observations together suggest dual roles for H19 as an oncogene or a tumor suppressor in various cancers (20). Therefore, future studies could evaluate the potential for lncRNAs as therapeutic targets or prognostic biomarkers in cancer treatments (23).

According to previous studies, some transcriptional factors can regulate and change the molecular functions of H19. For instance, c-Myc is a transcriptional factor that plays an oncogenic role through attaching to conserved E-boxed in the vicinity of the imprinting control region (ICR), to induce acetylation of histones and the H19 promoter. c-Myc induces H19

expression and may contribute to tumor etiology or function as an oncogene (12, 24, 25). c-Myc was first identified in Burkitt's lymphoma. Its activation is caused by a chromosomal translocation. However, deregulation of c-Myc expression has been observed along with poor patient survival in numerous human cancers, including carcinomas of the prostate, breast, lung, as well as leukemia, and lymphoma (26). Conversely, H19 and p53 mutually counter-regulate each other (27). The p53 tumor suppressor is a transcriptional factor that regulates various anti-proliferative processes and downregulates H19 expression by inducing DNA demethylation at the ICR of H19 (28-30). Various physiological processes such as cell metabolism, survival, proliferation, and angiogenesis play crucial roles in pathological scenarios (31, 32). A hypoxic region is present in ALL BM, and it is considered to be a determinative factor for both a therapeutic response and tumor progression. A complicated cellular network of genes is involved in tumor progression (33). Researchers have reported that H19 is a part of this network because its expression could be upregulated in hypoxic stress (34, 35). HIF-1α is a crucial factor responsible for H19 induction under hypoxic conditions and acts as a p53 inhibitor, leading to tumor growth. Hypoxia can indirectly upregulate H19 expression by inhibition of p53 (24, 35).

H19 is overexpressed in various cancerous tissues and has been shown to be associated with carcinogenesis, cell proliferation and differentiation, metastasis, poor prognosis, and tumor growth in various cancers, while normal expression of H19 has been shown in healthy individuals. This LncRNA may act as a novel diagnostic and prognostic marker for malignancies.

Material and Methods

Cell lines and patient samples

In this experimental study, we cultured the RPMI-8402, Jurkat, Ramos, and Daudi cell lines inRPMI-1640 (Gibco Life Technique, Germany) with 10 % heat-inactivated fetal bovine serum (FBS, Sigma-Aldrich, USA), 100 U/ml penicillin, and 100 µg/ml streptomycin. The cells were maintained in a humidified incubator with 5% CO_2 at 37°C. We purchased cell lines from National Cell Bank of Iran (NCBI, Pasteur Institute of Iran, Tehran, Iran). The patient samples were collected from BM of 25 newly diagnosed ALL individuals, 15 with B-ALL and 10 with T-ALL, and 20 healthy donors admitting to the Children's Medical Center, Tehran, Iran. The medical Ethics Committee of Tehran University (IR.TUMS.REC.1394.2201) permitted this study.

B and T cell isolation

BM from both healthy donors and patients were collected in EDTA tubes and mononuclear cells of BM (BM-MNCs) were isolated through Ficoll-Hypaque (Lymphodex, Germany). The isolated cells were magnetically labeled with Anti- CD3 and CD19 MACS MicroBeads (Miltenyi Biotech, Germany). Next, the samples were washed using 1-2 mL of phosphate-buffered saline (PBS) buffer per 10^6 cells and subsequently centrifuged for 10 minutes at 300x g. The cell suspension was placed onto the separation column and the flow-through that contained the unlabeled cell was collected. The column was then removed and the retained cells were washed, collected and considered as a positively selected cell fraction. The isolated cells from healthy individuals were considered to be the control group for evaluation of gene expression in patients with ALL.

Flow cytometry analysis

Flow cytometry analysis was conducted to assess the purity of the isolated B and T cells using CD19-FITC and CD3-PE-conjugated antibodies, respectively (ebioscience, Thermo Fisher Science, USA). The antibody binding step was performed for 45 minutes at 4°C in the dark. Afterward, the cells were resuspended in 100 µl of 0.5% PBS. The analysis was carried out by a flow cytometer (FACScalibur, Becton Dickenson, MA, USA).

RNA extraction and quantitative real-time polymerase chain reaction

Total RNA was extracted using RNeasy Mini Kit (Qiagen, Hilden, Germany) according to manufacturer's instruction. Next, using the revert Aid First-Strand cDNA Kit (Fisher Scientifiec, MA, USA) protocol cDNA was synthesized. Applied Biosystem 7300 real-time PCR System (Applied Biosystem, Foster City, USA) was used for quantitative real-time polymerase chain reaction (qRT-PCR). The following primers were used for qPCR:

H19 sense: 5′-TGTTTCTTTACTTCCTCCACGG-3′
antisense: 5′- TTCCTCTAGCTTCACCTTCCAG-3′
c-Myc sense: 5′-TTCGGGTAGTGGAAAACCAG-3′
antisense: 5′-AGTAGAAATACGGCTGCACC-3′
P53 sense: 5′- TCAACAAGATGTTTTGCCAACTG-3′
antisense: 5′- ATGTGCTGTGACTGCTTGTAGATG-3′
HIF1-α sense: 5′- TTCACCTGAGCCTAATAGTCC-3′
antisense: 5′- CAAGTCTAAATCTGTGTCCTG-3′
β-actin sense: 5′- TGAAGATCAAGATCATTGCTCCTC-3′
antisense: 5′- AGTCATAGTCCGCCTAGAAGC-3′

β-actin was used for normalization. Relative gene expression was calculated based on $2^{-\Delta\Delta CT}$ method. All experiments had three technical replicates.

Hypoxia treatment

ALL cell lines were cultured for 24 hours at 37°C in an anaerobic incubator (Ruskin Technologies, Pencoed, Wales, UK) with constant hypoxic environment (2% O_2, 93% N_2, and 5% CO_2) and 90% humidity. The time of inducing hypoxic condition was selected based on previous studies (36). The cell lines cultured under Normoxia conditions were incubated in 5% CO_2 at 37°C.

Treatment with chemotherapy drugs and dose selection

The effects of the chemotherapy drugs L-asparaginase (ASP, Paronal, Christiaens, The Netherlands) and vincristine (VCR, TEVA Pharma, Utrecht, The Netherlands) were assessed on *h19*, *c-myc*, *p53*, and *hif-1α* expressions in all of the cell lines. The logarithmic ranges of drugs were selected based on previous studies (2, 3). We used the 25-200 ng/mL doses of ASP and 2-16 ng/mL doses of VCR in our experiments to determine the lethal concentration of 50% (LC50%). Next, we assessed the target gene expressions in the ALL cell lines.

MTT assay

Cell viability was performed by dimethylthiazol diphenyl tetrazolium bromide (MTT, Sigma, Chemical, St Louis, MO, USA). ALL cell lines were treated with VCR (25-200 ng/mL) and ASP (2-16 ng/mL) as mentioned above. Untreated cell lines were cultured as the control groups. After 48 hours, a standard concentration of MTT (10 µM) was added to every well and then 100 µM of dimethyl sulfoxide (DMSO) was added to dissolve the formazan. The optical density was evaluated using a microplate reader (Anthos2020, Salzburg, Austria) at 570 nm.

Annexin V-fluorescein staining assay

After treatment with the chemotherapy drugs, we used BioscienceTM Annexin V-FITC Apoptosis in the ALL cell lines. Briefly, the cells were washed with phosphate-buffered saline (PBS) and stained with propidium iodide (PI) and Annexin V (FITC) for 20 minutes at room temperature. The samples were analyzed by a flow cytometer (FACScalibur, Becton Dickenson, MA, USA) with 10000 events acquired for each sample.

Statistical analysis

All data are presented as standard deviation (SD). We used Mann-Whitney U test to analyze two independent samples of patients' data. A Mann-Whitney test is used when we have a continuous level variable measured for all observations in two groups and we want to test if the distribution of this variable is different in the two groups but we are unable to assume normality in both groups. Statistical analysis were done with student's test for differences in each two-group comparison and one-way ANOVA was used to determine the differences among at least three groups. GraphPad Prism, version 6.07 (GraphPad Software, USA) was used for statistical analysis. A $P<0.05$ was defined as statistically significant.

Results

H19 expression was upregulated in T and B lymphocytes from ALL patients

In this study 25 patients were enrolled. In experimental group, there were 17 males (68%) and 8 females (32%). In the control group, there were 11 males (55%) and 9 females (45%). The *H19* expression levels in B-ALL and T-ALL cases were 2.51 (1.81 to 4.12) and 4.72 (2.71 to 9.48), respectively (Fig.1A). Our findings showed that *H19* expression was higher in the experimental B-ALL ($P<0.05$) and T-ALL ($P<0.01$) samples in comparison to the control group. The BM microenvironment in ALL is hypoxic; a condition that controls the expressions of other genes, particularly *H19*. Therefore, we assessed *HIF-1α* expression in patients and healthy samples. The results showed a significantly high *HIF-α* expression in B-ALL (12 folds, $P<0.01$) and T-ALL (8 folds, $P<0.001$) patients compared to the control group (Fig.1B). Because *H19* and *c-Myc,* as well as *P53,* are frequently co-amplified in cancer, we examined the expression levels of *c-Myc* and *P53* in the ALL patients and healthy subjects. *P53* expression was downregulated in both B-ALL (0.4-fold, ns) and T-ALL (0.3-fold, $P<0.01$) patients along with upregulation of *c-Myc* in B-ALL (3-fold, $P<0.01$) and T-ALL (7-fold, $P<0.001$) patients (Fig.1C, D). In addition, as seen in Supplementary section, flow cytometry analysis of isolated T and B lymphocytes showed that T cells expressed CD3 (98.3%) and B cells expressed CD19 (88.7%) as control groups. Clinical sample characteristics are summarized in Table 1.

Table 1: The demographic and clinicopathologic characteristics of newly diagnosed ALL patients (25 patients)

Clinical factor	Numbers/Percentage
Male	17 (68.0)
Female	8 (32.0)
Median age (Y)	28 (6-30)
BM blast	81 (20-95)
Median WBC (10^6/µl)	19000 (700-400000)
Immunophenotype B-ALL	15 (60.0)
CD19+median	69.8
CD20+median	11.2
CD22+median	42.8
Cyto CD 79α	63.8
CD34+median	42.8
TdT+median	51.5
Immunophenotype T-ALL	10 (40.0)
CD2+median	96.1
CD3+median	75.9
CD5+median	85.1
CD7+median	88.5
CD34+median	60.4
TdT+median	53.0

Data are presented as n (%) or %. BM; Bone Marrow, WBC; White blood cell, B-ALL; B-cell acute lymphoblastic leukemia, and T-ALL; T-cell acute lymphoblastic leukemia.

H19 expression increased in ALL cell lines

We conducted an *in vitro* examination of *H19* in the B and T lymphocyte-derived cell lines. The *H19* expression levels in Jurkat and RPMI-8402 cells showed an almost equivalent increase in *H19* expression (4.8 folds, P<0.05, Fig.2A). Expression of *H19* in the B cell lines of Daudi and Ramos were 16 folds, P<0.01 and 6 folds, P<0.05, respectively (Fig.2B). This finding suggested that cell lines had higher *H19* expression compared with the B and T lymphocytes. We also evaluated *H19* expression under hypoxic conditions after 24 hours. Interestingly, we found elevated expression levels of *H19* in the T cell lines (about 4-folds, P<0.05) and B cell lines (at least 2-folds, Daudi ns, Ramous P<0.05, Fig.2C, D). To further assess the molecular mechanism of *H19* in ALL pathogenesis, we treated the cell lines with VCR and ASP drugs. Expression of *H19* decreased by (0.24-fold, P<0.05) and (0.4-fold, P<0.05) in the Jurkat and RPMI-8402 cells, and (0.22-fold, P<0.05) and (0.29-fold, P<0.01) in the Daudi and Ramous cells, respectively. Treatment with ASP caused an insignificant downregulation of *H19* expression in the ALL cell lines, with the exception of the Daudi cells (Fig.2E, F). These findings demonstrated that *H19* expression was declined in treated cell lines in comparison to untreated cells.

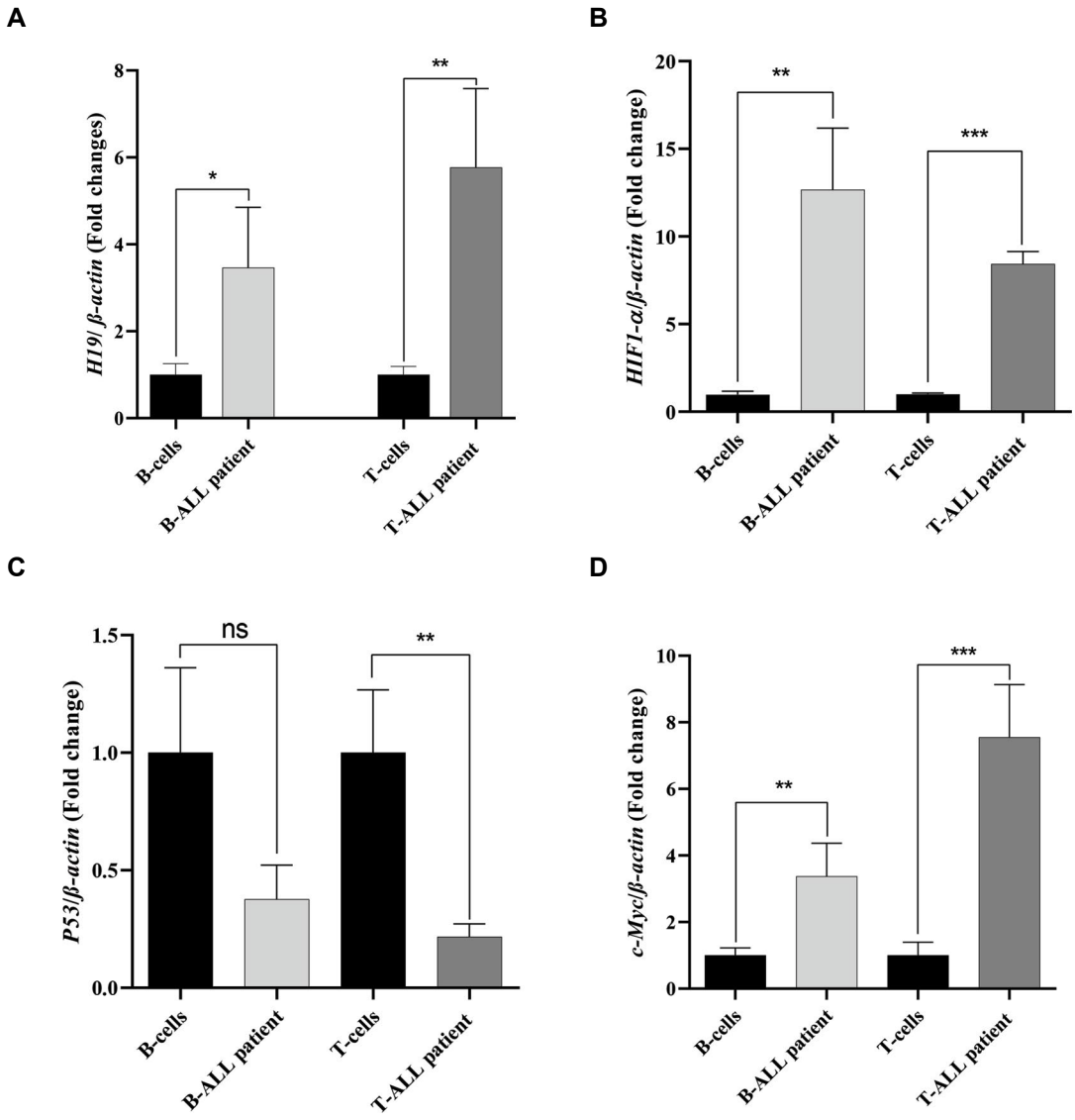

Fig.1: Gene expression in patients with ALL. All gene expressions were detected by quantitative real time PCR. T and B cells were extracted from B-ALL (n=15) and T-ALL (n=10) patients and compared with healthy donors (n=20) as the control group. **A.** *H19* expression in ALL patients and control group. **B.** *HIF-1α*, **C.** *P53*, and **D.** *c-Myc* expression levels in patient samples. Representative experiments performed in triplicate. The graphs demonstrate the standard deviation (SD). ALL; Acute lymphoblastic leukemia, B-ALL; B-cell acute lymphoblastic leukemia, T-ALL; T-cell acute lymphoblastic leukemia, PCR; Polymerase chain reaction, ns; Not significant, *; P<0.05, **; P<0.01, and ***; P<0.001.

Evaluation of cell line viability after culture in the presence of chemotherapy drugs

We used the MTT method to evaluate the viability of the cell lines with different doses and concentrations of VCR and ASP for 48 hours. The mean viability among the control and the treated groups was significant and is shown in Supplements. LC50 values were evaluated at the specific drug concentrations used for the cytotoxicity assay. To determine the effects of VCR and ASP on apoptosis of the ALL cell lines, we examined apoptotic cell death through AnnexinV and PI staining. The results showed that treatment with VCR and ASP induced apoptosis, as apoptosis was higher in the treated groups compared to the untreated cells (Fig.3).

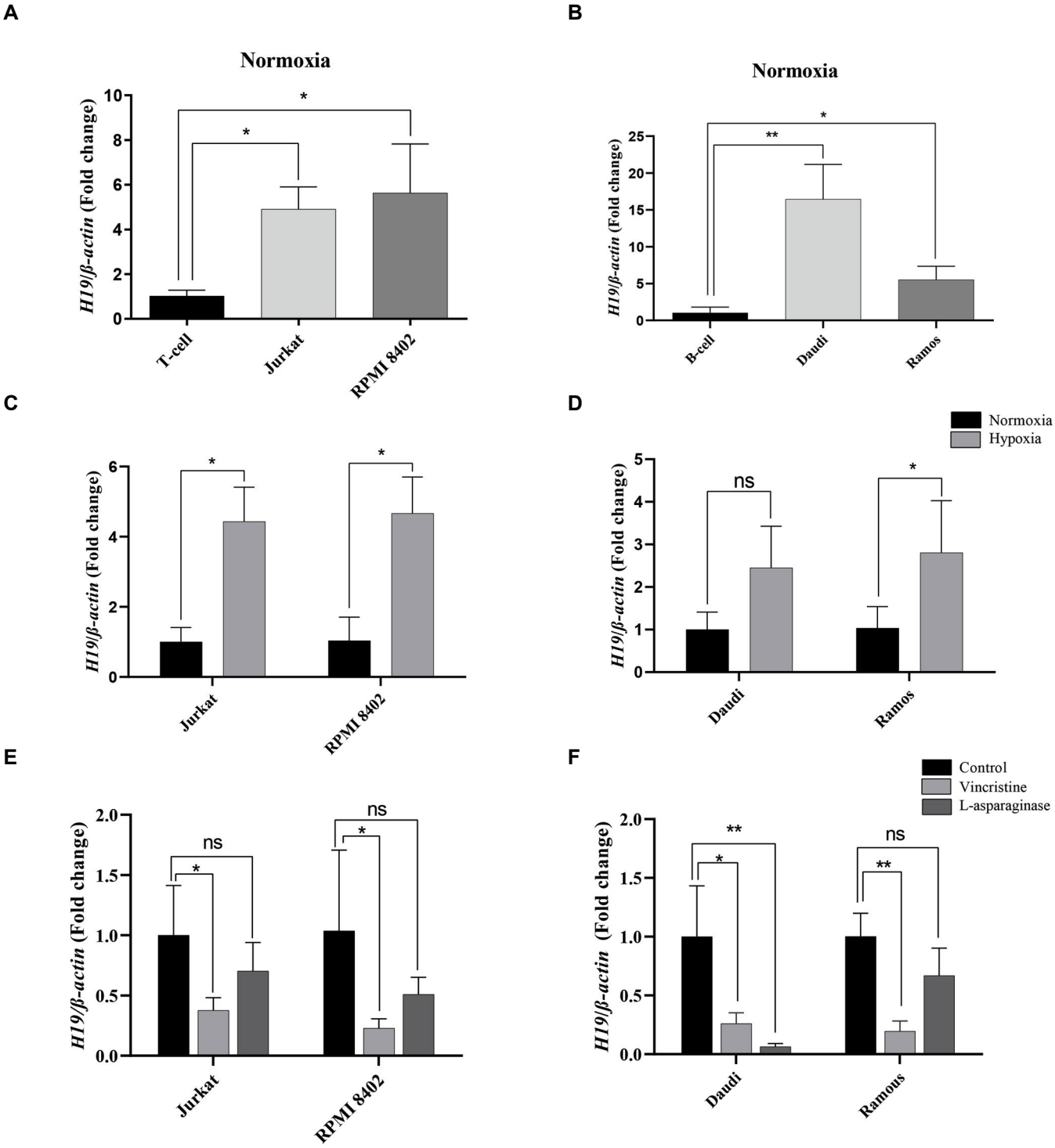

Fig.2: *H19* expression in ALL cell lines. Gene expression was assessed by q-RT PCR. **A, B.** *H19* expression was analyzed in both B and T ALL cell lines and compared to normal B and T cells, respectively. **C, D.** Analysis of *H19* expression in cell lines after 24 hours of exposure to hypoxic stress. **E, F.** Expression of *H19* was evaluated after treatment with VCR and ASP. The data are from three independent experiments, each done in triplicate. ALL; Acute lymphoblastic leukemia, q-RT PCR; Quantitative real-time polymerase chain reaction, VCR; Vincristine, ASP; L-asparaginase, ns; Not significant, *; P<0.05, and **; P<0.01.

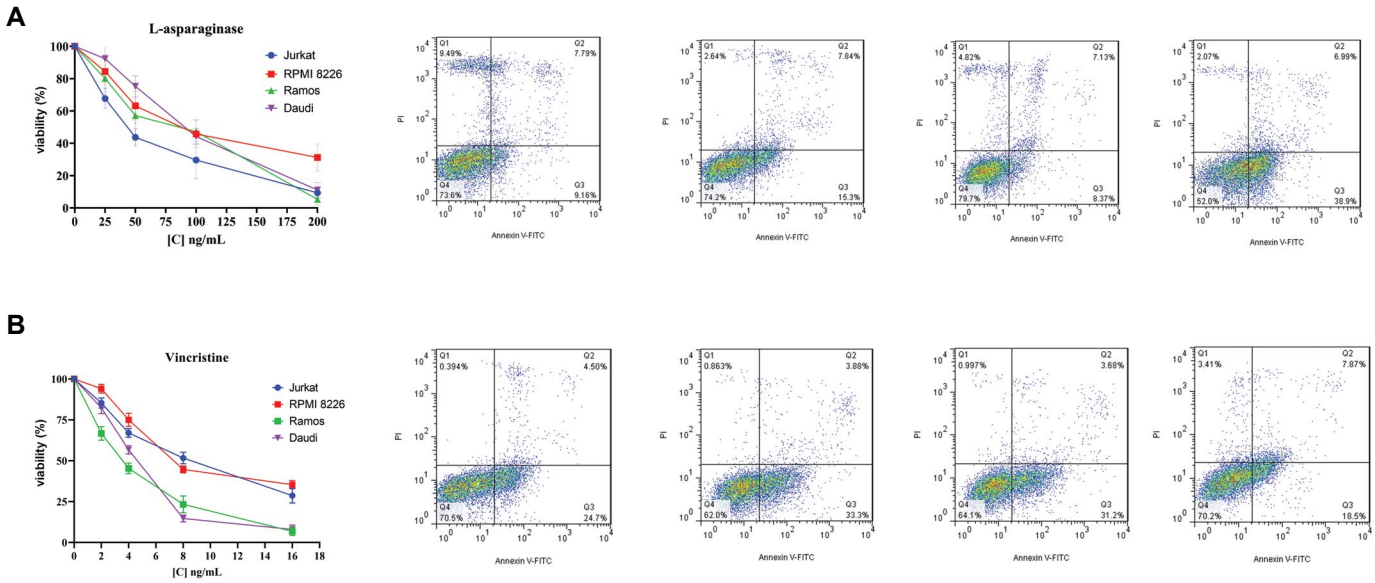

Fig.3: The effects of various doses of VCR and ASP on viability of ALL cell lines. **A.** MTT test was performed to investigate the survival of ALL cell lines at 48 hours after treatment with VCR and ASP. **B.** Staining with Annexin-V and PI assessed apoptosis. The histogram demonstrates the ratio of apoptotic or necrotic cells. Annexin V-/PI-, Annexin V+/PI-, Annexin V+, and PI+ represented live cells, early apoptotic cells, late apoptotic cells, necrotic cells, respectively. The data are from two independent experiments, each done in duplicate. VCR; Vincristine, ASP; L-asparaginase, ALL; Acute lymphoblastic leukemia, MTT; Dimethylthiazol diphenyl tetrazolium bromide, VCR; Vincristine, ASP; L-asparaginase, and PI; Propidium iodide.

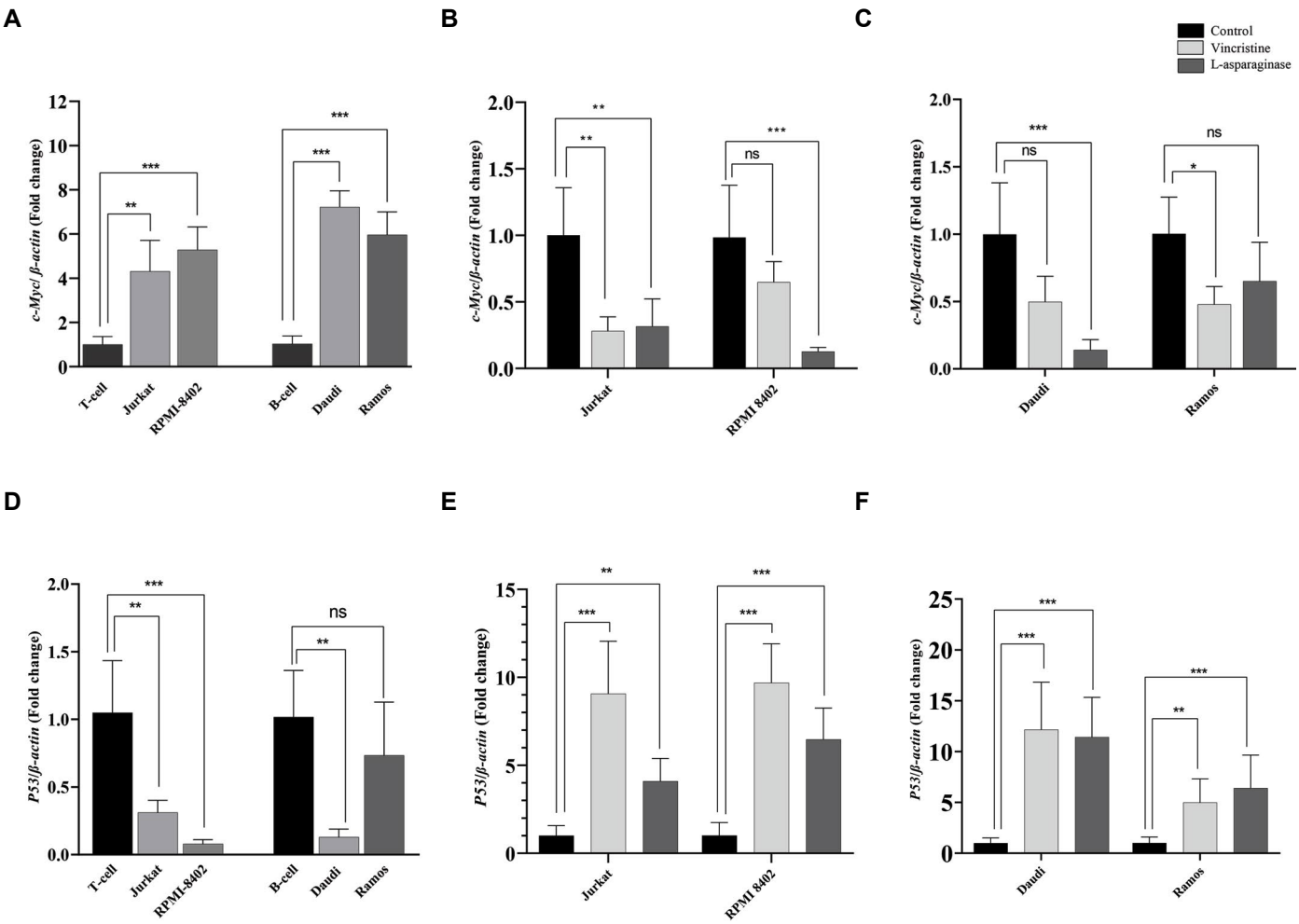

Fig.4: Expression of *H19*-related genes in the ALL cell lines. Gene expression was carried out through quantitative real-time PCR and the treated cell lines were compared with untreated controls. **A-C.** Expression of *c-Myc* was evaluated in B- and T- ALL cell lines and its relative expression was measured after a 48 hours of treatment with VIN and ASP. **D-F.** The relative expression levels of *P53* was measured in ALL cell lines and treated ones and compared to control group. The data are cultures from three independent experiments, each done in duplicate. ALL; Acute lymphoblastic leukemia, PCR; Polymerase chain reaction, VCR; Vincristine, ASP; L-asparaginase, ns; Not significant, *; P<0.05, **; P<0.01, and ***; P<0.001.

Expressions of related genes in the ALL cell lines

H19 expression is related to various genes, particularly *HIF-1α, P53*, and c-*Myc*; therefore, we evaluated the expression levels of these genes in ALL cell lines. The relative expression of *c-myc* was significantly elevated in the T-ALL cell lines compared with the T-lymphocytes (about 4-folds, P<0.01 (Jurkat), P<0.001 (RPMI-8402), and in the B-ALL cell lines compared with the B-lymphocytes (about 7-folds, P<0.001, Fig.4A). After treatment with VCR or ASP, *c-Myc* expression was significantly decreased in all cell lines; it was almost the same in Jurkat and Ramos cells after treatment. However, RPMI-8402 and Daudi cells had more robust decreases in *c-Myc* expression after treatment with ASP compared to VCR (Fig.4B, C). In contrast to the *c-Myc* expression pattern, there was a significant downregulation of *P53* expression in all of the cell lines, with the exception of Ramos cells (Fig.4D). On the other hand, *P53* expression was upregulated remarkably in all cell lines treated with either ASP or VCR. *P53* expression was significantly higher in the VCR-treated groups compared to the ASP-treated Jurkat cells (9-folds, P<0.001 vs. 4-folds, P<0.01) and RPMI-8402 cells (10-folds vs. 6-folds, P<0.001), respectively. B cell lines had approximately the same expression pattern of *P53* in the treated groups. Its expression was about 11.8 folds, P<0.001 in Daudi cells and about 5.7 folds P<0.01 in Ramous cells after treatment with VCR and ASP (Fig.4E, F). This finding showed that chemotherapy treatments upregulated *P53* expression, but downregulated *c-Myc*, which may ultimately lead to downregulation of *H19* expression. In addition, *H19* expression in hypoxic condition was related to *HIF-1a* gene through blocking *P53* expression; therefore, we evaluated the expression level of *HIF-1a* and *P53* in ALL cell lines. Expression of *HIF-1a* was upregulated in the B and T ALL cell lines (about 6-folds) (Fig.5A, B), whereas upregulation of *P53* was observed in all cell lines (Fig.5C, D). This result showed that upregulation of *H19* could be related to these genes in hypoxic condition.

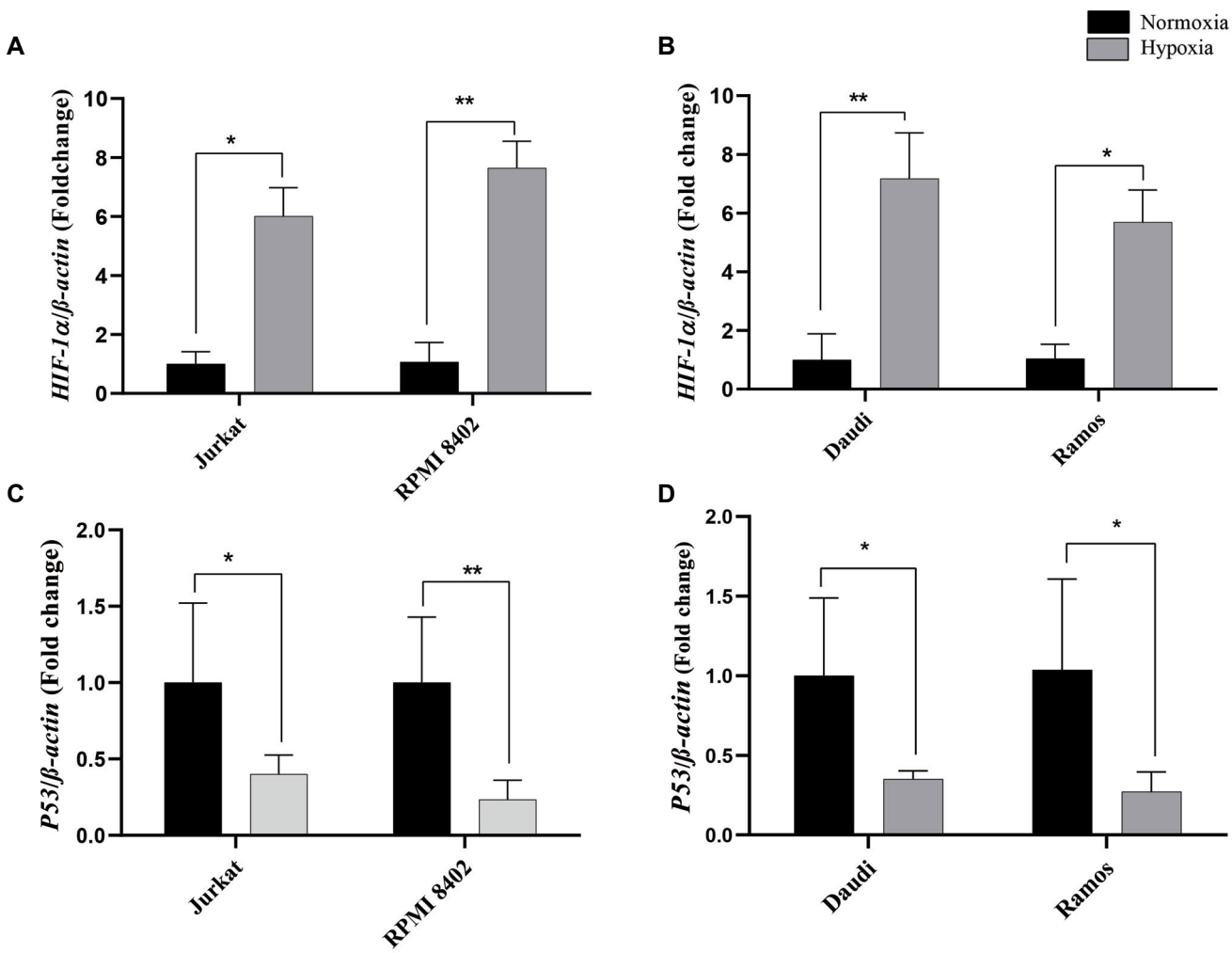

Fig.5: Expression of *c-Myc* and *P53* genes in the ALL cell lines after hypoxic condition. **A, B.** Expression of *HIF-1a* was evaluated by qRT-PCR after the cell lines were put into hypoxic condition for 24 hours. **C, D.** Expression of *P53* was evaluated after exposure to the hypoxic condition in comparison to normoxic culture conditions. The data are cultures from three independent experiments, each done in triplicate. ALL; Acute lymphoblastic leukemia, qRT-PCR; Quantitative real time polymerase chain reaction, *; P<0.05, and **; P<0.00.

Discussion

Gene expression is involved in various physiological processes, including differentiation, apoptosis, cell proliferation, and metastasis, and is directly regulated by LncRNA. It has been suggested that these LncRNAs could acts as tumor suppressors or oncogenes that make them potential diagnostic and prognostic biomarker in cancers (12). The expression level of H19 and its presumptive role in ALL have not been entirely appreciated. In the present study, we found that the level of *H19* expression increases in ALL patients that might have a tumor promoter in ALL, which is in harmony with other studies. In previous studies, Zhang et al. (22) have reported that upregulation of *H19* expression in BM-MNCs from newly diagnosed AML patients; these changes were reported in eight cell lines derived from AML patients. In another study on hematologic malignancies, Guo et al. (20) observed higher expression of *H19* in cell lines with Bcr-Abl transformation and in primary cells from patients with chronic myelogenous leukemia (CML). Downregulation of the *H19* expression has been shown to sensitize leukemic cells to imatinib-induced apoptosis and inhibit tumor growth resulting from Bcr-Abl transformation. In addition to hematologic malignancies, other investigations also reported overexpression of *H19* in numerous solid cancers such as hepatic, bladder, gastric, lung, and ovarian cancers (5).

In our study, we evaluated *H19* expression in ALL patients. Interestingly, an analogous increase in *H19* expression occurred in both T-ALL and B-ALL patients as well as in the cell lines; however, *H19* expression was significantly higher in the cell lines.

Previous studies verified the gene-gene interactions between *H19* and crucial genes related to survival and proliferation, such as *c-Myc* and *P53*. Thus, we further assessed *c-Myc* expression in ALL. *H19* and *c-Myc* expression levels were significantly increased in ALL patients and cell lines. We assumed that there could be a correlation between elevated expressions of these two genes. The Ramos and Jurkat cell lines had significantly higher *c-Myc* expression and significantly greater *H19* expression. The results of other studies showed that c-Myc could upregulate *H19* expression, Guo et al. (20) observed this direct induction in K562 cell lines. They found that knockdown of c-*myc* expression significantly decreased *H19* expression. The same relationship has been also reported in breast, esophageal, and colorectal tumors (21, 22).

In contrast to *c-Myc*, which has been demonstrated to increase H19 expression and enhance cell growth and tumorigenesis, P53 is the most important tumor suppressor gene in cancer that is negatively associated with H19 expression. p53 not only represses the promoter activity of the H19 gene, it also suppresses H19 expression at the epigenetic level (9). Dugimont et al. (28) reported the inhibitory effect of P53 on H19 expression by the luciferase assay in HeLa (cervical cancer) and Calu-6 (human pulmonary adenocarcinoma) cell lines. This was also confirmed in the AGS cell line (gastric cancer), where ectopic H19 expression increased cell proliferation, and H19 siRNA treatment was associated with P53 inactivation and cell apoptosis (37). Our findings demonstrated an inverse relationship between P53 and H19 expressions. We observed decreased *P53* expression in the ALL patients along with elevated *H19* expression. The same correlation occurred in the cell lines where higher expression of *H19* co-occurred with decreased *P53* expression.

Apart from gene-gene interactions, environmental stimuli could effectively change the cellular process, and particularly affect cell growth and apoptosis, as well. Notably, previous studies have indicated that hypoxic stress induces H19 expression and could increase cell proliferation in malignancies. It has been confirmed that hypoxia regulates leukemia progression and causes resistance to radiotherapy and chemotherapy (33, 38). HIF-1α is a key regulator of the hypoxic response and a major oxygen homeostasis regulator. It is a crucial factor that is responsible for H19 RNA induction under hypoxic conditions by inhibiting P53 expression (39).

Matouk and colleagues demonstrated that hypoxia upregulates H19 expression via an inhibitory effect of HIF-1a on P53 expression in hepatocellular and bladder carcinoma (25). In another study, they manipulated different lineage sources of carcinoma and overexpressed H19. This modification was along with a decreased level of P53 expression. They demonstrated a tight connection between the P53 gene and H19 expression under hypoxic stress, which was determined by semi-quantitative RT-PCR. These researchers also found that knockdown of HIF-1α remarkably diminished *h19* expression under hypoxic condition (35).

H19 expression was significantly increased in ALL patient samples, which could be due to hypoxia-like conditions in BM. The ALL cell lines confirmed that the hypoxic condition and *HIF-1α* induction caused *P53* suppression and a simultaneous up-regulation of *H19*.

We examined the expression of *H19* and its related genes in B and T ALL patients and cell lines. Next, we examined the potential application of *H19* in therapeutic conditions by treating the ALL cell lines with two common chemotherapy drugs prescribed for ALL patients, VCR and ASP. Next, we evaluated the expressions of *H19* and its associated genes following drug treatments. Expression of *H19* in the treated leukemia cell lines was downregulated compared to the untreated cell lines. In addition, assessment of the related genes demonstrated that suppression of *H19* occurred along with significantly elevated *P53* and lower *c-Myc* expressions. This pattern could suggest the possible prognostic applications of *H19* in patients with ALL. Several studies also explored the role of H19 in the clinical status of cancer patients. Zhang et al. (22) reported that H19 overexpression correlated with poor overall survival and chemotherapy

response among AML patients. However, H19 expression in patients with AML who achieved complete remission after induction therapy was lower compared to the patients with relapses. In another study, Guo et al. (20) found that tumor formation was attenuated by h19 knockdown in a mouse xenograft model. They observed that *H19* repression in K562 cell line could significantly inhibit tumor progression. Knocking down *H19* RNA by siRNA resulted in inhibiting tumorigenicity in hepatocellular cells (Hep3B) and human bladder carcinoma cells (UMUC3*) in vivo* (25).

Conclusion

It has been demonstrated that H19 expression might act as a novel target for prognosis prediction as well as the means for assessing the clinicopathologic features in various cancers. Our findings show that the expression of *H19* increased in B and T ALL patients and cell lines, which may be related to the expression of *P53*, *c-Myc*, and *HIF-1α*. Interestingly*, H19* expression was significantly upregulated by hypoxic condition, while a decreased expression of this gene was observed after treatment with chemotherapy drugs. Although our study suggests that *H19* could be accounted for a potential therapeutic target or useful predictive biomarker in ALL patients, further investigation is needed to identify the molecular mechanisms underlying *H19* function in pathological process and/or carcinogenesis in this disease.

Acknowledgments

This work was supported by Tehran University of Medical Science and Health Services under the Grant [number 31542]. The authors declare no conflicts of interest in this study.

Authors' Contributions

M.A., M.A.Gh.; Performed all *in vitro* experiments, analyzed the data and wrote the manuscript. Sh.A.; Contributed to the study concept and design. F.K.; Contributed to sample preparation and data gathering from patients. All authors read and approved the final manuscript.

References

1. Miller KD, Siegel RL, Lin CC, Mariotto AB, Kramer JL, Rowland JH, et al. Cancer treatment and survivorship statistics, 2016. CA Cancer J Clin. 2016; 66(4): 271-289.
2. Hulleman E, Kazemier KM, Holleman A, VanderWeele DJ, Rudin CM, Broekhuis MJ, et al. Inhibition of glycolysis modulates prednisolone resistance in acute lymphoblastic leukemia cells. Blood. 2009; 113(9): 2014-2021.
3. Kang MH, Kang YH, Szymanska B, Wilczynska-Kalak U, Sheard MA, Harned TM, et al. Activity of vincristine, L-ASP, and dexamethasone against acute lymphoblastic leukemia is enhanced by the BH3-mimetic ABT-737 in vitro and in vivo. Blood. 2007; 110(6): 2057-2066.
4. Angrand PO, Vennin C, Le Bourhis X, Adriaenssens E. The role of long non-coding RNAs in genome formatting and expression. Front Genet. 2015; 6: 165.
5. Bhan A, Soleimani M,Mandal SS. Long noncoding RNA and cancer: a new paradigm. Cancer Res. 2017; 77(15): 3965-3981.
6. Ernst C, Morton CC. Identification and function of long non-coding RNA. Front Cell Neurosci. 2013; 7: 168.
7. Kopp F, Mendell JT. Functional classification and experimental dissection of long noncoding RNAs. Cell. 2018; 172(3): 393-407.
8. Raveh E, Matouk IJ, Gilon M, Hochberg A. The H19 Long noncoding RNA in cancer initiation, progression and metastasis–a proposed unifying theory. Mol Cancer. 2015; 14(1): 184.
9. Yoshimura H, Matsuda Y, Yamamoto M, Kamiya S, Ishiwata T. Expression and role of long non-coding RNA H19 in carcinogenesis. Front Biosci (Landmark Ed). 2018; 23: 614-625.
10. Zhang EB, Han L, Yin DD, Kong R, De W, Chen J. c-Myc-induced, long, noncoding H19 affects cell proliferation and predicts a poor prognosis in patients with gastric cancer. Med Oncol. 2014; 31(5): 914.
11. Yoshimura H, Matsuda Y, Suzuki T, Naito Z,Ishiwata T. Long noncoding RNA H19 as a novel therapeutic target for pancreatic cancer. Cancer Res. 2014; 74 Suppl 19: 5203.
12. Chi Y, Wang D, Wang J, Yu W, Yang J. Long non-coding RNA in the pathogenesis of cancers. Cells. 2019; 8(9): 1015.
13. Li Y, Ma HY, Hu XW, Qu YY, Wen X, Zhang Y, et al. LncRNA H19 promotes triple-negative breast cancer cells invasion and metastasis through the p53/TNFAIP8 pathway. Cancer Cell Int. 2020; 20: 200.
14. Anastasiadou E, Jacob LS, Slack FJ. Non-coding RNA networks in cancer. Nat Rev Cancer. 2018; 18(1): 5-18.
15. Yoshimizu T, Miroglio A, Ripoche MA, Gabory A, Vernucci M, Riccio A, et al. The H19 locus acts in vivo as a tumor suppressor. Proc Natl Acad Sci USA. 2008; 105(34): 12417-12422.
16. Cerk S, Schwarzenbacher D, Adiprasito JB, Stotz M, Hutterer GC, Gerger A, et al. Current status of long non-coding RNAs in human breast cancer. Int J Mol Sci. 2016; 17(9): 1485.
17. Lottin S, Adriaenssens E, Dupressoir T, Berteaux N, Montpellier C, Coll J, et al. Overexpression of an ectopic H19 gene enhances the tumorigenic properties of breast cancer cells. Carcinogenesis. 2002; 23(11): 1885-1895.
18. Qi P, Du X. The long non-coding RNAs, a new cancer diagnostic and therapeutic gold mine. Mod Pathol. 2013; 26(2): 155-165.
19. Tanos V, Ariel I, Prus D, De-Groot N, Hochberg A. H19 and IGF2 gene expression in human normal, hyperplastic, and malignant endometrium. Int J Gynecol Cancer. 2004; 14(3): 521-525.
20. Guo G, Kang Q, Chen Q, Chen Z, Wang J, Tan L, et al. High expression of long non-coding RNA H19 is required for efficient tumorigenesis induced by Bcr-Abl oncogene. FEBS lett. 2014; 588(9): 1780-1786.
21. Morlando M, Ballarino M, Fatica A. Long non-coding RNAs: new players in hematopoiesis and leukemia. Front Med (Lausanne). 2015; 2: 23.
22. Zhang Tj, Zhou Jd, Zhang W, Lin J, Ma Jc, Wen Xm, et al. H19 overexpression promotes leukemogenesis and predicts unfavorable prognosis in acute myeloid leukemia. Clin Epigenetics. 2018; 10(1): 47.
23. Lim YW, Xiang X, Garg M, Le MT, Wong A L-A, Wang L, et al. The double-edged sword of H19 lncRNA: Insights into cancer therapy. Cancer Lett. 2021; 500: 253-262.
24. Arun G, Diermeier SD,Spector DL. Therapeutic targeting of long non-coding RNAs in cancer. Trends Mol Med. 2018; 24(3): 257-277.
25. Matouk IJ, DeGroot N, Mezan S, Ayesh S, Abu-lail R, Hochberg A, et al. The H19 non-coding RNA is essential for human tumor growth. PLoS One. 2007; 2(9): e845.
26. Huang J, Zhang A, Ho TT, Zhang Z, Zhou N, Ding X, et al. LincRoR promotes c-Myc expression through hnRNP I and AUF1. Nucleic Acids Res. 2016; 44(7): 3059-3069.
27. Li Y, Sasaki H. Genomic imprinting in mammals: its life cycle, molecular mechanisms and reprogramming. Cell Res. 2011; 21(3): 466-473.
28. Dugimont T, Montpellier C, Adriaenssens E, Lottin S, Dumont L, Iotsova V, et al. The H19 TATA-less promoter is efficiently repressed by wild-type tumor suppressor gene product p53. Oncogene. 1998; 16(18): 2395-2401.
29. Liu C, Chen Z, Fang J, Xu A, Zhang W, Wang Z. H19-derived miR-675 contributes to bladder cancer cell proliferation by regulating p53 activation. Tumour Biol. 2016; 37(1): 263-270.
30. Park IY, Sohn BH, Choo JH, Joe CO, Seong JK, Lee YI, et al. Deregulation of DNA methyltransferases and loss of parental methylation at the insulin-like growth factor II (Igf2)/H19 loci in p53 knockout mice prior to tumor development. J Cell Biochem. 2005; 94(3): 585-596.
31. Petit C, Gouel F, Dubus I, Heuclin C, Roget K,Vannier J. Hypoxia promotes chemoresistance in acute lymphoblastic leukemia cell

lines by modulating death signaling pathways. BMC Cancer. 2016; 16(1): 746.
32. Wilson WR, Hay MP. Targeting hypoxia in cancer therapy. Nat Rev Cancer. 2011; 11(6): 393-410.
33. Frolova O, Samudio I, Benito JM, Jacamo R, Kornblau SM, Markovic A, et al. Regulation of HIF-1α signaling and chemoresistance in acute lymphocytic leukemia under hypoxic conditions of the bone marrow microenvironment. Cancer Biol Ther. 2012; 13(10): 858-870.
34. Luo M, Li Z, Wang W, Zeng Y, Liu Z, Qiu J. Upregulated H19 contributes to bladder cancer cell proliferation by regulating ID2 expression. FEBS J. 2013; 280(7): 1709-1716.
35. Matouk IJ, Mezan S, Mizrahi A, Ohana P, Abu-lail R, Fellig Y, et al. The oncofetal H19 RNA connection: hypoxia, p53 and cancer. Biochim Biophys Acta. 2010; 1803(4): 443-451.
36. Fahy L, Calvo J, Chabi S, Renou L, Le Maout C, Poglio S, et al. Hypoxia favors chemoresistance in T-ALL through an HIF1α-mediated mTORC1 inhibition loop. Blood Adv. 2021; 5(2): 513-526.
37. Yang F, Bi J, Xue X, Zheng L, Zhi K, Hua J, et al. Up-regulated long non-coding RNA H19 contributes to proliferation of gastric cancer cells. FEBS J. 2012; 279(17): 3159-3165.
38. Houghton PJ, Lock R, Carol H, Morton CL, Phelps D, Gorlick R, et al. Initial testing of the hypoxia-activated prodrug PR-104 by the pediatric preclinical testing program. Pediatr Blood Cancer. 2011; 57(3): 443-453.
39. Deynoux M, Sunter N, Hérault O, Mazurier F. Hypoxia and hypoxia-inducible factors in leukemias. Front Oncol. 2016; 6: 41.

Cell J
Cell Journal(Yakhteh) Homepage: https://www.celljournal.org/
Original Article Vol 25, No 1, January 2023, Pages: 11-16

Beneficial Mitochondrial Biogenesis in Gastrocnemius Muscle Promoted by High-Intensity Interval Training in Elderly Female Rats

Hossein Pirani, Ph.D.[1*], Ali Bakhtiari, Ph.D.[2], Bahareh Amiri, Ph.D.[3], Omid Reza Salehi, Ph.D.[3]

1. Department of Basic Sciences, Chabahar Maritime University, Chabahar, Iran
2. Department of Physical Education and Sport Sciences of Tehran University, Tehran, Iran
3. Department of Physical Education and Sport Sciences, University of Kurdistan, Sanandaj, Iran

**Corresponding Address: P.O.Box: 997175649, Department of Basic Sciences, Chabahar Maritime University, Chabahar, Iran*
Email: hn.piranis@gmail.com

Received: 11/July/2022, Revised: 20/July/2022, Accepted:28/August/2022

Abstract

Objective: Exercise can attenuate mitochondrial dysfunction caused by aging. Our study aimed to compare 12 weeks of high-intensity interval training (HIIT) and moderate-intensity continuous training (MICT) on the expression of mitochondria proteins [e.g., AMP-activated protein kinase (AMPK), Estrogen-related receptor alpha (ERRα), p38 mitogen-activated protein kinase (P38MAPK), and Peroxisome proliferator-activated receptor gamma coactivator 1-alpha (PGC1-α)] in gastrocnemius muscle of old female rats.

Materials and Methods: In this experimental study, thirty six old female Wistar rats (18-month-old and 270-310 g) were divided into three groups: i. HIIT, ii. MICT, and iii. Control group (C). The HIIT protocol was performed for 12 weeks with 16-28 minutes (2 minutes training with 85-90% VO_{2max} in high intensity and 2 minutes training with 45-75% VO_{2max} low intensity). The MICT was performed for 30-60 minutes with the intensity of 65-70% VO_{2max}. The gastrocnemius muscle expression of AMPK, ERRα, P38MAPK, and PGC1α proteins were determined by Western blotting.

Results: The expression of AMPK (P=0.004), P38MAPK (P=0.003), PGC-1α (P=0.028), and ERRα (P=0.006) in HIIT was higher than C group. AMPK (P=0.03), P38MAPK (P=0.032), PGC-1α (P=0.015), and ERRα (P=0.028) in MICT was higher than the C group. Also expression of AMPK (P=0.008), P38MAPK (P=0.009), PGC-1α (P=0.020) and ERRα (P=0.014) in MICT was higher than MICT group.

Conclusion: It seems that exercise training has beneficial effects on mitochondrial biogenesis, but the HIIT training method is more effective than MICT in improving mitochondrial function in aging.

Keywords: Aging, Exercise, Mitochondrial, Muscle

Citation: **Pirani H, Bakhtiari A, Amiri B, Salehi OR. Beneficial mitochondrial biogenesis in gastrocnemius muscle promoted by high-intensity interval training in elderly female rats. Cell J. 2023; 25(1): 11-16. doi: 10.22074/CELLJ.2022.557565.1078.**

Introduction

Aging is a natural, progressive and damaging process that is associated with various damages and reduction of functional efficiency in cells and tissues homeostasis over time (1, 2). Any discovery in cellular and molecular biology introduces a new family of aging theories, all of which will increase our perception of the aging process (3). Studies have shown that sarcopenia, or muscle atrophy, is associated with impaired muscle cell metabolism and disorder in ATP/ADP ratio, activated kinase protein of AMP (AMPK); This process is mediated by increased tumor necrosis factor alpha (TNF-α), oxidative stress and anabolic signaling pathways, such as Peroxisome proliferator-activated receptor gamma coactivator 1-alpha (PGC1-α), p38 mitogen-activated protein kinases (P38MAPK)/Extracellular signal-regulated kinase (ERK)1/2 and c-Jun N-terminal kinases (JNKs) (4, 5). Almost all aging theories enumerate mitochondria dysfunction as one of the most critical factors in the aging process. This mitochondrial dysfunction is a multifactorial process in which DNA damage and enzymatic disorder are the most important processes (6). AMPK and P38MAPK are vital in Mitochondrial biogenesis. One of its downstream proteins, PGC1-α, is a multitask protein serving as a switch molecule, and this protein can increases the biogenesis of mitochondria by activating transcription factors such as nuclear respiratory factors 1 and 2 (NRF-1/2) and estrogen-related receptor alpha (ERRα) (7). Activation of these replicating factors increases the expression of mitochondrial transcription factor A (Tfam) and Mitochondrial transcription factor B1 and B2 (TFB1/2M). NRF1-2 is necessary to duplicate, replicate and maintain mtDNA (8, 9). Aging decrease the content of mitochondrial proteins (10). The researchers stated that the disorder of mitochondrial function in aging rats with telomere disorder had been correlated with rates of AMPK and PGC-1α suppression (6).

But regular exercise/training is a critical therapeutic intervention for aging, and it can improve brain function and metabolic disorders, attenuate sarcopenia, and increase mitochondrial oxidative capacity (11). According to studies, exercise training can lead to insulin-like growth factor-1 (IGF-1)/Ak/mTOR signaling activation mechanisms, as well as FoxOs/Nuclear transcription factor kappa-B (NF-κB) and MAPKs. Also, exercise

training increases NRF1/2, improves protein synthesis, and increases mitochondrial biogenesis in skeletal muscle (5, 12). The net effect of exercise depends on its variables; among them, intensity is the most important. Intense exercise training can lead to a higher reduction in ADP & AMP levels, making a better stimulation for AMPK activation.

Moreover, reports indicate that the type, intensity, and duration of exercise affect the expression of mitochondrial biogenesis proteins (8). Short-term, high-intensity endurance exercise and long-term aerobic swimming training increased SIRT1 and PGC-1α proteins in muscles (9). Another study showed the HIIT, and MICT drastically increased protein contents of PGC-1α and mtDNA expression. Soleus muscle was decreased in both inactive elderly rats versus inactive juveniles (10). Soleus muscle protein PGC-1α increased 2.3-fold in active elderly mice compared to inactive elderly mice (11, 13, 14). It has also been reported that the expression of mitochondrial biogenesis proteins, especially MAPK, NRF1-2, Tfam, SIRT1, and PGC1α, increased significantly in young people following high-intensity interval training (HIIT) compared to moderate intensity continuous training (MICT) (9). Although studies have examined the effect and intensity of endurance training on mitochondrial biogenesis in skeletal muscle, it seems that the difference in the type and intensity of exercise and its effect on mitochondrial function markers in sarcopenia is not well understood; in addition, due to the differences during the training period and adaptation to training, conducting studies with long-term training is very important in obtaining more information compared to the two types of exercise. So this study aimed to determine the effects of 12 weeks of HIIT and MICT on the expression of mitochondria proteins in old female rats.

Materials and Methods

This experimental study was performed in compliance with all ethical principles of working with laboratory animals and was approved by the Ethics Committee of the Faculty of Physical Education, University of Tehran (IR.UT.SPORT.REC.1397.021). In this study, 36 female elderly Wistar rats (18-month-old) (1, 15) were bought from the Pasteur Institute of Iran and randomly divided into three groups: HIIT, MICT, and control (C) groups. Rodent housed in a standard lab (12-hour light-dark cycle with an average temperature of 22-23°C and a humidity of 45%) with free access to water and food in the Faculty of Physical Education, University of Tehran. In addition, the rats in this study were kept in washable polycarbonate cages; a sterile wood grater was used to absorb moisture from the cages. All protocols conformed with the Guide Laboratory Animals for The Care and Use.

Maximum oxygen consumption determination

Rats were introduced to living conditions in the laboratory and trained on how to run on a treadmill for five days. The rat's maximum oxygen consumption (VO_{2max}) was assessed using an incremental test described by Høydal et al. (16). In summary, rats warmed up for 10 minutes at a speed of 10 meters per minute. Subsequently, they entered the test stage. Every two minutes, the treadmill's speed increased by 0.03 m/s until the rats could not continue the test (unable to run on the treadmill and go to the end space of the treadmill). After the exercise test was completed, the velocity at which the rat ran (last velocity in the exhaustion phase) was recorded. The VO_{2max} was measured using the equation y=162x-1 where y represents oxygen consumption in milliliters per minute per kilogram of body weight and x, indicates the maximum speed of running per meters per second).

Exercise protocol

Both HIIT and MICT protocols consisted of three parts: warm-up, main body, and cool down, as described in Tables 1 and 2. The following formulas were used to equalize the training load. Total training time in HIIT group: (minutes*intensity of work interval)+(minutes*intensity of rest interval). Total training time in MICT group: minutes*intensity).

Table 1: High-intensity interval training (HIIT) protocol

Week	Warm up	Work interval	Rest interval	Cool down	Total training time
1st and 2nd	3 minutes with running 45-50% VO_{2max}	4* (two-minute running with 85-90% VO_{2max}	4 two-minutes repetitions 45-50% VO_{2max}	3 minutes with running 45-50% VO_{2max}	14 minutes
3rd, 4th, and 5th	3 minutes- 45-50% $VO_{2\,max}$	5 two-minute repeated training 85-90% $VO_{2\,max}$	5 two-minutes repetitions 45-50% $VO_{2\,max}$	3 minutes with 45-50% intensity $VO_{2\,max}$	16 minutes
6th, 7th, and 8th	3 minutes- 45-50% VO_{2max}	7 two-minute repeated training 85-90% $VO_{2\,max}$	7 two-minutes repetitions 45-50% $VO_{2\,max}$	3 minutes with 45-50% intensity $VO_{2\,max}$	20 minutes
9th, 10th, 11th, and 12th	3 minutes- 45-50% VO_{2max}	7 two-minute repeated training 85-90% $VO_{2\,max}$	7 two-minutes repetitions 45-50% $VO_{2\,max}$	3 minutes with 45-50% intensity $VO_{2\,max}$	20 minutes

Table 2: MICT protocol

Training weeks	Warm up	Training body	Cool down	Total training time
Two first weeks	3 minutes, 45-50%VO_{2max}	65-70% VO_{2max} for 30 minutes	3 minutes, 45-50% VO_{2max}	36 minutes
3rd, 4th and 5th weeks	3 minutes, 45-50%VO_{2max}	65-70% VO_{2max} for 45 minutes	3 minutes, 45-50% VO_{2max}	51 minutes
6th, 7th, 8th weeks	3 minutes, 45-50%VO_{2max}	65-70% VO_{2max} for 50 minutes	3 minutes, 45-50% VO_{2max}	56 minutes
9th, 10th, 11th and 12th weeks	3 minutes, 45-50%VO_{2max}	65-70% VO_{2max} for 60 minutes	3 minutes, 45-50% VO_{2max}	66 minutes

Measurement procedures

Two days after the last training session, rats were anesthetized using ketamine and xylazine. Their left gastrocnemius muscle was extracted and immediately frozen in liquid nitrogen and kept at -80˚C until further analysis. Western blot was used to study AMPK, ERRα, P38MAPK, and PGC1α proteins levels. First, 100 mg of gastrocnemius muscle tissue was homogenized with 200 µl of Rippa lysis buffer, and then, the sample was centrifuged for 20 minutes at 1300 rpm at 4˚C. The supernatant was transferred to a 1 cc microtype, and 0.5 l was poured into another microtype to determine the protein concentration using nanodrop. The protein concentration in all samples was diluted with a certain ratio. Stacking gel and separating gel required for agarose gels were prepared using the materials needed. Subsequently, wells were created to pour the sample. Samples were poured into wells and placed in X1 electrophoresis buffer. After this step, the protein was transferred from the gel to PVDF paper. The primary antibodies AMPK (Ab191838, Cambridge Science Park, Cambridge, UK) and ERRα (Ab131607, Cambridge Science Park, Cambridge, UK) were diluted 1 to 1000 and used. After 24 hours of PVFD paper quenching, a diluted secondary antibody of 1 to 1000 was used. GAPDH was also used as a control protein, and finally, colored substrate (ECL) was added to PVDF paper in the dark room. After a few seconds, the emergence films were placed on paper. The emergence films were immediately transferred to the fixation and emergence solutions. After the desired protein bands appeared on the film strips, the films were photographed, and the size of each band was calculated using Image J software.

Statistical analysis

Shapiro-Wilk test was used to assess the data normality, and one-way analysis of variance (ANOVA) and Tukey post hoc tests were used to compare the data between groups. Data analysis was performed using SPSS software version 16 packaged by National Opinion Research Center (NORC), at the University of Chicago, and Microsoft Office software such as Excel and PowerPoint was used to design the graphs. The significance level was considered less than 0.05.

Results

The results of ANOVA showed that there was a significant difference between groups in AMPK (P=0.001), ERRα (P=0.001), P38MAPK (P=0.0013), and PGC1α (P=0.002).

Tukey's post hoc test showed that AMPK in both HIIT (P=0.004) and MICT (P=0.03) groups was higher than the C group and in HIIT was higher than the MICT group (P=0.008, Fig.1).

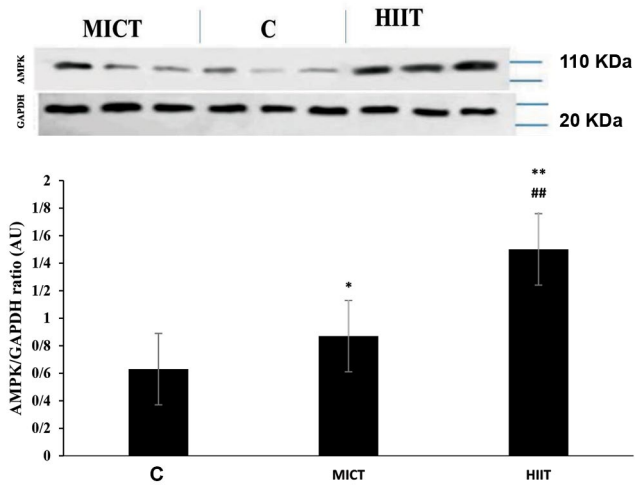

Fig.1: The ANOVA test results for expression rates of AMPK/GAPDH in research groups. *; P≤0.05, **; P≤0.01 increased AMPK in MICT and HIIT groups compared to the C group, and ##; P≤0.01 increased AMPK in the HIIT group compared to the MICT group. MICT; Moderate-intensity continuous training and HIIT; High-intensity interval training.

Also, the levels of P38MAPK protein in the MICT (P=0.032) and HIIT (P=0.003) groups significantly increased compared to the C group. Also, the levels of P38MAPK protein in the HIIT group showed a significant

increase compared to the MICT group (P=0.009, Fig.2).

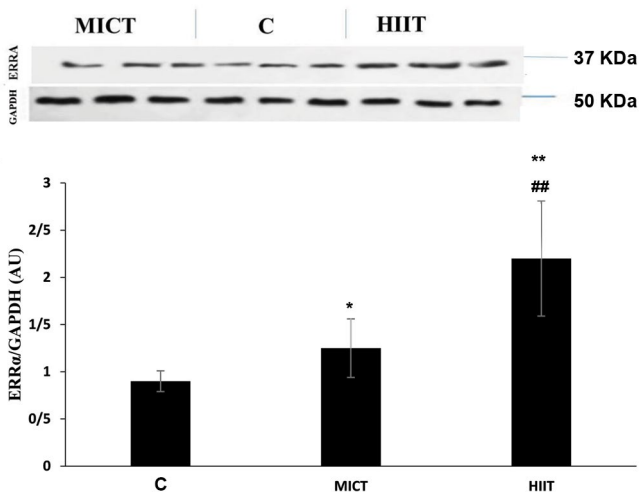

Fig.2: The ANOVA test results for expression rates of ERRa/GAPDH in research groups. *; P≤0.05, **; P≤0.01 increased ERRa in MICT and HIIT groups compared to the C group, and ##; P≤0.01 increased ERRa in the HIIT group compared to the MICT group. MICT; Moderate-intensity continuous training and HIIT; High-intensity interval training.

The level of PGC-1α protein in the MICT (P=0.015) and HIIT (P=0.028) groups significantly increased compared to the C group. The level of PGC-1α protein in the HIIT was higher than the MICT group (P=0.020, Fig.3).

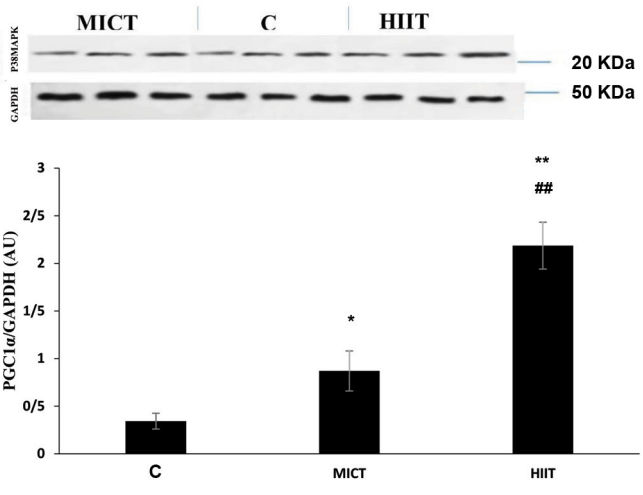

Fig.3: The ANOVA test results for expression rates of PGC1-a/GAPDH in research groups. *; P≤0.05, **; P≤0.01 increased PGC1-a in MICT and HIIT groups in comparison to the C group, and ##; P≤0.01 increased PGC1-a in the HIIT group compared to the MICT group.

Also, ERRα protein in the MICT (P=0.028) and HIIT (P=0.006) groups was higher than in the C group. ERRα protein levels in the HIIT group increased significantly compared with the MICT (P=0.014) group (Fig.4).

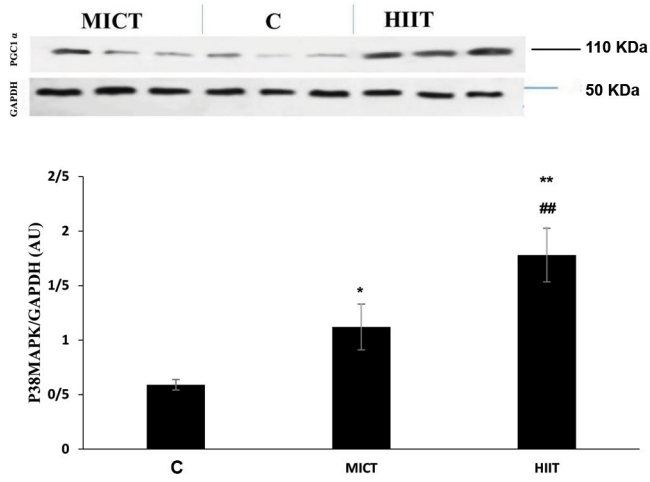

Fig.4: ANOVA test results for expression rates of P38MAPK/GAPDH in research groups. *; P≤0.05, **; P≤0.01 increased P38MAPK in MICT and HIIT groups compared to the C group, and ##; P≤0.01 increased P38MAPK in the HIIT group compared to the MICT group. MICT; Moderate-intensity continuous training and HIIT; High-intensity interval training.

Discussion

In this study, the effect of HIIT and MICT on total protein levels of AMPK, ERRα, P38MAPK, and PGC1α in the gastrocnemius muscle of aging rats was compared. This study showed that both HIIT and MICT models increased the amounts of proteins involved in mitochondrial biogenesis. The population of elderly women in the last century has increased due to increased life expectancy. With the onset of menopause in these women, estrogen secretion is disrupted; this factor is one of the leading causes of problems in elderly women, such as osteoporosis, sarcopenia, muscle atrophy, and decreased physical function (4). Physical activity increases oxidative capacity and muscle function. This adaptation is partly due to the exercise-induced increase in proteins involved in the transport and oxidation of metabolic substrates and the increase in mitochondrial content. Therefore, exercise may improve cellular metabolism. The mechanism of mitochondrial biogenesis seems to be multifactorial. Still, exercise intensity is one of the most critical factors in activating proteins in this pathway. The important finding of this study was that HIIT increased the amounts of AMPK, ERRα, P38MAPK, and PGC1α in the gastrocnemius muscle of aging rats more than MICT. These results highlight the importance of intensity in exercise-induced mitochondrial biogenesis. In line with our results, it has been shown that high-intensity exercise causes more cellular stress than low-intensity exercise, providing better stimulation for mitochondrial biogenesis (17). Granata et al. (18) showed that sprint interval training (SIT) had a more significant effect on mitochondrial function than HIIT.

Improving the lactate threshold could lead to better mitochondrial function, and because SIT is more effective in enhancing the lactate threshold, it causes more improvements in mitochondrial function. In other words, increasing exercise intensity enhances ADP and AMP production, which in turn increases ADP, AMP/ATP ratio and activates AMPK, an upstream of ERRα and PGC-1a (10). In addition to AMPK, it is also possible that activation of beta (2) -adrenergic receptor by catecholamines stimulates PGC-1α expression through an increase in cAMP levels and thus activation of CREB (AMP-responsive element-binding) transcription factors (19, 20). It seems that the same happens in aging rates because three weeks of endurance training with 85-90% of VO_{2max} increased the expression of PGC-1α, Tfam, and AMPK in the Soleus muscle (21, 22). HIIT training compared to MICT leads to a more significant increase in aerobic capacity (21). Increased cardiorespiratory capacity seems to be associated with increased stroke volume and cardiac output (23).

Furthermore, increased stroke volume and cardiac output are likely associated with the more significant cardiac challenge due to HIIT exercise program rotations. Increasing VO_{2max} leads to a further increase of oxidative capacity and, ultimately, more mitochondrial content. Therefore, one of the reasons for the further increase in PGC-1α protein synthesis is the increase in VO_{2max} induced by HIIT (23, 24). The intensity of exercise is one of the influential factors in improving the condition of mitochondrial biogenesis in the elderly. Intense training, including HIIT, increases the AMP/ADP/ATP ratio, followed by a further increase in AMPK. This factor can further increase ERRα and PGC-1a (as an upstream factor) (18, 25). Green et al. (26) examined the metabolic stress during exercise in a steady state following ten days of 30 or 60 minutes of cycling at a low, medium, and high intensity (60-86% VO_{2max}). Their study showed that following higher-intensity exercise, the cumulative levels of AMP and ADP and depletion of phosphocreatine occur in the muscle. Recently, a study has shown that increasing the volume of HIIT exercise (with increasing frequency and duration) increases the muscles' mitochondrial content (10).

Therefore, exercise frequency is also one of the effective factors in increasing mitochondrial biogenesis (18). Other factors appear to be involved in increasing AMPK expression. Furthermore, indicators such as SIRT1 and p53 as upstream factors can affect AMPK activity and expression. PGC-1α can also directly induce DNA to transcribe P53 (27). It seems that Short-term muscle activity can lead to P53 activation by increasing AMPK and P38MAPK levels.

Nevertheless, the intensity of exercise has been shown to be an essential factor in increasing p53 expression in order to increase PGC-1α expression. In such a way that only periodic rapid exercise increased p53 (25). So it seems that the intensity of exercise training is an important factor in increasing p53 expression, which has not been measured in this study to justify higher expression levels of PGC-1α compared to CT.

Conclusion

HIIT appears to improve mitochondrial function by increasing PGC-1α and ERRα levels. Probably one of the reasons for the increase in mitochondrial proteins in the gastrocnemius muscles is the training nature of HIIT (short and severe episodes). Considering the favorable effects of HIIT training on mitochondrial biogenesis compared to continuous training, it is suggested to use HIIT training to improve muscle performance in the elderly. However, considering the effect of IGF-1/Akt in inhibiting muscle atrophy and their impact on MAPK activation, it seems that the lack of evaluation of IGF-1/Akt/mTOR pathway is one of the limitations of this study. Therefore, studying hypertrophy signaling pathways under the influence of type and intensity of exercise in sarcopenia should be considered in future studies. Also, ATP and ADP are known as mitochondrial function indices, so in this study, the lack of measurement of ADP/ATP ratio is another limitation of the present study. Therefore, it is suggested to evaluate more physiological and pathological parameters of mitochondria in future studies.

Acknowledgments

We sincerely appreciate all people who helped us in doing this project. There is no financial support and conflict of interest in this study.

Authors' Contributions

H.P., A.B.; Contributed to the conception and design, to all experimental work, data and statistical analysis, and interpretation of data. H.P.; Was responsible for overall supervision. B.A., O.R.S.; Drafted the manuscript, which was revised by H.P., A.B., B.A., OR.S. All authors read and approved the final manuscript.

References

1. Hosseini SA, Salehi O, Keikhosravi F, Hassanpour G, Ardakani HD, Farkhaie F, et al. Mental health benefits of exercise and genistein in elderly rats. Exp Aging Res. 2022; 48(1): 42-57.
2. Kim Y, Triolo M, Hood DA. Impact of aging and exercise on mitochondrial quality control in skeletal muscle. Oxid Med Cell Longev. 2017; 2017: 3165396.
3. Lanza IR, Short DK, Short KR, Raghavakaimal S, Basu R, Joyner MJ, et al. Endurance exercise as a countermeasure for aging. Diabetes. 2008; 57(11): 2933-2942.
4. Cho EJ, Choi Y, Jung SJ, Kwak HB. Role of exercise in estrogen deficiency-induced sarcopenia. J Exerc Rehabil. 2022; 18(1): 2-9.
5. Seo DY, Hwang BG. Effects of exercise training on the biochemical pathways associated with sarcopenia. Phys Act Nutr. 2020; 24(3): 32-38.
6. Sahin E, Colla S, Liesa M, Moslehi J, Müller FL, Guo M, et al. Telomere dysfunction induces metabolic and mitochondrial compromise. Nature. 2011; 470(7334): 359-365.
7. Chung MY, Choi HK, Hwang JT. AMPK activity: a primary target for diabetes prevention with therapeutic phytochemicals. Nutrients. 2021; 13(11): 4050.
8. Carapeto PV, Aguayo-Mazzucato C. Effects of exercise on cellular and tissue aging. Aging (Albany NY). 2021; 13(10): 14522-14543.
9. Torma F, Gombos Z, Jokai M, Takeda M, Mimura T, Radak Z. High intensity interval training and molecular adaptive response of skeletal muscle. Sports Med Health Sci. 2019; 1(1): 24-32.

10. Khalafi M, Mohebbi H, Karimi P, Faridnia M, Tabari E. The effect of high intensity interval training and moderate intensity continuous training on mitochondrial content and pgc-1α of subcutaneous adipose tissue in male rats with high fat diet induced obesity. Journal of Sport Biosciences. 2018; 10(3): 297-315.
11. Koltai E, Szabo Z, Atalay M, Boldogh I, Naito H, Goto S, et al. Exercise alters SIRT1, SIRT6, NAD and NAMPT levels in skeletal muscle of aged rats. Mech Ageing Dev. 2010; 131(1): 21-28.
12. Kramer HF, Goodyear LJ. Exercise, MAPK, and NF-κB signaling in skeletal muscle. J Appl Physiol. 2007; 103(1): 388-395.
13. Kang C, Chung E, Diffee G, Ji LL. Exercise training attenuates aging-associated mitochondrial dysfunction in rat skeletal muscle: role of PGC-1α. Exp Gerontol. 2013; 48(11): 1343-1350.
14. Egan B, Carson BP, Garcia-Roves PM, Chibalin AV, Sarsfield FM, Barron N, et al. Exercise intensity-dependent regulation of peroxisome proliferator-activated receptor γ coactivator-1α mRNA abundance is associated with differential activation of upstream signalling kinases in human skeletal muscle. J Physiol. 2010; 588(Pt 10): 1779-1790.
15. Sengupta P. The laboratory rat: relating its age with human's. Int J Prev Med. 2013; 4(6): 624-630.
16. Høydal MA, Wisløff U, Kemi OJ, Ellingsen O. Running speed and maximal oxygen uptake in rats and mice: practical implications for exercise training. Eur J Cardiovasc Prev Rehabil. 2007; 14(6): 753-760.
17. Huang CC, Wang T, Tung YT, Lin WT. Effect of exercise training on skeletal muscle SIRT1 and PGC-1α expression levels in rats of different age. Int J Med Sci. 2016; 13(4): 260-270.
18. Granata C, Oliveira RS, Little JP, Renner K, Bishop DJ. Mitochondrial adaptations to high-volume exercise training are rapidly reversed after a reduction in training volume in human skeletal muscle. FASEB J. 2016; 30(10): 3413-3423.
19. Petrocelli JJ, Drummond MJ. PGC-1α-targeted therapeutic approaches to enhance muscle recovery in aging. Int J Environ Res Public Health. 2020; 17(22): 8650.
20. O'Neill HM. AMPK and exercise: glucose uptake and insulin sensitivity. Diabetes Metab J. 2013; 37(1): 1-21.
21. Sharafi Dehrhm F, Soori R, Rastegar Mogaddam Mansouri M, Abbasian S. The effect of high intensity interval training on muscular biomarkers of mitochondrial biogenesis in male rats. J Babol Univ Med Sci. 2017; 19(6): 57-63.
22. Ebadi Ghahremani M, Tarverdizade B, Piri M, Agha Alinezhad H. The effect of continuous and interval muscular endurance traning on some cardiorespiratory variables and training runners' records. JSEP. 2014; 7(2): 1101-1112.
23. Mohammadi M, Siavoshi H, Naderi A, Panah Abadi M, Maleki M. A review of cardiac rehabilitation and exercise in cardiovascular disease. J Crit Rev. 2020; 7(1): 182-188.
24. Hadanny A, Hachmo Y, Rozali D, Catalogna M, Yaakobi E, Sova M, et al. Effects of hyperbaric oxygen therapy on mitochondrial respiration and physical performance in middle-aged athletes: a blinded, randomized controlled trial. Sports Med Open. 2022; 8(1): 1-12.
25. Gibala MJ, McGee SL, Garnham AP, Howlett KF, Snow RJ, Hargreaves M. Brief intense interval exercise activates AMPK and p38 MAPK signaling and increases the expression of PGC-1α in human skeletal muscle. J Appl Physiol. 2009; 106(3): 929-934.
26. Green HJ, Burnett M, Carter S, Jacobs I, Ranney D, Smith I, et al. Role of exercise duration on metabolic adaptations in working muscle to short-term moderate-to-heavy aerobic-based cycle training. Eur J Appl Physiol. 2013; 113(8): 1965-1978.
27. Suwa M, Nakano H, Radak Z, Kumagai S. Endurance exercise increases the SIRT1 and peroxisome proliferator-activated receptor gamma coactivator-1alpha protein expressions in rat skeletal muscle. Metabolism. 2008; 57(7): 986-998.

Cell J
Cell Journal(Yakhteh) Homepage: https://www.celljournal.org/
Original Article Vol 25, No 1, January 2023, Pages: 17-24

Nuclear Factor Kappa-B Protein Levels in Sperm of Obese Men with and without Diabetes; Cellular Approach in Male Infertility

Shima Abbasihormozi, Ph.D.[1, 2], Azam Kouhkan, M.D., Ph.D.[1], Abdolhossein Shahverdi, Ph.D.[1, 2], Mohammad Ali Sadighi Gilani, M.D.[3], Vahab Babapour, Ph.D.[4], Amir Niasari Naslji, Ph.D.[5], Vahid Akbarinehad, Ph.D.[5], AliReza Alizadeh, Ph.D.[2*]

1. Reproductive Epidemiology Research Center, Royan Institute for Reproductive Biomedicine, ACECR, Tehran, Iran
2. Department of Embryology, Reproductive Biomedicine Research Center, Royan Institute for Reproductive Biomedicine, ACECR, Tehran, Iran
3. Department of Andrology, Reproductive Biomedicine Research Center, Royan Institute for Reproductive Biomedicine, ACECR, Tehran, Iran
4. Department of Basic Science, Faculty of Veterinary Medicine, University of Tehran, Tehran, Iran
5. Department of Theriogenology, Faculty of Veterinary Medicine, University of Tehran, Tehran, Iran

**Corresponding Address: P.O.Box: 16635-148, Department of Embryology, Reproductive Biomedicine Research Center, Royan Institute for Reproductive Biomedicine, ACECR, Tehran, Iran*
Email: ar.alizadehmasouleh@royan-rc.ac.ir

Received: 10/July/2022, Revised: 15/October/2022, Accepted: 29/November/2022

Abstract

Objective: Although the role of obesity and diabetes mellitus (DM) in male infertility is well established, little information about the underlying cellular mechanisms in infertility is available. In this sense, nuclear factor kappa-B (NF-kB) has been recognized as an important regulator in obesity and DM; However, its function in the pathogenesis of male infertility has never been studied in obese or men who suffer from diabetes. Therefore, the main goal of current research is assessing NF-kB existence and activity in ejaculated human spermatozoa considering the obesity and diabetics condition of males.

Materials and Methods: In an experimental study, the ELISA technique was applied to analyze NF-kB levels in sperm of four experimental groups: non-obese none-diabetic men (body mass index (BMI) <25 kg/m^2; control group; n=30), obese non-diabetic men (BMI >30 kg/m^2; OB group; n=30), non-obese diabetic men (BMI <25 kg/m^2; DM group; n=30), and obese diabetic men (BMI >30 kg/m^2; OB-DM group; n=30) who were presented to Royan Institute Infertility Center. In addition, protein localization was shown by Immunocytofluorescent assay. Sperm features were also evaluated using CASA.

Results: The diabetic men were older than non-diabetic men regardless of obesity status (P=0.0002). Sperm progressive motility was affected by obesity (P=0.035) and type A sperm progressive motility was affected by DM (P=0.034). The concentration of sperm (P=0.013), motility (P=0.025) and morphology (P<0.0001) were altered by obesity × diabetes interaction effects. The NF-kB activity was negatively influenced by the main impact of diabetics (P=0.019). Obesity did not affect (P=0.248) NF-kB activity. Uniquely, NF-kB localized to the midpiece of sperm and post-acrosomal areas.

Conclusion: The current study indicated a lower concentration of NF-kB in diabetic men, no effect of obesity on NF-kB was observed yet. Additionally, we revealed the main obesity and diabetes effects, and their interaction effect adversely influenced sperm characteristics.

Keywords: Diabetes Mellitus, Nuclear factor kappa-B, Obesity Morbid, Spermatozoa, Type II

Citation: **Abbasihormozi Sh, Kouhkan A, Shahverdi AH, Sadighi Gilani MA, Babapour V, Niasari Naslji A, Akbarinehad V, Alizadeh AR. Nuclear factor kappa-B protein levels in sperm of obese men with and without diabetes; cellular approach in male infertility. Cell J. 2023; 25(1): 17-24. doi: 10.22074/CELLJ.2022.557547.1065.**

Introduction

Obesity and diabetes mellitus (DM) are the most prevalent health threats in several countries increasing rapidly. In addition, infertility caused by male factors is associated with diabetes and overweight/obesity (1). There seems to be mediated through complex mechanisms, including chronic systemic low-grade inflammation, insulin resistance, oxidative stress, and hyperleptinemia (2). More than 30 percent of the world's population suffers from obesity. Some sexual problems such as low-quality semen, erectile dysfunction, and subclinical prostatitis have been reported in obese men (3). Similarly, DM was introduced by excess blood sugar due to impaired insulin action. Negative effects of DM on pre-testicular, testicular, and post-testicular levels have been reported (4). Patients with hypogonadism develop through central hyperleptinemia or hypothalamic pulsatile GnRH secretion changes in overweight or obese patients (5) and Leydig cell function changes (6). Mechanisms that lead to the reduction of serum levels of testosterone. In addition, glucose metabolism plays an essential role in spermatogenesis, and numerous human and animal studies have confirmed the impacts of diabetes on male sexual function, seminal fluid parameters,

nuclear DNA, and chromatin quality (7).

The adverse effects of obesity and DM on male fertility are established well (1, 2), but little information on the mechanisms of molecular approaches and infertility problems in diabetic and obese patients is available (8). Therefore, the transcription factor activity found in sperm is part of the mechanisms involved in infertility or subfertility in obese or DM patients. Spermatozoa is a unique cell that experiences two different physiological and metabolic stages during its lifetime. In the reproductive tract, spermatozoa are quiescent cells while they become metabolically active after ejaculation (9). Increased expression of pro-inflammatory cytokines in adipose tissue of obese and DM patients, blood was the first indication that inflammatory mediators and obesity/diabetes were related (7). Recently, it has been hypothesized that high levels of pro-inflammatory factors in diabetic patients lead to the activation of nuclear factor-kappa-B (NF-kB), which mediates inflammatory and metabolic responses in part through cross-talk with peroxisomal proliferator-activated receptors (PPARs) (10). NF-kB is a major transcription factor that regulates genes responsible for the innate and adaptive immune response (11). It also plays an important role in regulating apoptosis in a germ cell of human testis tissue (12, 13). NF-kB activation under DM/obesity is a consequence of mild chronic inflammation, exposure to high glucose [advanced glycation end products: (AGEs)], and free fatty acids. NF-kB signaling and production of pro-inflammatory mediators in the liver contribute to insulin resistance in the early stages of DM, Whereas NF-kB activation in adipose tissue macrophages is required to propagate inflammation and promote systemic insulin resistance in muscle and other insulin-sensitive tissues, which is required for PPARγ in adipose tissue (14). While the crucial roles of PPARγ pointed out (15), scarce report exists on the NF-kB status and activity for sperm as well as male fertility (13, 16). According to the works of literature, the activity of NF-kB in spermatozoa of men with obesity or DM which may differ from that of obese men with DM has not been studied yet. With this background, the current study aimed to monitor NF-kB presence and activity in ejaculated human spermatozoa with a focus on the situations associated with DM and/or obesity.

Materials and Methods

Study population and experimental groups

After obtaining permission from the Ethics Committee of the National Institute of Medical Research Development (NIMAD), Tehran, Iran (IR.NIMAD.REC.1398.024), samples and demographic information were collected at the Royan Institute Infertility Center, a referral infertility clinic in Tehran, Iran. This experimental study, as part of a master plan, involved 120 Iranian men who attended Royan Institute including group I: control (n=30); men with normal weight and non-diabetes mellitus; group II: obese (BMI ≥ 30 kg/m^2; n=30) and non-diabetic mellitus men (Ob); group III: non-obese diabetic men (n=30) (Nob-DM); and group IV (n=30): obese diabetic men (Ob-DM). Diagnostic criteria for non-diabetic men were glucose levels below 110 mg/dL and HbA1C levels below 5.7%. Furthermore, the use of insulin was an exclusion criterion for diabetic men. Signed informed consent was obtained from all subjects to use their semen and personal information for research purposes.

After registration, a questionnaire containing demographic information, medical and drug history, smoking status, alcohol consumption, fertility history, and surgical history was completed by each participant. Men with a history of azoospermia, genital infections, varicocele, and debilitating chronic medical diseases (cerebrovascular, cardiovascular, sexually transmitted diseases, systemic diseases, and acute infections) were excluded from the study. BMI was calculated with the formula of weight/(height^2) (kgm^{2-}) and classified into normal weight (BMI 18-25 kg/m^2) and obese (BMI≥30 kg/m^2). All participants sustain a physical examination including anthropometric measurements (height and body weight, waist circumference (WC), and hip circumference (HC). WC and HC along with the ratio of waist to HC were also measured.

Collection and analysis of semen

Semen samples were collected after 2 to 5 days of sexual abstinence according to the World Health Organization (WHO 2010). Semen volume was measured with conical graduated tubes. The CASA system [Sperm Class Analyzer Software (SCATM, Microptic, version 4.2, Barcelona, Spain)] is used to assess sperm motility and concentration. The system consisted of a phase contrast microscope (Nikon™ Eclipse E-200, Japan) with a thermal plate. The Images were captured with a video camera (Basler Vision TecnologieTM A312FC, Ahrensburg, Germany) at 50 fps and 100x magnification. Haemocytometer method with counting chamber Neubauer improved bright lines by measuring sperm concentration in million/milliliters (M/mL) (Carl Roth™, Karlsruhe, Germany) (17). A Makler chamber was used for motility scoring. In this study, we only evaluated sperm progressive and general movements (18).

Blood sampling and analysis methods

Biochemical markers such as serum glucose concentration were measured using a standard enzymatic method (Roche Diagnostics GmbH, Mannheim, Germany). Serum insulin levels were measured using an electro-chemiluminescence immunoassay (ECLIA) kit (Roche Diagnostics GmbH, Mannheim, Germany). Glycosylated hemoglobin (HbA1C) was determined using the Nyco Card Reader II analyzer according to the manufactured instructions for use. Evaluation of the homeostasis model of insulin resistance (HOMR-IR) based on the formula: fasting insulin (microU/L)×fasting glucose (nmol/L)/22.5 was calculated.

NF-kB protein analysis and Immunocytofluorescent assay

For the detection of NF-kB protein levels, the validated method by ELISA was used (19). The total protein was extracted from equal amounts of cells (~1×10^7 sperm) in all samples using phosphate-buffered (PB). Sperm proteins were collected in the supernatant and concentrations were determined by a BCA protein assay kit (Thermo Fisher Scientific, USA). After that, the NF-kB /p65 Active ELISA kit was used to measure the binding activity of free NF-kB p65 in nuclear extracts. The analysis was performed using the sandwich ELISA method, according to the manufacturer's instructions. Supernatants containing the solubilized nuclear proteins were collected, and the quantity of NF-kB in the nuclear fractions was measured with an NF-kB p65 ELISA kit, (cat. no. ab176647; Abcam, Cambridge, UK) according to the manufacturer's instructions. For protein localization by Immunocytofluorescent Assay, sperm cells were washed in phosphate-buffered saline (PBS, Sigma, USA, 1X), and a uniform smear was prepared on Poly-L-Lysine coated slides. Cells were then fixed in paraformaldehyde 4% (w/v), washed in PBS-Tween 0.05% (v/v), permeabilized with Triton X-100 (0.5%) and resuspended in 10% (v/v) secondary host serum were blocked. Finally, primary and secondary antibodies were used. Also, a slide without a primary antibody was used as a negative control for each sample (9).

Statistical analysis

Quantitative variables were presented as mean ± standard deviation (SD). Qualitative variables were presented as percentages. Data were initially tested for normal distribution using the Kolmogorov-Smirnov test, and non-normally distributed data were log-transformed before analysis. The data of four groups (control, obese, diabetic and obese and diabetic) were analyzed using the General Linear Model (GLM) method of SAS software, in which the main and reciprocal effects of obesity and diabetes on the dependent variable were investigated (SAS 9.4). Multiple comparisons were performed using the LSMEENS statement. Differences at $P\leq0.05$ were considered significant.

Results

Comparison of age, BMI, waist circumference, hip circumference, waist-to-hip ratio (WHR), semen parameters, fasting blood sugar (FBS), hemoglobin A1c (HbA1C), Insulin, and NF-kB protein activity between experimental groups were shown in Table 1. The Obese group was younger than Non-DM and Ob-DM groups (P=0.0002). BMI (P<0.001), WC (P=0.003), and HC (P<0.001) of Obese as well as Ob-DM groups were higher than control and DM groups. However, the WHR was not changed (P=0.131). Sperm progressive motility was affected by obesity (P=0.035) and type A sperm progressive motility was affected by DM (P=0.034). Sperm concentration (P=0.013), motility (P=0.025) and morphology (P<0.0001) were altered by obesity × diabetes interaction effects. All men in diabetic groups had higher FBS (P<0.0001) and HbA1C (P<0.0001) levels. The main impact of obesity on the level of Insulin was significantly visible (P<0.0001). Obesity's main effect on beat-cross frequency (BCF) was significant (P=0.018). The levels of NF-kB activity were evaluated at 0.043, 0.033, 0.029, and 0.025 ng/ml for control, obese (ob), non-obese DM, and ob-DM groups. NF-kB concentrations were negatively influenced by diabetes (P=0.019) measured by ELISA (Fig.1). Obesity did not affect NF-kB activity (P=0.248). NF-kB localization has been also shown mainly in the sperm midpiece and post-acrosomal areas (Fig.2).

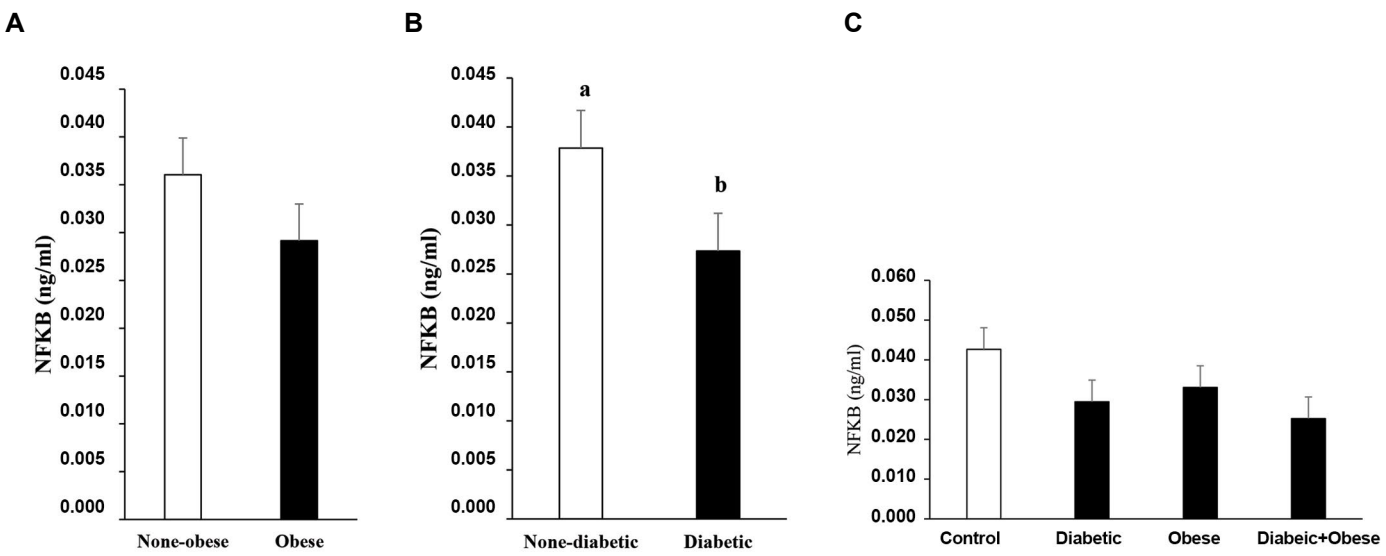

Fig.1: Nuclear factor kappa-B (NF-kB) protein activity in human spermatozoa. **A**. NF-kB protein content in obese vs. none-obese men (P=0.248). **B**. NF-kB protein content in diabetic vs. none-diabetic men (P=0.019). **C**. NF-kB protein content in experimental groups (P=0.52). [a,b]; Columns with different superscripts are different.

Table 1: Comparison of parameters in control (n=30): men with normal weight and non-diabetes mellitus; obese (BMI ≥30 kg/m^2; n=30) and non-diabetic mellitus men (Ob); non-obese diabetic men (Nob-DM; n=30); obese diabetic men (Ob-DM; n=30)

Variables	Experimental groups				P value		
	Control	Ob	Nob-DM	Ob-DM	Obesity	Diabetes	Obesity × diabetes
Age (Y)	31.30 ± 5.12[a]	32.97 ± 5.33[a]	39.33 ± 6.14[b]	39.20 ± 5.74[b]	0.455	**< 0.0001**	0.380
BMI (kg/m^2)	23.12 ± 1.26[a]	36.31 ± 4.67[b]	25.59 ± 1.89[c]	34.33 ± 4.22[b]	< 0.0001	0.687	**< 0.001**
Waist circumference (cm)	88.33 ± 4.65[a]	116.40 ± 11.91[b]	95.57 ± 8.05[c]	113.27 ± 10.39[b]	< 0001	0.223	**0.003**
Hip circumference (cm)	96.13 ± 3.70[a]	112.67 ± 22.79[b]	97.47 ± 16.99[a]	114.33 ± 7.74[b]	**< 0.0001**	0.581	0.951
Waist-to-hip ratio (WHR)	0.92 ± 0.05	1.33 ± 1.75	1.23 ± 1.54	0.99 ± 0.06	0.692	0.951	0.131
Concentration (million/ml)	75.73 ± 33.77[a]	45.04 ± 31.55[b]	51.28 ± 30.78[b]	50.77 ± 34.16[b]	0.010	0.119	**0.013**
Motility (%)	74.96 ± 14.65[a]	56.35 ± 24.57[b]	57.21 ± 25.55[b]	57.12 ± 22.61[b]	0.023	0.039	**0.025**
Morphology (%)	29.47 ± 11.33[a]	13.43 ± 13.15[b]	12.67 ± 8.77[b]	17.57 ± 12.10[b]	0.009	0.003	**< 0.0001**
Progressive motility (%)	49.64 ± 17.38	38.88 ± 25.01	38.75 ± 21.49	35.14 ± 18.89	**0.035**	0.159	0.141
Type A (%)	20.15 ± 12.15	16.29 ± 13.65	14.83 ± 10.48	12.47 ± 9.97	0.147	**0.034**	0.727
Type B (%)	28.02 ± 11.75	22.20 ± 15.87	24.39 ± 13.39	22.66 ± 11.58	0.122	0.514	0.401
Type C (%)	24.70 ± 7.93	20.71 ± 9.83	24.17 ± 20.02	23.67 ± 9.14	0.334	0.601	0.453
Type D (%)	27.14 ± 16.35	40.72 ± 24.11	52.70 ± 77.44	41.20 ± 21.44	0.894	0.098	0.111
VCL (µm/s)	55.87 ± 29.72	64.40 ± 36.38	48.73 ± 23.35	59.35 ± 27.18	0.081	0.264	0.848
VSL (µm/s)	25.78 ± 16.48	29.56 ± 17.85	21.18 ± 12.78	26.49 ± 14.69	0.115	0.183	0.790
VAP (µm/s)	35.73 ± 20.04	40.66 ± 22.56	30.36 ± 16.23	37.60 ± 19.13	0.095	0.245	0.750
LIN (%)	44.98 ± 6.52	44.63 ± 9.27	42.24 ± 10.18	43.54 ± 7.83	0.764	0.227	0.603
STR (%)	70.22 ± 7.27	70.37 ± 9.01	67.79 ± 9.38	68.75 ± 7.54	0.722	0.190	0.792
WOB (%)	63.90 ± 4.60	62.90 ± 6.27	61.47 ± 7.39	61.99 ± 6.75	0.836	0.155	0.515
ALH (µm)	2.33 ± 0.49	2.06 ± 0.73	2.06 ± 0.51	2.04 ± 0.52	0.178	0.172	0.239
BCF (Hz)	10.36 ± 4.42[ab]	12.34 ± 5.77[a]	9.01 ± 4.54[b]	11.34 ± 4.79[ab]	**0.018**	0.195	0.846
Fasting blood sugar (FBS) (mg/dl)	95.77 ± 10.65	98.70 ± 9.91	178.17 ± 76.78	156.50 ± 56.31	0.289	**< 0.0001**	0.164
HbA1C (%)	5.12 ± 0.63[a]	5.46 ± 0.59[a]	7.21 ± 1.91[b]	7.12 ± 1.69[b]	0.395	**< 0.0001**	0.315
Insulin (mU/L)	8.21 ± 3.26[a]	19.34 ± 10.68[b]	11.66 ± 12.21[a]	20.55 ± 10.46[b]	**< 0.0001**	0.443	0.803
NF-kB (ng/ml)	0.043 ± 0.032	0.033 ± 0.029	0.029 ± 0.031	0.025 ± 0.027	0.248	**0.019**	0.520

Data are presented as mean ± SD and they were analyzed using the general linear model (GLM) method. VCL; Curvilinear velocity, VSL; Straight-line velocity, VAP; Average path velocity, LIN; Linearity, STR; Straightness, WOB; Wobble, ALH; Amplitude of lateral head displacement, BCF; Beat-cross frequency, HbA1C; Glycosylated hemoglobin, NF-kB; Nuclear factor kappa-B. a, b, c; Values with different superscripts within rows differ. P values in bold were significant.

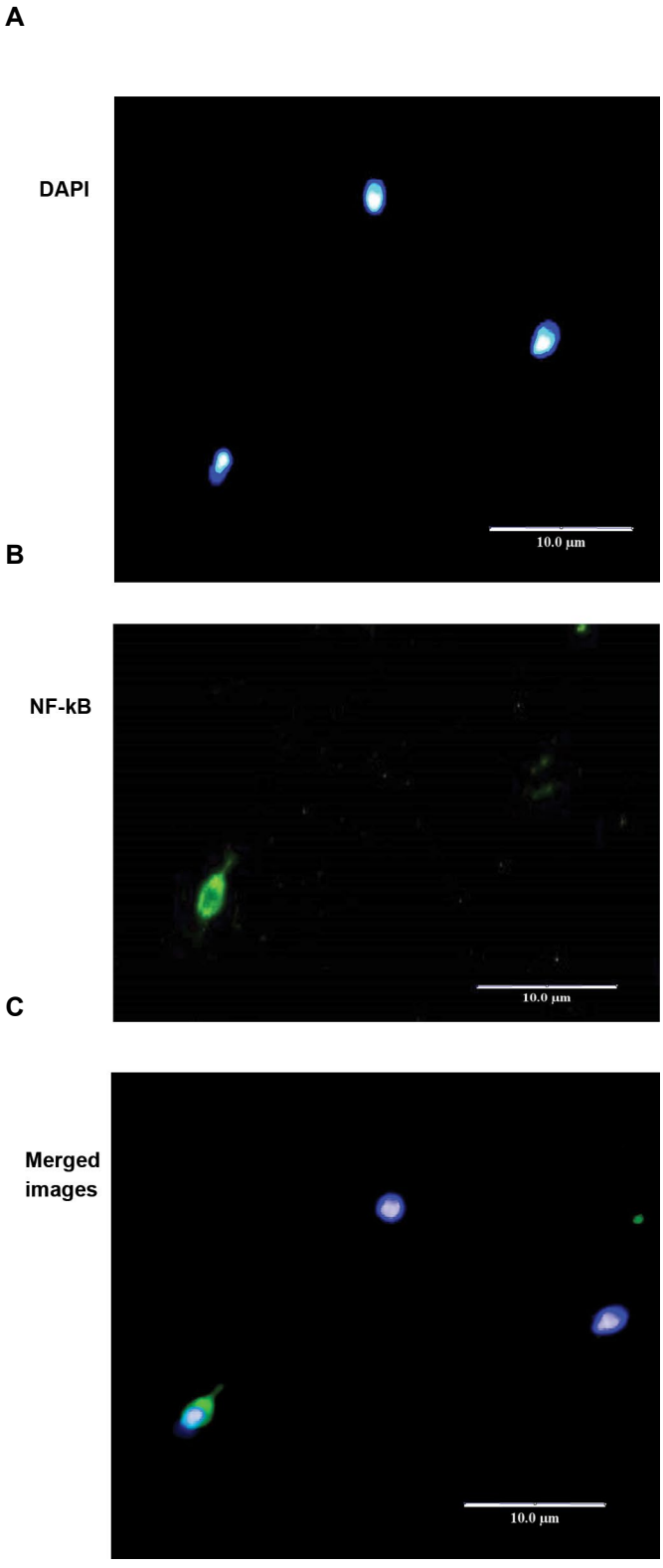

Fig.2: Nuclear factor kappa-B (NF-kB) protein localization by Immunocytofluorescent assay. **A-C.** Representative immunolocalization of NF-kB in ejaculated spermatozoa of a normozoospermic man. **A.** DAPI for nuclear staining. **B.** NF-kB detection. **C.** Merged images of A and B. NF-kB localized mainly to the sperm head and post-acrosomal regions.

Discussion

The current study provides convincing evidence for the active role of diabetes obesity or not on the level of NF-kB in the sperm of men referred to an infertility center. Based on the previous literature, obesity may not play a major role in NF-kB activity, however, in this study, the impact of diabetes on NF-kB activity is shown. While there are not many studies about the possible roles of NF-kB in male infertility, previously a published abstract represented NF-kB activity in sperm (16). For the first time in this study, by focusing on the NF-kB role in male infertility the negative impacts of obesity and diabetes on NF-kB activity in the sperm of obese and diabetic men were reported. Moreover, the results presented in the current study have shed a light on the exploration of other NF-kB roles in the sperm of diabetic men. The data of our study by providing a piece of strong evidence showed the value of monitoring men with diabetes as it may lead to their infertility. Therefore it would be valuable that refer these types of cases to infertility clinics after the diagnosis of DM. In this study, is shown that DM may exert different effects on NF-kB activity.

Recently, Zhong et al. (1) focused on the association of diabetes and obesity with sperm parameters. The mechanisms of obesity affecting semen quality include (17, 20): the first is male endocrine dysfunction, such as lower testosterone levels in obese men, which may be the main cause of decreased semen volume and total sperm concentration. The second is the damage of the inflammatory factors on the seminiferous epithelium of the testicular tissue, which ultimately leads to damage to the spermatogenesis process in obese men. Third, increasing oxidative stress may damage sperm structure and function, as high levels of reactive oxygen species (ROS) may attack sperm mitochondria and nuclei in obese men. On the other hand, DM mechanisms affecting semen quality included testicular and post-testicular levels (7). At the level of the testis, DM seems to cause: i. Increased oxidative stress by increasing the production of ROS in the seminal fluid and lipoperoxidation (LP), ii. Increasing the level of sperm DNA fragmentation, iii. Modification of sperm mitochondrial bioenergetics, and iv. End products of enzymatic glycation. In addition, possible post-testicular mechanisms may occur, as DM may cause sperm damage and prevent seminal fluid release by i. Infection/inflammation of the male parathyroid glands, where the association enhances the inflammatory response in the seminal fluid; and changes the normal parameters of sperm and causes it to increase more. Expansion of the inflammatory process and its chronicity and ii. Erectile and ejaculatory dysfunction, well-known complications of DM. It is surprising to note that NF-kB protein activity is an undertreated issue in diabetes and obese men.

While conflicting data on the effects of obesity and DM on seminal fluid volume and concentration have been reported (1), the adverse effects of obesity and DM on sperm motility were a common response. As a possible mechanism, it seems that the negative effects of the interaction of obesity and diabetes develop mitochondrial dysfunction and sperm motility reduction in the experimental groups in comparison with the normal group. Furthermore, our findings not only confirm the

deleterious effects of DM on the kinematic properties of human sperm, but also these data provide evidence that DM can effectively alter sperm motility in diabetic men with a BMI within the normal range. In an animal model, Abdel-Fadeil et al. (21) confirmed that obesity and diabetes in combination have more detrimental effects on male fertility than obesity alone in male rats. In contrast, a recent study concluded that obesity and diabetes in humans have a minor effect and are not harmful to male fertility (22). However, the important role of chronic inflammation in obesity and diabetes has been distinguished by a recent study (23).

As a possible mechanism, obesity impairs fertility and reproductive potential in men, particularly through alterations in the hypothalamic-pituitary-gonadal axis including sperm concentration, motility, viability, and normal morphology (3). Our data support this hypothesis when we compare the normal group with the obese group. Uniquely, BMI does not affect sperm quality, but rather reproductive hormone levels (24). Similarly, a meta-analysis that examined 20,367 obese and 1,386 diabetic patients reported that obesity and diabetes negatively affect sperm parameters in men and are associated with low testosterone levels (1). Although obesity, as well as diabetes, were expected to have deleterious effects, our findings in men with diabetes but normal BMI suggest that normal or low BMI may be a complication of diabetes. Considering a wide change in men's lifestyle, further investigation of molecular and cellular mechanisms in this group is necessary. For the first time in this study, while the tail is almost completely unstained in the NF-kB localization on human spermatozoa was represented in the midpiece and post-acrosomal regions. It has been hypothesized that high levels of pro-inflammatory factors in diabetic patients lead to the activation of NF-kB, which mediates inflammatory and metabolic responses in part through cross-talk with PPARs. As mentioned before, the localization of NF-kB was not reported in previous studies, however, Aquila et al. (25) and Mousavi et al. (9) studied on the localization of PPARγ in sperm and suggested a non-genomic signaling action in this particular cell type. Further studies on NF-kB seem to confirm that the multiple roles of NF-kB are location-dependent in the future.

Uniquely, Fan et al. (26) suggested that NF-kB should be considered in the chronic inflammation of obese men and they noted that signaling factors regulated by NF-kB were expressed at higher levels in the reproductive tract of obese men. In this study, NF-kB concentration in sperm was negatively affected by DM. The low level of NF-kB protein activity by ELISA in diabetic cases shows the critical role of DM on sperm. However, obesity may not play a significant role in the alternation of the level of NF-kB in sperm in our study. Similarly, a previous study using the ELISA technique to evaluate NF-kB protein activity in the sperm of infertile men investigated low levels of NF-kB in their sperm (16). On the other hand, previous studies focused on NF-kB activity in testes (13, 27) and there is little information about sperm. As a putative mechanism, increased levels of AGEs, its receptors (RAGE), oxidative stress, lipoproteins, and hyperlipidemia increase NF-kB expression through different pathways in subclinical/infertile diabetic men. Furthermore, inappropriate expression of NF-kB increases apoptosis and inflammatory process, that play a major role in cellular damage and subsequent complications (28). High levels of blood sugar cause oxidative stress and the formation of AGEs/RAGE in nerve cells, increasing glycated hemoglobin (HbAc1), and the level of stromal collagen in peripheral nerves, Schwann cells, and endoneurial vessels is another risk factor for the development of peripheral nerve damage (29). In contrast, our data support reduced NF-kB activation in sperm of DM men, which was confirmed by a previous study (16) that indicated a decrease of NF-kB activation in sperm. Meanwhile, the idea that different protein levels in different sub-fertile men serve as biomarkers is an exciting and emerging area for research and clinical studies. Hence, the cross-talk between diabetes and obesity on male infertility is important, and some biomarkers in sperm such as high mobility group protein 1 (HMGB1) (30), and mitochondrial uncoupling protein 2 (UCP2) (31) and it is considered special. PPARγ investigation may open the horizon for future interventions in diabetes and male infertility (32). Also, the level of several proteins in types of diabetes (type 1 and type 2) obesity or non-obesity is a subject that receives research and clinical attention.

Aging leads to adipose tissue dysfunction and thus systemic effects such as inflammation and low peripheral insulin sensitivity (33). Age matching of experimental groups can affect the results of such studies. Since the beginning of the survey, this has been one of our team's concerns and has been in the spotlight. There are always limitations in human research projects, and elderly men with diabetes are certainly one of them. Recently, older age in the diabetic group was shown in Iraq (22), which confirms our findings. In Iraqian study, the obese-diabetic group (43 years) was older than the control group (37 years). It is surprising to note that their control group was older than our control group. Therefore, we are faced with a challenge for age-matched of experimental groups in studies with diabetic men and controls in the infertility clinic, which needs more attention in future studies. Another limitation is the evaluation of NF-kB

protein phosphorylation in the current study, and we focused on net NF-kB protein activity by ELISA. In addition, future studies should focus on sperm DNA damage alongside NF-kB protein activity.

Conclusion

The current study indicated lower concentration and activation of NF-kB in diabetic men, while no effect of obesity on NF-kB activity was observed. Further, the present study revealed the main effects of obesity and diabetics, and their interactivity effect harmfully influenced sperm characteristics.

Acknowledgments

This research was supported by a grant for a young researcher from the National Institute for Medical Research Development (NIMAD) [Grant no. 972382]. We thank all the participants who participated in this study. We also would like to extend our appreciation to the Royan Institute laboratory staff, especially Mrs. Pegah Rahimizadeh for their sincere participation in all laboratory procedures. There is no conflict of interest in this study.

Authors' Contributions

S.A.; Main project contributor, investigation, data collection and analysis, writing- original draft preparation. A.K.; Contribution in designed this study focusing on NF-kB, interpreted the experimental data and writing- original draft preparation. A.S.; Methodology, confirmed the authenticity of all the raw data, writing- original draft preparation and visualization. M.A.S.G.; Project advisor, the head of team in clinic, methodology and participants selection. V.B.; Contributed to conception of NF-kB related mechanisms and manuscript drafting and revising. A.N.N.; Project advisor and manuscript revising. V.A.; Data analysis, methodology, writing- review and editing. A.A.; Principle investigator (PI) as the young researcher and project management regarding NF-kB and PPAR-gama at Royan Institute, study design, validation, writing- original draft preparation, writing and reviewing final version. All authors read and approved the final manuscript.

References

1. Zhong O, Ji L, Wang J, Lei X, Huang H. Association of diabetes and obesity with sperm parameters and testosterone levels: a meta-analysis. Diabetol Metab Syndr. 2021; 13(1): 109.
2. Carvalho MG, Silva KM, Aristizabal VHV, Ortiz PEO, Paranzini CS, Melchert A, et al. Effects of obesity and diabetes on sperm cell proteomics in rats. J Proteome Res. 2021; 20(5): 2628-2642.
3. Leisegang K, Sengupta P, Agarwal A, Henkel R. Obesity and male infertility: mechanisms and management. Andrologia. 2021; 53(1): e13617.
4. Sexton WJ, Jarow JP. Effect of diabetes mellitus upon male reproductive function. Urology. 1997; 49(4): 508-513.
5. Chan JL, Mantzoros CS. Leptin and the hypothalamic-pituitary regulation of the gonadotropin-gonadal axis. Pituitary. 2001; 4(1-2): 87-92.
6. Pitteloud N, Hardin M, Dwyer AA, Valassi E, Yialamas M, Elahi D, et al. Increasing insulin resistance is associated with a decrease in Leydig cell testosterone secretion in men. J Clin Endocrinol Metab. 2005; 90(5): 2636-2641.
7. Condorelli RA, La Vignera S, Mongioì LM, Alamo A, Calogero AE. Diabetes mellitus and infertility: different pathophysiological effects in type 1 and type 2 on sperm function. Front Endocrinol (Lausanne). 2018; 9: 268.
8. Abbasihormozi SH, Babapour V, Kouhkan A, Niasari Naslji A, Afraz K, Zolfaghary Z, et al. Stress hormone and oxidative stress biomarkers link obesity and diabetes with reduced fertility potential. Cell J. 2019; 21(3): 307-313.
9. Mousavi MS, Shahverdi A, Drevet J, Akbarinejad V, Esmaeili V, Sayahpour FA, et al. Peroxisome proliferator-activated receptors (PPARs) levels in spermatozoa of normozoospermic and asthenozoospermic men. Syst Biol Reprod Med. 2019; 65(6): 409-419.
10. Naeini Z, Toupchian O, Vatannejad A, Sotoudeh G, Teimouri M, Ghorbani M, et al. Effects of DHA-enriched fish oil on gene expression levels of p53 and NF-κB and PPAR-γ activity in PBMCs of patients with T2DM: a randomized, double-blind, clinical trial. Nutr Metab Cardiovasc Dis. 2020; 30(3): 441-447.
11. Serasanambati M, Chilakapati SR. Function of nuclear factor kappa B (NF-kB) in human diseases-a review. South Indian J Biol Sci. 2016; 2(4): 368-387.
12. El-Hoseny R, Neamatallah M, Alghobary M, Zalata A, Comhaire F, El-Beah SM. The possible role of NF-κB1 Rs28362491 polymorphism in male fertility of Egyptian population. Andrologia. 2020; 52(7): e13659.
13. Pentikäinen V, Suomalainen L, Erkkilä K, Martelin E, Parvinen M, Pentikäinen MO, et al. Nuclear factor-kappa B activation in human testicular apoptosis. Am J Pathol. 2002; 160(1): 205-218.
14. Catrysse L, van Loo G. Inflammation and the metabolic syndrome: the tissue-specific functions of NF-κB. Trends Cell Biol. 2017; 27(6): 417-429.
15. Santoro M, De Amicis F, Aquila S, Bonofiglio D. Peroxisome proliferator-activated receptor gamma expression along the male genital system and its role in male fertility. Hum Reprod. 2020; 35(9): 2072-2085.
16. Ranganathan P, Kattal N, Moustafa MH, Sharma RK, Thomas AJ, Agarwal A. Correlation of nuclear factor KAPPA B (NFKB) with sperm quality and clinical diagnoses in infertile men. Fertil Steril. 2002; 78(1): S95.
17. Esmaeili V, Zendehdel M, Shahverdi A, Alizadeh A. Relationship between obesity-related markers, biochemical metabolic parameters, hormonal profiles and sperm parameters among men attending an infertility clinic. Andrologia. 2022; 54(1): e14524.
18. Abbasihormozi S, Kouhkan A, Alizadeh AR, Shahverdi AH, Nasr-Esfahani MH, Sadighi Gilani M A, et al. Association of vitamin D status with semen quality and reproductive hormones in Iranian subfertile men. Andrology. 2017; 5(1): 113-118.
19. Ernst O, Vayttaden SJ, Fraser IDC. Measurement of NF-κB activation in TLR-activated macrophages. Methods Mol Biol. 2018; 1714: 67-78.
20. Wang S, Sun J, Wang J, Ping Z, Liu L. Does obesity based on body mass index affect semen quality?-A meta-analysis and systematic review from the general population rather than the infertile population. Andrologia. 2021; 53(7): e14099.
21. Abdel-Fadeil MR, Abd Allah ESH, Iraqy HM, Elgamal DA, Abdel-Ghani MA. Experimental obesity and diabetes reduce male fertility: potential involvement of hypothalamic Kiss-1, pituitary nitric oxide, serum vaspin and visfatin. Pathophysiology. 2019; 26(3-4): 181-189.
22. Mohammad MHS, Ameen EM. Impact of diabetes and obesity on human fertility and semen quality. Zanco J Pure Appl Sci T. 2021; 33(1): 42-54.
23. Leisegang K, Henkel R, Agarwal A. Obesity and metabolic syndrome associated with systemic inflammation and the impact on the male reproductive system. Am J Reprod Immunol. 2019; 82(5): e13178.
24. Al-Ali MB, Gutschi T, Pummer K, Zigeuner R, Brookman-May S, Wieland WF, et al. Body mass index has no impact on sperm quality but on reproductive hormones levels. Andrologia. 2014; 46(2): 106-111.
25. Aquila S, Bonofiglio D, Gentile M, Middea E, Gabriele S, Belmonte M, et al. Peroxisome proliferator-activated receptor

(PPAR)gamma is expressed by human spermatozoa: its potential role on the sperm physiology. J Cell Physiol. 2006; 209(3): 977-986.
26. Fan W, Xu Y, Liu Y, Zhang Z, Lu L, Ding Z. Obesity or overweight, a chronic inflammatory status in male reproductive system, leads to mice and human subfertility. Front Physiol. 2018; 8: 1117.
27. Özata DM, Li X, Lee L, Liu J, Warsito D, Hajeri P, et al. Loss of miR-514a-3p regulation of PEG3 activates the NF-kappa B pathway in human testicular germ cell tumors. Cell Death Dis. 2017; 8(5): e2759.
28. Singh VP, Bali A, Singh N, Jaggi AS. Advanced glycation end products and diabetic complications. Korean J Physiol Pharmacol. 2014; 18(1): 1-14.
29. Lv X, Lv GH, Dai GY, Sun HM, Xu HQ. Food-advanced glycation end products aggravate the diabetic vascular complications via modulating the AGEs/RAGE pathway. Chin J Nat Med. 2016; 14(11): 844-855.
30. Biscetti F, Rando MM, Nardella E, Cecchini AL, Pecorini G, Landolfi R, et al. High mobility group Box-1 and diabetes mellitus complications: state of the art and future perspectives. Int J Mol Sci. 2019; 20(24): 6258.
31. Li J, Jiang R, Cong X, Zhao Y. UCP2 gene polymorphisms in obesity and diabetes, and the role of UCP2 in cancer. FEBS Lett. 2019; 593(18): 2525-2534.
32. Cataldi S, Costa V, Ciccodicola A, Aprile M. PPARγ and diabetes: beyond the genome and towards personalized medicine. Curr Diab Rep. 2021; 21(6): 18.
33. Crowley CA, Smith WPW, Seah KTM, Lim SK, Khan WS. Cryopreservation of human adipose tissues and adipose-derived stem cells with DMSO and/or trehalose: a systematic review. Cells. 2021; 10(7): 1837.

Cell J
Cell Journal(Yakhteh) Homepage: https://www.celljournal.org/
Original Article Vol 25, No 1, January 2023, Pages: 25-34

A Combination of Physical and Chemical Treatments Is More Effective in The Preparation of Acellular Uterine Scaffolds

Masoomeh Masoomikarimi, Ph.D.[1], Majid Salehi, Ph.D.[2, 3*], Farshid Noorbakhsh, Ph.D.[1], Samira Rajaei, Ph.D.[1*]

1. Department of Immunology, School of Medicine, Tehran University of Medical Sciences, Tehran, Iran
2. Department of Tissue Engineering, School of Medicine, Shahroud, University of Medical Sciences, Shahroud, Iran
3. Sexual Health and Fertility Research Center, University of Medical Sciences, Shahroud, Iran

**Corresponding Addresses: P.O.Box: 3614773943, Department of Tissue Engineering, School of Medicine, Shahroud University of Medical Sciences, Shahroud, Iran*

P.O.Box: 1417653761, Department of Immunology, School of Medicine, Tehran University of Medical Sciences, Tehran, Iran
Emails: msalehi.te1392@sshmu.ac.ir, s-rajaei@tums.ac.ir

Received: 28/December/2021, Revised: 05/April/2022, Accepted: 16/May/2022

Abstract

Objective: Decellularized uterine scaffold, as a new achievement in tissue engineering, enables recellularization and regeneration of uterine tissues and supports pregnancy in a fashion comparable to the intact uterus. The acellular methods are methods preferred in many respects due to their similarity to normal tissue, so it is necessary to try to introduce an acellularization protocol with minimum disadvantages and maximum advantages. Therefore, this study aimed to compare different protocols to achieve the optimal uterus decellularization method for future *in vitro* and *in vivo* bioengineering experiments.

Materials and Methods: In this experimental study, rat uteri were decellularized by four different protocols (P) using sodium dodecyl sulfate (SDS), with different doses and time incubations (P1 and P2), SDS/Triton-X100 sequentially (P3), and a combination of physical (freeze/thaw) and chemical reagents (SDS/Triton X-100). The scaffolds were examined by histopathological staining, DNA quantification, MTT assay, blood compatibility assay, FESEM, and mechanical studies.

Results: Histology assessment showed that only in P4, cell residues were completely removed. Masson's trichrome staining demonstrated that in P3, collagen fibers were decreased; however, no damage was observed in the collagen bundles using other protocols. In indirect MTT assays, cell viabilities achieved by all used protocols were significantly higher than the native samples. The percentage of red blood cell (RBC) hemolysis in the presence of prepared scaffolds from all 4 protocols was less than 2%. The mechanical properties of none of the obtained scaffolds were significantly different from the native sample except for P3.

Conclusion: Uteri decellularized with a combination of physical and chemical treatments (P4) was the most favorable treatment in our study with the complete removal of cell residue, preservation of the three-dimensional structure, complete removal of detergents, and preservation of the mechanical property of the scaffolds.

Keywords: Acellularization, Female Infertility, Rat Uterus, Sodium Dodecyl Sulfate, Tissue Engineering

Citation: **Masoomikarimi M, Salehi M, Noorbakhsh F, Rajaei S. A Combination of physical and chemical treatments is more effective in the preparation of acellular uterine scaffolds. Cell J. 2023; 25(1): 25-34. doi: 10.22074/cellj.2022.8396.**

Introduction

Absolute uterine factor infertility (AUFI) is one of the infertility causes, which refers to the absence or dysfunction of the uterus and has a prevalence of one in every 500 women of fertile age (1). Currently, the only solution available is gestational surrogacy, which comes with its own set of economic, legal, and ethical challenges (2). While organ transplantation has been proposed as a solution, due to the scarce availability of human organs and immunogenic effects, many investigators have been directed towards the utilization or development of bioengineered tissue by a synthetic mold or acellularized scaffold to restore fertility. This approach takes advantage of the body's inherent ability to regenerate organs, and repairs the defect of reproductive organs with a combination of cells, growth factors, and biological materials with repairing (3). So far, many studies have used biodegradable polymer scaffolds [such as poly-DL-lactide-coglycolide (PLGA)-coated polyglycolic acid (PGA) (4)], collagen/matrigel (5), silk-coated collagen (6), or boiled blood clots (7). Despite the excellent mechanical support and stability of synthetic scaffolds, decellularized extracellular matrix (ECM) of the target tissue is one of the preferred methods of engineered tissue. The main benefit of this method is the minimized immune system reactions (due to the removal of membrane antigen epitopes and intracellular derivatives) as well as functional, mechanical, and structural similarities to the native tissues (8).

The use of decellularized scaffolds for the engineering of vital organs such as kidneys (9), heart (whole organ) (10), blood vessels (whole organ) (11), and bone (12) have been reported. This technique already has been transferred to clinical trials (13).

Several methods have been tested to remove cells from the ECM (14-17). Physical treatments such as freeze-thawing procedures, sonication, agitation, mechanical

pressure, and enzymatic treatment (using dispase, trypsin, esterases, or nucleases) have also been employed to remove cells from tissues (14, 18). Due to the diversity of cell morphology, matrix thickness, and variable density from organ to organ, the optimal acellularization method is unique to each tissue (17). The methods used to produce uterine tissue ECM scaffolds show distinct effects on the structural and functional components of the scaffold material preparation, some of which even have adverse effects on immunological, structural, and mechanical properties (19). Therefore, introducing an efficient decellularization protocol for tissue engineering of the uterine is very necessary.

Detergents are effective in removing nuclear remnants and cytoplasmic proteins from tissues, but their optimum dose and exposure time are important for tissue properties. White et al. (20) showed increasing sodium dodecyl sulfate (SDS) concentrations from 0.1% to 1.0% increased both the intensity of SDS fragments and adverse cell outcomes. Most studies have used detergents to remove cells from uterine tissue, and there are fewer reports of combining these methods with other methods, such as mechanical cell removal, so we developed four decellularisation protocols, In the first three protocols, only detergent (chemical) was used, but in the fourth, a combination of physical (freeze/thaw) and chemical reagents was used. Therefore, we evaluated the decellularization efficacy of each method using different methods such as H&E which evaluates cell component removal, mechanical testing for ECM structure preservation, MTT for detergent removal, and so on. We aimed to determine which method was advantageous in cell removal and preserving the ECM components, structure, and mechanical properties of natural uterine for an ideal scaffold for tissue engineering.

Materials and Methods

Animals

All animals used in this experimental study were housed in the animal house facility according to the institutional ethical guidelines for using laboratory animals.

Fifty rats were randomly divided into five groups (n=10 per group). Female Wistar rats were put down, 9-16 weeks old and weighing 180-200 g, in an estrous cycle (which was characterized by the presence of abundant anucleated cornified epithelial cells in the cytology of vaginal smear) (21). Rats were anesthetized with an injection of ketamine (70 mg/kg) and xylazine (6 mg/kg) via the intraperitoneal (IP) route (22).

Acellularization of uterine tissue samples

Four different protocols (P1, P2, P3, and P4) were utilized for the decellularization of uterine tissues.

Protocols 1 and 2 (P1 and P2)

Rats were deeply anesthetised, uterine horns were excised, and connective tissues and fats were removed. Briefly, the horns were rinsed with phosphate-buffered saline (PBS, 25°C) incised in the mesometrium line and cut into rectangular pieces that varied in size depending on the test. Up to four samples from the same rat were immersed in 5 ml of SDS (1%) solution for 2 hours (P1) or 4 hours (P2) at room temperature. After SDS treatment, samples were washed for 1 week (P1) or 10 days (P2) using a washing buffer containing 0.05 M magnesium chloride hexahydrate, 0.2 mg/ml DNaseI (Roche, USA), 0.9% NaCl, and 1% penicillin and streptomycin on a shaker at 4°C (Table 1).

Protocol 3 (P3)

To prevent blood clots in the arteries during perfusion, rats were injected subcutaneously with heparin (100 IU/kg) one hour before anesthesia. Subsequently, the abdominal aorta was cannulated with a 20-G angiocatheter and cannulas were fixed with the 4-0 silk ligatures. The uterus was connected to 200 ml of heparin/PBS solution (50 IU/ml) and 200 ml PBS, respectively, and the volumetric flow rate was set at 4 ml/minutes. Then, their connection was cut off from the solution flow, and uterine horns were cut into rectangular samples. Uterine patches were soaked in three different doses of SDS (0.01%, 0.1%, and 1% in distilled water), respectively (the time of each dose was 24 hours). Samples were washed with PBS every 24 hours (3 times, 5 minutes, on a shaker) and finally soaked in 1% of Triton X100 for 30 minutes. In the end, the samples were washed with PBS (3 times, 10 minutes, on the shaker) (Table 1).

Protocol 4 (P4)

One hour before anesthesia, rats were injected subcutaneously with 100 IU/kg of heparin. Rats were anesthetised, and the diaphragm was dissected. Then ribs were cut, and a 50 ml syringe filled with NaCl was inserted in the left ventricle of the heart. The right atrium was cut to allow the flow. Subsequently, 200 ml of NaCl was slowly injected to remove the blood from the uterine tissue (until the lung tissue became white). Uterine horns were excised, connective tissue and fat were removed, and rinsed with PBS. The uterus was frozen at -20°C for 1 to 7 days. Next, the uterus was thawed, and one of the horns was attached to a peristaltic pump using a pipette tip and silicon tubing. Initially, perfusion with PBS was performed for one hour to remove cell debris. The perfusion speed was set at a flow rate of 10 ml/minutes. Then, five 24-hour cycles were performed. In the first two days, the cycle of SDS 1% (6 hours) and PBS (18 hours) was repeated. On the third day, the SDS time was reduced to 2 hours, the samples were treated with Triton X-100(1%) for 2 hours, and then PBS flowed for 20 hours, and this cycle was repeated until the fifth day (Table 1).

Table 1: Decellularization protocols

1.1: Decellularization protocol 1 and 2			
Stages		Protocol 1	Protocol 2
SDS 1% (25°C)		2 hours	4 hours
Washing buffer		1 week	10 days
1.2: Decellularization protocol 3			
Perfusion of heparin/PBS (50 IU/ml, 200 ml)			
Perfusion of PBS (200 ml)			
SDS 0.01%			24 hours
PBS			5 minutes (3 times)
SDS 0.1%			24 hours
PBS			5 minutes (3 times)
SDS 1%			24 hours
PBS			5 minutes (3 times)
Triton X100 1%			30 minutes
PBS			10 minutes (3 times)
1.3: Decellularization protocol 4			
Perfusion of NaCl (200 ml) into the left ventricle			
Physical treatment	Freeze/thawing of the uterus (at -20°C)		
Chemical treatment	Day 1	PBS	1 hour
		SDS 1%	6 hours
		PBS	18 hours
	Day 2	SDS 1%	6 hours
		PBS	18 hours
	Day 3	SDS 1%	2 hours
		PBS	10 minutes
		Triton X100 1%	2 hours
		PBS	20 hours
	Day 4	SDS 1%	2 hours
		PBS	10 minutes
		Triton X100 1%	2 hours
		PBS	20 hours
	Day 5	SDS 1%	2 hours
		PBS	10 minutes
		Triton X100 1%	2 hours
		PBS	20 hours

SDS; Sodium dodecyl sulfate and PBS; Phosphate-buffered saline.

Histological analysis

The presented cellular component and collagen fibers were evaluated by H&E and MT staining, respectively. To prevent any ECM breakdown, the segments of native and acellularized samples were fixed in 10% formalin for 24 hours. Subsequently, they were incubated in 70% ethanol at 4°C overnight and then dehydrated in graded alcohols. This was followed by immersion in xylene and embedding in paraffin wax. The paraffin-embedded tissues were cut into 5-µm slices and stained with H&E (23) and MT (24), using standard protocols.

DNA quantification

The efficacy of the acellularization process and the presence of nuclear materials were evaluated by measuring the remaining nuclear DNA. The native and acellular samples were dried using a freeze dryer (Zibrus vaco2, Germany) to remove the liquid and then, weighed less than 20 mg. The total DNA content was extracted using a commercial kit (DNeasy Blood & Tissue, Qiagen, Cat No. ID: 69504) as per the protocol provided. DNA concentration was calculated from OD measurements at 260 nm by picodrop (pico100, UK).

FESEM imaging

We performed FESEM to investigate the ultrastructure of the scaffolds in different protocols. To prepare the samples for FESEM imaging, we provided 0.5×5 cm^3 patches from the horns of native and acellular uteri of rats. The samples were first immersed in 2.5% glutaraldehyde solution at 4°C for 2 hours, washed with distilled water (DW) three times, and were dehydrated by graded series of ethanol (30, 50, 70, 90, 100%) each for 15 minutes and then dried with a freeze dryer (25). The samples were ultimately put under a scanning electron microscope (ZEISS Sigma 300 HV, Germany) following coating with the gold sputter-coater.

Cytotoxicity assay

Sample preparation

To ensure the complete removal of detergents from the scaffolds and to evaluate the cytotoxicity of the acellular scaffolds, equal-weighted round patches with 5 mm diameter were prepared. Patches were sterilized with 70% ethanol (24 hours) and washed in sterile PBS for the next 24 hours.

Cell culture

Rabbit mesenchymal stem cells (Ra-MSC) was purchased from the Iranian Biological Resource Center with accession cell No: IBRC C10723 which was confirmed as a rabbit by polymerasde chain reaction (PCR) method. Cryopreserved MSCs were thawed in a 37ºC water bath. To improve cell viability, MSCs were put in a complete medium consisting of 10% fetal bovine serum (FBS, Gibco, USA) and 1% pen/strep. The cell-medium suspension was centrifuged at 2500 rpm for 10 minutes. The supernatant was recovered, and the pellet was resuspended in a 1 ml complete medium. After that, cells were counted by a hemocytometer and were seeded into a T25 or T75 flask at 5×10^4 cells/flask (T25) or 1×10^6 cells per T75 flask and incubated at 37ºC and 5% CO_2. Every 3 days, the complete medium was changed. When the cells reached 80% confluency, they were ready for harvesting.

Direct MTT

Acellular scaffolds were put into a 96-well plate, and MSCs were seeded onto the scaffolds at the density of 2×10^4/w. The fresh culture medium containing Dulbecco's Modified Eagle Medium (DMEM, Gibco, USA) with 10% FBS and 1% penicillin/streptomycin was added to cell-seeded scaffolds. Cell viability was monitored 1st and 3rd day of culturing by MTT assay. In brief, after the prescribed period of incubation, the supernatant was removed, and the wells were washed twice with PBS. After that, 100 µL of MTT (0.5 mg/ml in PBS, Sigma Aldrich, USA) was added to each well and left on the plate for 4 hours at 37°C and a 5% CO_2 incubator. Then dimethyl sulfoxide (DMSO, DNAbiotech, Iran, 100 µL) was added to each well and allowed to react until the dissolution of the formazan pigment. The scaffolds were then removed, and their optical densities (ODs) were measured at 570 and 650 nm (as a reference wavelength) in a spectrophotometer.

The OD of the treated wells was compared with that of the control, which consisted of MSCs without any scaffold and the cell viability percentage was calculated according to the following formulas.

Equation (1): Viability=(OD sample–OD blank)/(OD control–OD blank)×100

Indirect MTT

MSCs were seeded onto wells of flat-bottomed 96-well plates at 10^4 cells/well. After 24 hours (to ensure the adherence of cells to wells), the acellularized scaffolds were added to the wells and incubated at 37°C for 24 or 72 hours. Thereafter, the scaffolds were removed from each well and the culture medium was discarded. MTT (100 µL, 0.5 mg/mL) was added to each well and the plates were incubated for 4 hours at 37°C. Then dimethyl sulfoxide was added, and the OD was measured like what we explained above (direct MTT).

Hemolysis assay

The effect of an acellularized uterine sample on red blood

cells (RBC) was determined by a hemolysis assay. Firstly, patches of uterine from all of the acellular protocols were cut (15 mg) and added to sample tube containing 4 ml NaCl 0.9% and preheated in a 37°C incubator for 30 minutes. Two tubes containing 4 ml NaCl 0.9%, and DW were considered as negative and positive control, respectively. Two ml of citrated blood were diluted with 2.5 mL NaCl 0.9%. Diluted blood (200 µl) was added to all sample and control tubes, and the tubes were replaced at 37°C for a further 60 minutes. The tubes were centrifuged at 1500 RPM for 10 minutes following the second incubation period. Release of hemoglobin which indicates the RBC damage was determined by photometric analysis of the supernatant at 545 nm (O.D). The percent hemolysis was calculated using the following formula.

% Hemolysis=(TS–NC)/(PC-NC)×100

TS: Absorbance of supernatant of erythrocyte suspension with the sample solution

NC: Absorbance of supernatant of erythrocyte suspension with NaCl

PC: Absorbance of supernatant of erythrocyte suspension with distilled water

This test was run in triplicate and the results were averaged.

Mechanical characterization

The mechanical properties or tensile test of the native tissue and acellularized scaffolds were conducted using a universal tensile machine (UTM) equipped with a 50-N load cell (Zwick/Roell, Model: Hct 25-400, Germany). Wet tissue samples (20 mm in length×5 mm in width) were pulled at a rate of 10 mm/minutes, displacement data were recorded, and a stress-strain curve was drawn. The tests were performed with three replicates for each sample (n=3). The ultimate tensile strength (UTS), Young's modulus (E), and Elongation at break ($\boldsymbol{\delta}$) were calculated using the following formula:

Equation (2): $E=(F/A)/(\Delta L/L0)$

Equation (3): $UTS=F/A$

Equation (4): $\%\boldsymbol{\delta} = \Delta L/L0$

E=Young's modulus (Elastic Modulus)

$\boldsymbol{\delta}$=Elongation at break

F=Force exerted on an object under tension

A=Cross-sectional area

ΔL=Changes in length

L0=Initial length

Statistical analysis

The data were analyzed by SPSS software (version 23, IBM, USA) using the ANOVA test. Data were expressed as mean ± standard deviation, and a $P<0.05$ was considered as the significance level.

Ethical consideration

The experimental procedures were approved by the Animal Ethics Committee of Tehran University of Medical Sciences (IR.TUMS.MEDICINE.REC.1398.298).

Results

Histological evaluation

Investigation of acellularization efficiency in four different protocols by H&E staining demonstrated that only the P4 successfully removed cellular components in all epithelial, stromal, and smooth muscle layers. The samples processed by P1 and P2 showed the most residual cells compared to the others. In scaffolds obtained from P3, the nucleus of cells was removed but some cytoplasmic components remained. In the H&E staining the nuclei were purple and cytoplasmic components were pink, indicating the cytoplasmic components were not removed. Native uterine tissue was used as the control sample (Fig.1AI, II). Masson's trichrome staining showed that P1, P2, and P4 samples had an abundance of collagen fibers, similar to native tissue, that indicates no damage of detergents to the ECM; however, P3 specimens showed slightly reduced collagen fibers (Fig.1AIII).

DNA quantification

DNA quantification is an assay for assessing the efficiency of cell removal protocol. DNA content of samples was reported as a percentage of normal (intact) tissue. The remaining DNA contents of all the protocols were significantly lower than native tissues, while P1 samples showed the highest amount of DNA remnants after the decellularization process compared to other protocols ($P<0.05$, Fig.1B).

FESEM results

As observed in the low magnification of FESEM images, the scaffolds, after acellularization by P1, P2, and P4 protocols, appeared as porous sponges with a well-defined three-dimensional structure. Even the structure of the vascular conduits in protocol 4 was preserved with intact conformation. Although scaffolds prepared using P1 and P2 protocol looked rich in fibrous content, P4 appeared more porous than other decellularization scaffolds. P3 became collapsed in all layers and showed poor porous structure (Fig.2A, B). Cross-sections of the native uterus and acellular scaffolds from each protocol viewed at high

magnification showed tissue fibrils (e. g. collagen and elastin) that maintained their striated and bundle patterns (Fig.2C).

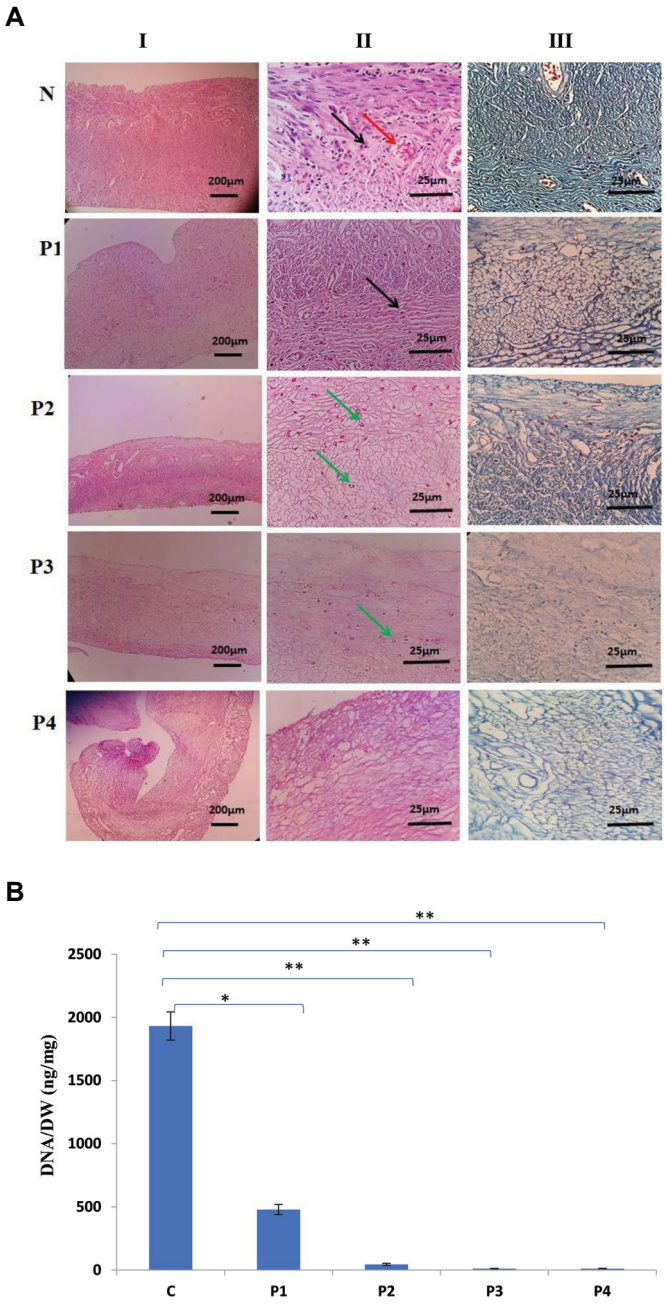

Fig.1: Verification of decellularization by histological staining and residual DNA content. **A.** Histological assessment of decellularized uterine scaffolds (with different protocols; P1, P2, P3, P4) and native tissue (N). Optical microscope images of hematoxylin-eosin staining indicate cells (I and II) (black arrowhead) in the layers of native (N) samples and blood cells in their arteries (red arrowhead). In P1 and P2 protocols, the cells were partially removed; however, some cytoplasm without a nucleus remained (green arrowhead). Also, in protocol 3, the cytoplasm without a nucleus is seen. Only in protocol 4, the cells are completely removed. III; Masson's trichrome staining demonstrated that there is no damage in the collagen fibers of the scaffold from P1, P2, and P4 following the decellularization process but in scaffolds obtained from P3, fibers are decreased (I; 10x magnification, II and III; 40x magnification). **B.** Quantification of residual DNA showing a drop of 24, 2.3, 0.5, and 0.6% for the protocols 1-4 respectively compared to native sample (100%). *; $P=1.1\times10^{-10}$, **; $P=2\times10^{-12}$, and DW; Dry weight.

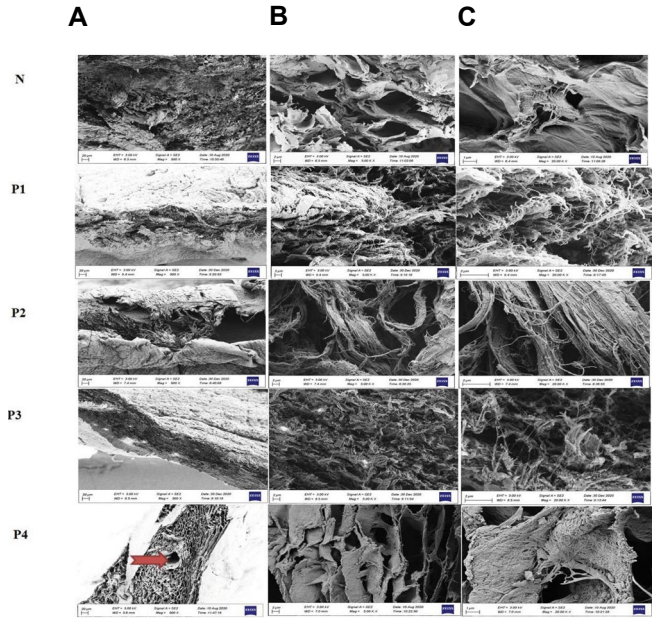

Fig.2: Scanning electron microscope images of the cross-section of native (N) and acellularized protocols (P1-P4) of rat uterine tissues. **A, B.** Scanning electron micrographs at lower magnification (200 and 5000x magnification) showing pores of scaffolds. **C.** Higher magnification (20000x magnification) demonstrates the fibers bundles. Arrowhead indicates blood vessel.

MTT assay results

Because incomplete removal of detergents from a scaffold can affect cell viability *in vitro* and *in vivo*, we evaluated the biocompatibility of scaffold by MTT assay. In the direct method, the cell viability of MSCs that were seeded on all the P1, P2, P3, and P4 acellular scaffolds was significantly higher than in the scaffold-free control group (Fig.3A). In indirect contact of the scaffold with MSCs, no significant decrease was seen in cell viability compared with the control samples at 24 and 72 hours (Fig.3B).

Hemocompatibility

Results obtained for hemolysis of citrated blood with acellularized uterine patches are shown in Table 2. The percentage of hemolysis in the presence of uterine scaffolds prepared from all of the protocols was less than 2%. According to the Autian report (26), when the material presents a hemolysis percentage below 5%, it is considered a non-hemolytic material. Therefore, it can be concluded that acellularized uterine from all 4 protocols could be considered highly hemocompatible.

Table 2: Hemolysis of blood by acellularized uterine patches prepared from 4 protocols (P1, P2, P3, P4)

Sample	Optical density at 545 nm	Hemolysis (%)
Water (control+)	1.31	100
Saline (control-)	0.055	0
P1	0.06	0.39
P2	0.07	1.19
P3	0.058	0.23
P4	0.055	0

Mechanical characterization of scaffolds

A mechanical evaluation test was conducted to ensure that the acellular process did not affect the structural integrity of scaffolds. The extracted results from the stress-strain curves (Fig.4A) are shown in Figure 4B-D.

The native uterus has the maximum tensile stress of 0.66 ± 0.1 MPa and Young's modulus of 1.7 ± 0.2 MPa and they are higher than acellularized samples (P1, P2, P3, and P4), but these differences are not significant (P=0.2). Also, elongation at break was only significantly different for P3-treated uterine tissue which led to a decreased tissue extensibility (P=0.04).

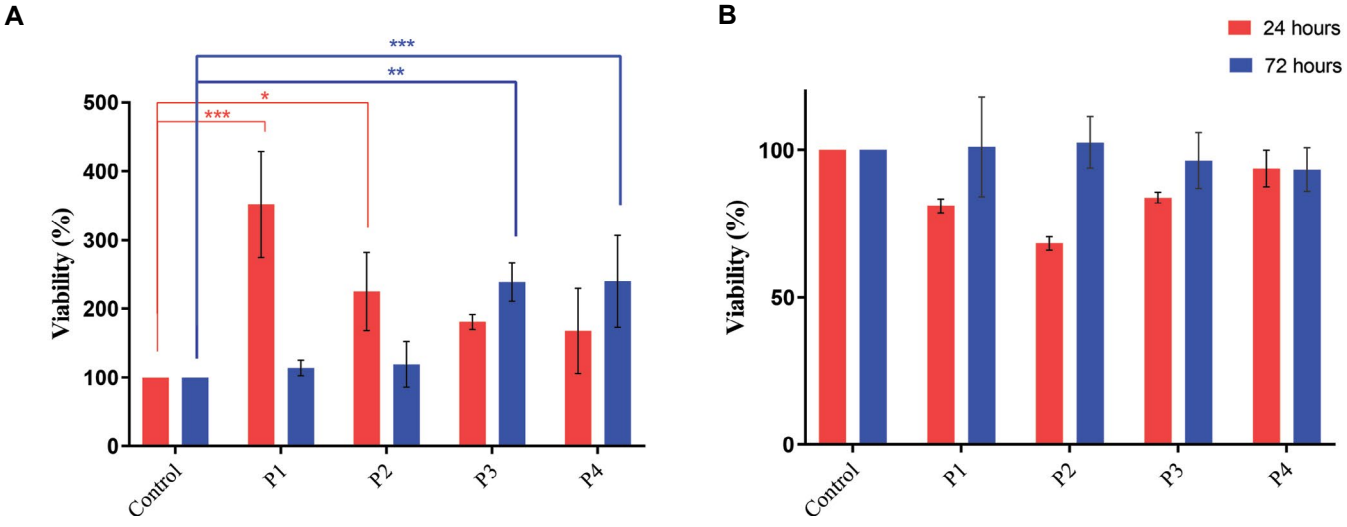

Fig.3: Analysis of cell viability following culture on acellularized uterine scaffolds. **A.** The MTT photograph in direct contact revealed that there were higher cell viabilities in the acellularized samples (P1- P4) compared with control groups. **B.** In indirect contact there were no significant differences between the acellularized groups (P1- P4) and control group after 24 and 72 hours. *; P=0.002, **; P=0.0002, and ***; P=0.0003.

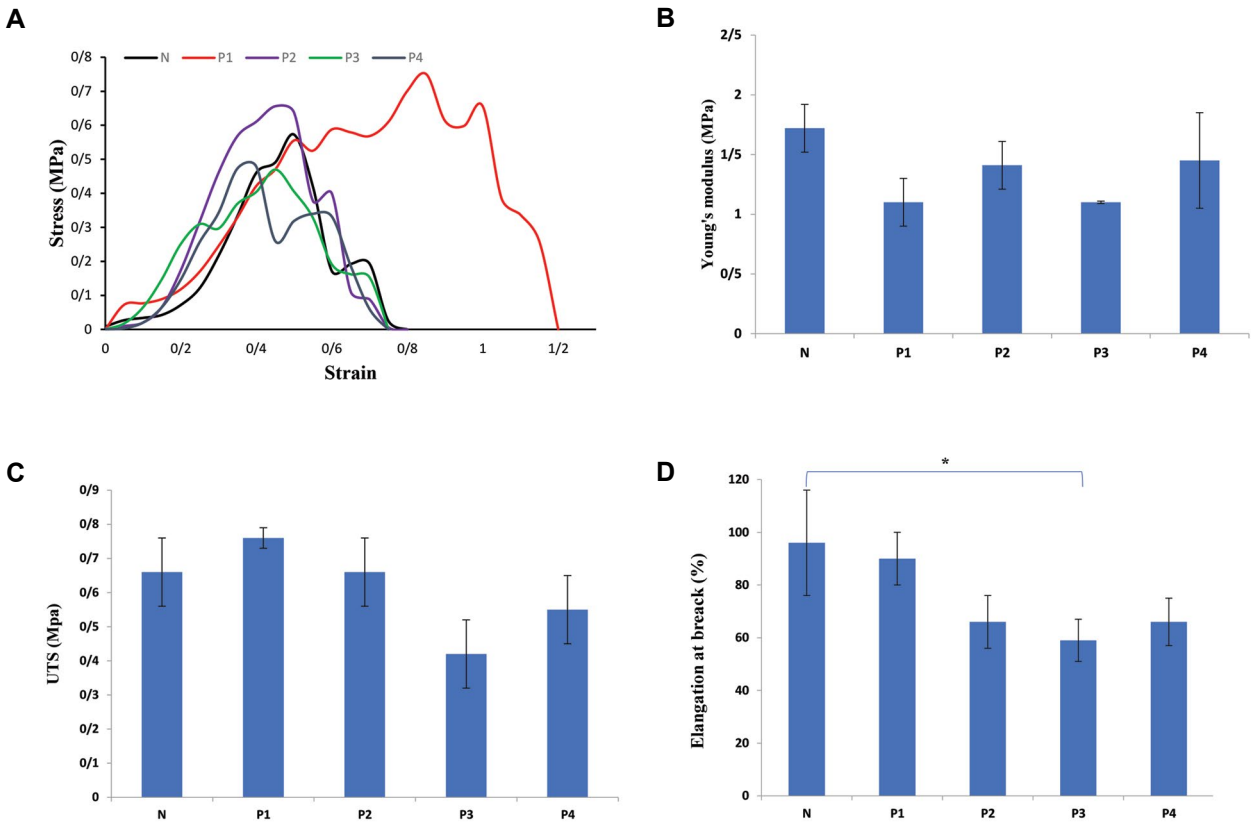

Fig.4: Mechanical evaluation of the samples (n=3); native (N) and acellularized tissues prepared from protocols 1-4 (P1, P2, P3, and P4). **A.** Stress-strain curves, **B.** Young's modulus, and **C.** ultimate tensile strength of acellularized specimens are not significantly different from each other, or the native group. 1 MPa (Mega Pascal)=1 N/mm^2. **D.** Elongation at break in P3 was significantly different compared to native (*; P=0.04).

Discussion

Tissue engineering has proposed various biomaterials for repairing different tissues. Each of these biomaterials has advantages and disadvantages. Among these biomaterials, decellularized ECM-based constructs are more successful due to their high similarity to natural tissues (biocompatibility, mechanical properties, etc.). Moreover, as they have properties such as low antigenic properties and lack stimulation of immune responses in tissue regeneration, can demonstrate additional useful applications (27).

Since the use of natural decellularized scaffolds is currently a promising potential for regenerating, replacing, or improving the function of various organs such as the vagina, heart, and bladder, researchers are working to achieve an optimal protocol of tissue engineering for uterine tissue repair and treatment of AUFI patients. Previous studies compared the efficacy of different protocols such as perfusion of detergents and ionic solutions or high hydrostatic pressure for decellularization of the different animal uterine tissues (15, 16, 28). Optimizing the cell removal protocol is very important because tissue standardization will enable the optimization of clinical protocols, which will result in better outcomes for patients. To achieve the protocol that while is simple, has similar characteristics to the natural tissue, we selected four different types of decellularization methods and evaluated the efficiency of cell removal and the preservation of the physicochemical properties as well as the biological integrity of rat uterine tissues. In protocol 1, we used SDS 1% for 2 hours, and DNase to remove the cells and nuclei. In protocol 2, the soaking time of scaffolds in the SDS was increased to 4 hours. In protocol 3, we used three additional doses of SDS (0.01, 0.1, and 1%) with a longer time (24 hour) and Triton X100. In protocol 4, in addition to cardiac perfusion and removal of blood cells, we performed a freeze-thawing process before using the detergent (SDS and Triton x100). Because the success of the decellularization method is based on the cell removal while maintaining ECM, we evaluated these two properties.

Histological examination showed that protocol 1 still had some cell residue and even the amount of DNA was 24% compared to the native sample. In protocol 2, with increasing detergent time from 2 to 4 hours and washing duration (from 7 to 10 days), the number of complete cell debris (nucleus and cytoplasm) decreased, and the amount of DNA decreased considerably, but their cell cytoplasm remained. The importance of complete removal of cellular residue from scaffolds is related to the presence of major histocompatibility complexes (MHC) present on the cell membrane, which can lead to immune responses and hyperacute rejection of scaffolds (29). These nucleus-free cytoplasms also seemed to be removed if the washing period was longer. The DNA count of scaffolds obtained from protocol 3 was the lowest but the cytoplasm remained to some extent. Interestingly, although DNase enzyme (DNA digester) was used only in the first two protocols, the scaffolds obtained from protocol P3 had the lowest amount of DNA, which shows that the using of detergents (SDS and Triton X-100) is enough to remove DNA. Our study showed that protocol 4 was the most efficient method of cellular removal (without any debris).

The second purpose of effective decellularization is preserving biologically active ECM components. Successful repair after implantation of acellular tissue depends on the preservation of the 3D ECM structure or its protein composition. In the regeneration process, ECM has an essential role in cell adhesion, aggregation, migration, as well as proliferation and differentiation of cells for that specific tissue. This is done by preserving vascular cells and molecules such as growth factors, collagen, elastin, glycosaminoglycans, fibronectin, and, laminin (30). Since collagen is one of the main components of ECM proteins that plays an important role in providing the tissue framework connection, and tensile strength and, affecting cell types disposition, the destruction or reduction of this protein is the cause of scaffold failure (31). Histology and FESEM analysis of protocols 1,2 , and 4 showed that ECM proteins preserved their structural integrity during decellularization, but similar to Santoso et al. (16) study, long exposure time with SDS, had a disruptive effect on the ECM during the process of decellularization and reduced the collagen bundles in P3. Another important role of the acellular ECM in the repair process is mechanical support for tissue regeneration and fabrication and even strategies such as the use of cross-linkers were used to optimize the mechanical properties and structural stability of the tissue (32). Scaffold stiffness plays an important role in the migration and proliferation of stem cells and modulation of the ECM microenvironment after recellularization. Tiemann et al. (33) suggested that the sheep uteri tissues became stronger after decellularisation treatments with SDS, SDC, or triton x100. They explained that this is the result of the denser structure of the ECM caused by cell removal.

In our study, although uterine tissue appeared to be visually thinner and weaker after the acellularization, there were no statistically significant differences between these acellularized samples from all of the protocol and native groups in young modulus elasticity and UTS. However, the elongation at break of the samples obtained from the p 3 protocol is significantly lower compared to the normal sample. Reduction and destruction of collagen (in histological examination) and contraction of ECM fibers (in FESEM photos) justify this extension reduction.

Since increased detergent concentrations in the scaffold in addition to ECM disruption, can increase adverse cell outcomes (23), we assessed the removal of the detergent agents and toxicity of the scaffolds by MTT assay (via direct and indirect contacts of MSCs to acellularized scaffolds) and hemolysis assay. The results of the MTT assay showed that 24 h after incubation, the acellular scaffolds from all protocols did not inhibit the growth of the co-cultured cells but rather promoted cell proliferation

significantly. The three-dimensional environment of the scaffolds (compared to the two-dimensional environment of the control group), can be a justification for this finding. Yu et al. (34). showed that growth factors such as epidermal growth factor (EGF), transforming growth factor-beta (TGF-β) and basic fibroblast growth factor (bFGF) were preserved after pancreatic body tail acellularization and these cytokines can stimulate proliferation of cells in MTT assay. A previous study showed that SDS 1% altered the basement membrane complex (BMC) of the porcine urinary bladder. BMC has an important function in the attachment and growth of cells (35). In our study, Scaffolds obtained from protocols 1 and 2 were treated with SDS for a shorter time (than the other two protocols). Therefore, the possibility of more cell proliferation in the first 24 hours can be attributed to the more intact structure of ECM and better cell attachment in these two groups. Increased proliferation in 24 hours, caused a lack of nutrients, growth factors, and insufficient space, followed by cell death in 72 hours.

Also, in the indirect MTT test, where the cells were not implanted in the three-dimensional structure of the scaffolds, cell proliferation was not significantly different from the control sample. These results of the MTT assay suggested that the acellular uterine scaffolds exhibited good compatibility without any cytotoxic effect on co-cultured cells. Another test for the assessment of the cytotoxicity of ECM is the hemolysis assay. If toxic chemical agents are not removed from the scaffold during acellularization, it will cause RBC damage and hemoglobin release (36). So, a low degree of hemolysis indicates better hemocompatibility of the biomaterial. In our study, uterine patches from all protocols were hemocompatible. SDS is the strong ionic detergent and preferred agent for removing cell debris from different tissue. However, in addition to the damage to phospholipid membranes (37) and denaturation of proteins (38), SDS can lead to cell toxicity (39).

Momtahan et al. (36) removed SDS using DW, Phosphate-buffered saline, and Triton X-100 from decellularized heart tissues. They showed that using Triton-X 100 can double the SDS removal rate from ECM (36). Nouri et al. (40) used three methods for the decellularization of mouse uterine. 1: SDS and triton X-100 solutions (at concentrations of 0.1, 0.3, 0.6%, each for 24 hours), 2: hypertonic and hypotonic solutions, and 3: freeze and thaw and subsequently in 0.5% SDS and Triton X-100 0.1% (each for 48 hours). Their data indicated SDS and Triton X-100 (unlike the other two methods) could completely decellularize the uterus. 3D ultrastructure of decellularized scaffold prepared by this protocol remained intact and the MTT assay revealed that these uterus scaffolds were non-toxic for cell growth and proliferation of menstrual blood stem cells.

In summary, according to the results of our study, P1 and 2 due to incomplete cell removal and P3 due to ECM damage do not have the necessary criteria to be introduced as an optimized method of acellularization of uterine tissue. Therefore, we suggest that the P4 process is an optimal protocol for the acellularization of rat uterus (out of 4 protocols introduced) with complete removal of cell debris, preservation of the protein fibers of ECM, removal of cytotoxic detergents, and finally, preservation of mechanical characteristics.

Conclusion

We aimed to evaluate and ultimately propose an efficient decellularization protocol for uterine tissue, but this study is required more evaluations of recellularization and biocompatibility of the scaffold. Also, not reporting the level of proteins (such as elastin, and fibronectin) and not evaluating the vascular network were the limitations of this study. Evaluation tests should also be performed after implantation *in vivo* studies.

Acknowledgments

This study was a part of the Ph.D. dissertation supported by the Tehran University of Medical Sciences (Grant No: 98-01-30-41244) and performed by the contribution of Tehran University of Medical Sciences and Shahroud University of Medical Sciences. The authors would like to acknowledge the Iran National Science Foundation (INSF, Grant No: 98001385) and the Council for Development of Stem cell Sciences and Technologies (Grant No: 11/35723). There is no conflict of interest in this study.

Authors' Contributions

M.M.K.; Conceptualization, data curation, formal analysis, validation, experimental work, and writing-original draft. M.S.; Conceptualization, review,editing, formal analysis, and validation. F.N., S.R.; Conceptualization, formal analysis, review and editing. S.R., M.S.; Data curation, validation, and project administration. All authors read and approved the final manuscript.

References

1. Johannesson L, Dahm-Kähler P, Eklind S, Brännström M. The future of human uterus transplantation. Women's Health (Lond). 2014; 10(4): 455-467.
2. Jones BP, Saso S, Yazbek J, Thum MY, Quiroga I, Ghaem-Maghami S, et al. Uterine transplantation: scientific impact paper No. 65 April 2021. BJOG. 2021; 128(10): e51-e66.
3. Kuo CY, Baker H, Fries MH, Yoo JJ, Kim PCW, Fisher JP. Bioengineering strategies to treat female infertility. Tissue Eng Part B Rev. 2017; 23(3): 294-306.
4. Magalhaes RS, Williams JK, Yoo KW, Yoo JJ, Atala A. A tissue-engineered uterus supports live births in rabbits. Nat Biotechnol. 2020; 38(11): 1280-1287.
5. Schutte SC, Taylor RN. A tissue-engineered human endometrial stroma that responds to cues for secretory differentiation, decidualization, and menstruation. Fertil Steril. 2012; 97(4): 997-1003.
6. House M, Sanchez CC, Rice WL, Socrate S, Kaplan DL. Cervical tissue engineering using silk scaffolds and human cervical cells. Tissue Eng Part A. 2010; 16(6): 2101-2112.
7. Campbell GR, Turnbull G, Xiang L, Haines M, Armstrong S, Rolfe BE, et al. The peritoneal cavity as a bioreactor for tissue engineering visceral organs: bladder, uterus, and vas deferens. J Tissue Eng Regen Med. 2008; 2(1): 50-60.

8. Porzionato A, Stocco E, Barbon S, Grandi F, Macchi V, De Caro R. Tissue-engineered grafts from human decellularized extracellular matrices: a systematic review and future perspectives. Int J Mol Sci. 2018; 19(12): 4117.
9. Ciampi O, Bonandrini B, Derosas M, Conti S, Rizzo P, Benedetti V, et al. Engineering the vasculature of decellularized rat kidney scaffolds using human induced pluripotent stem cell-derived endothelial cells. Sci Rep. 2019; 9(1): 8001.
10. Ott HC, Matthiesen TS, Goh SK, Black LD, Kren SM, Netoff TI, et al. Perfusion-decellularized matrix: using nature's platform to engineer a bioartificial heart. Nat Med. 2008; 14(2): 213-221.
11. Negishi J, Funamoto S, Kimura T, Nam K, Higami T, Kishida A. Porcine radial artery decellularization by high hydrostatic pressure. J Tissue Eng Regen Med. 2015; 9(11): E144-E151.
12. Hashimoto Y, Funamoto S, Kimura T, Nam K, Fujisato T, Kishida A. The effect of decellularized bone/bone marrow produced by high-hydrostatic pressurization on the osteogenic differentiation of mesenchymal stem cells. Biomaterials. 2011; 32(29): 7060-7067.
13. Cebotari S, Tudorache I, Ciubotaru A, Boethig D, Sarikouch S, Goerler A, et al. Use of fresh decellularized allografts for pulmonary valve replacement may reduce the reoperation rate in children and young adults: early report. Circulation. 2011;124 (11 Suppl): S115-S123.
14. Badylak SF. Decellularized allogeneic and xenogeneic tissue as a bioscaffold for regenerative medicine: factors that influence the host response. Ann Biomed Eng. 2014; 42(7): 1517-1527.
15. Daryabari SS, Kajbafzadeh AM, Fendereski K, Ghorbani F, Dehnavi M, Rostami M, et al. Development of an efficient perfusion-based protocol for whole-organ decellularization of the ovine uterus as a human-sized model and in vivo application of the bioscaffolds. J Assist Reprod Genet. 2019; 36(6): 1211-1223.
16. Santoso EG, Yoshida K, Hirota Y, Aizawa M, Yoshino O, Kishida A, et al. Application of detergents or high hydrostatic pressure as decellularization processes in uterine tissues and their subsequent effects on in vivo uterine regeneration in murine models. PLoS One. 2014; 9(7): e103201.
17. Keane TJ, Swinehart IT, Badylak SF. Methods of tissue decellularization used for the preparation of biologic scaffolds and in vivo relevance. Methods. 2015; 84: 25-34.
18. Gilbert TW, Sellaro TL, Badylak SF. Decellularization of tissues and organs. Biomaterials. 2006; 27(19): 3675-3683.
19. Song M, Liu Y, Hui L. Preparation and characterization of acellular adipose tissue matrix using a combination of physical and chemical treatments. Mol Med Rep. 2018; 17(1): 138-146.
20. White LJ, Taylor AJ, Faulk DM, Keane TJ, Saldin LT, Reing JE, et al. The impact of detergents on the tissue decellularization process: a ToF-SIMS study. Acta Biomater. 2017; 50: 207-219.
21. Wolcott NS, Sit KK, Raimondi G, Hodges T, Shansky RM, Galea LAM, et al. Automated classification of estrous stage in rodents using deep learning. Sci Rep. 2022; 12: 17685.
22. Helmer KS, Cui Y, Chang L, Dewan A, Mercer DW. Effects of ketamine/xylazine on expression of tumor necrosis factor-alpha, inducible nitric oxide synthase, and cyclo-oxygenase-2 in rat gastric mucosa during endotoxemia. Shock. 2003; 20(1): 63-69.
23. Ichimura T, Kasai M, Imai K, Yamauchi M, Fukuda T, Yasui T, et al. A difficult to diagnose case of low-grade endometrial stromal sarcoma with smooth muscle differentiation treated with laparoscopic surgery: a case report. Mol Clin Oncol. 2022; 16(4): 92.
24. Ozawa A, Sakaue M. New decolorization method produces more information from tissue sections stained with hematoxylin and eosin stain and masson-trichrome stain. Ann Anat. 2020; 227: 151431.
25. Mehdizadeh Kashi A, Tahemanesh K, Chaichian Sh, Joghataei MT, Moradi F, Tavangar SM, et al. How to prepare biological samples and live tissues for scanning electron microscopy (SEM). Galen Medical Journal. 2014; 3(2): 63-80.
26. Autian J. Biological model systems for the testing of the toxicity of biomaterials. In: Kronenthal RL, Oser Z, Martin E, editors. Polymer science and technology. Boston: Springer; 1975; 181-203.
27. Abdulghani S, Mitchell GR. Biomaterials for in situ tissue regeneration: a review. Biomolecules. 2019; 9(11): 750.
28. Campo H, Baptista PM, López-Pérez N, Faus A, Cervelló I, Simón C. De-and recellularization of the pig uterus: a bioengineering pilot study. Biol Reprod. 2017; 96(1): 34-45.
29. Gilpin A, Yang Y. Decellularization strategies for regenerative medicine: from processing techniques to applications. Biomed Res Int. 2017; 2017: 9831534.
30. Hellstrom M, Bandstein S, Brannstrom M. Uterine tissue engineering and the future of uterus transplantation. Ann Biomed Eng. 2017; 45(7): 1718-1730.
31. Zhang X, Chen X, Hong H, Hu R, Liu J, Liu C. Decellularized extracellular matrix scaffolds: recent trends and emerging strategies in tissue engineering. Bioact Mater. 2021; 10: 15-31.
32. Yao Q, Zheng YW, Lin HL, Lan QH, Huang ZW, Wang LF, et al. Exploiting crosslinked decellularized matrix to achieve uterus regeneration and construction. Artif Cells Nanomed Biotechnol. 2020; 48(1): 218-229.
33. Tiemann TT, Padma AM, Sehic E, Bäckdahl H, Oltean M, Song MJ, et al. Towards uterus tissue engineering: a comparative study of sheep uterus decellularisation. Mol Hum Reprod. 2020; 26(3): 167-178.
34. Yu H, Chen Y, Kong H, He Q, Sun H, Bhugul PA, et al. The rat pancreatic body tail as a source of a novel extracellular matrix scaffold for endocrine pancreas bioengineering. J Biol Eng. 2018; 12: 6.
35. Faulk DM, Carruthers CA, Warner HJ, Kramer CR, Reing JE, Zhang L, et al. The effect of detergents on the basement membrane complex of a biologic scaffold material. Acta Biomater. 2014; 10(1): 183-193.
36. Momtahan N, Panahi T, Poornejad N, Stewart MG, Vance BR, Struk JA, et al. Using hemolysis as a novel method for assessment of cytotoxicity and blood compatibility of decellularized heart tissues. ASAIO J. 2016; 62(3): 340-348.
37. de la Maza A, Parra JL. Vesicle-micelle structural transitions of phospholipid bilayers and sodium dodecyl sulfate. Langmuir. 1995; 11(7): 2435-2441.
38. Hwang J, San BH, Turner NJ, White LJ, Faulk DM, Badylak SF, et al. Molecular assessment of collagen denaturation in decellularized tissues using a collagen hybridizing peptide. Acta Biomater. 2017; 53: 268-278.
39. Andersen KK, Oliveira CL, Larsen KL, Poulsen FM, Callisen TH, Westh P, et al. The role of decorated SDS micelles in sub-CMC protein denaturation and association. J Mol Biol. 2009; 391(1): 207-226.
40. Nouri A, Hajian M, Monsefi M. Tissue engineering of mouse uterus using menstrual blood stem cells (MenSCs) and decellularized uterine scaffold. Stem Cell Res Ther. 2021; 12(1): 475.

Cell J
Cell Journal(Yakhteh) Homepage: https://www.celljournal.org/
Original Article Vol 25, No 1, January 2023, Pages: 35-44

Effects of Different Perfusing Routes through The Portal Vein, Hepatic Vein, and Biliary Duct on Whole Rat Liver Decellularization

Bahram Jambar Nooshin, M.Sc.[1], Tahereh Tayebi, Ph.D.[1], Amirhesam Babajani, M.D.[2], Mohammad-Mehdi Khani, Ph.D.[1*], Hassan Niknejad, Ph.D.[2*]

1. Department of Tissue Engineering and Applied Cell Sciences, School of Advanced Technologies in Medicine, Shahid Beheshti University of Medical Sciences, Tehran, Iran
2. Department of Pharmacology, School of Medicine, Shahid Beheshti University of Medical Sciences, Tehran, Iran

**Corresponding Addresses: P.O.Box: 1985717446, Department of Tissue Engineering and Applied Cell Sciences, School of Advanced Technologies in Medicine, Shahid Beheshti University of Medical Sciences, Tehran, Iran*
P.O.Box: 1985717446, Department of Pharmacology, School of Medicine, Shahid Beheshti University of Medical Sciences, Tehran, Iran
Emails: khani@sbmu.ac.ir, niknejad@sbmu.ac.ir

Received: 11/July/2022, Revised: 11/September/2022, Accepted: 04/October/2022

Abstract

Objective: Organ transplantation is the last therapeutic choice for end-stage liver failure, which is limited by the lack of sufficient donors. Decellularized liver can be used as a suitable matrix for liver tissue engineering with clinical application potential. Optimizing the decellularization procedure would obtain a biological matrix with completely removed cellular components and preserved 3-dimensional structure. This study aimed to evaluate the decellularization efficacy through three anatomical routes.

Materials and Methods: In this experimental study, rat liver decellularization was performed through biliary duct (BD), portal vein (PV), and hepatic vein (HV); using chemical detergents and enzymes. The decellularization efficacy was evaluated by measurement of DNA content, extracellular matrix (ECM) total proteins, and glycosaminoglycans (GAGs). ECM preservation was examined by histological and immunohistochemical (IHC) staining and scanning electron microscopy (SEM). Scaffold biocompatibility was tested by the MTT assay for HepG2 and HUVEC cell lines.

Results: Decellularization through HV and PV resulted in a transparent scaffold by complete cell removal, while the BD route produced an opaque scaffold with incomplete decellularization. H&E staining confirmed these results. Maximum DNA loss was obtained using 1% and 0.5% sodium dodecyl sulfate (SDS) in the PV and HV groups and the DNA content decreased faster in the HV group. At the final stages, the proteins excreted in the HV and PV groups were significantly less than the BD group. The GAGs level was diminished after decellularization, especially in the PV and HV groups. In the HV and PV groups the collagen amount was significantly more than the BD group. The IHC and SEM images showed that the ECM structure was preserved and cellular components were entirely removed. MTT assay showed the biocompatibility of the decellularized scaffold.

Conclusion: The results revealed that the HV is a more suitable route for liver decellularization than the PV and BD.

Keywords: Biliary Duct, Decellularization, Hepatic Vein, Portal Vein, Tissue Engineering

Citation: **Jambar Nooshin B, Tayebi T, Babajani A, Khani MM, Niknejad H. Effects of different perfusing routes through the portal vein, hepatic vein, and biliary duct on whole rat liver decellularization. Cell J. 2023; 25(1): 35-44. doi: 10.22074/CELLJ.2022.557600.1081.**

Introduction

Chronic and acute liver diseases are growing challenges responsible for approximately 2% of total deaths worldwide (1). Liver transplantation is the last treatment option in end-stage liver disease; however, shortage of transplantable tissues is the major obstacle for this therapeutic approach (2). In order to surmount this challenge, engineering liver tissue by employing decellularization-recellularization techniques has become a valuable strategy in recent years (3). The decellularization technique aims to provide a healthy cell-free tissue with preserved extracellular matrix (ECM) composition, intact 3D macro- and micro-structure, and a maintained vascular network. Subsequently, the decellularized scaffold could be engineered by recellularization. These cells then attach onto the scaffold, proliferate, differentiate, become functional, and create a new engineered tissue for tissue transplantation (4).

ECM consists of functional and structural molecules, which play a pivotal role in the viability, proliferation, and differentiation of transferred cells after re-cellularization (5). Thus, preserving the bio-architecture of the ECM with the maximum bioactive molecules is a pivotal aspect of tissue engineering. Different decellularization strategies have been designed utilizing single or multi-step mechanical, chemical, and enzymatic protocols, leading to various undesirable structural and compositional effects on decellularized ECM (6). Optimizing decellularization methods has become an interesting issue for researchers in order to reduce the destructive impact of the current techniques by selecting suitable material and conditions regarding cellular density, specific ECM structure, physiological function, and anatomy of aimed tissue (7). The optimized decellularization method is a rapid and effective procedure for cell destruction and removal of the cell membrane, cytoplasmic organelles, and nuclear

content debris from the tissue in the shortest time. Simultaneously, maintaining the structural components of tissue scaffold such as various collagen types, laminin, fibronectin, and glycosaminoglycans (GAGs) and preventing washing of growth factors, cytokines, and other signaling molecules out of the ECM are essential parameters in an optimized decellularization protocol (8). The controversial challenge of decellularization protocols is balancing between cellular debris removal that reduces the immunogenicity problems of the ECM and preserving the crucial components of the scaffold that is pivotal for cellular function after re-cellularization (9, 10). Therefore, designing a non-immunogenic, non-toxic, and non-pathogenic scaffold depends on utilizing effective decellularization strategies. The primary cause of decellularized scaffold immunogenicity is the remaining cellular DNA, RNA, and membrane antigenic epitopes, as well as decellularizing agents such as detergents in the ECM (11). Thus, removing antigens from decellularized scaffold as much as possible will reduce the chance of immune reaction.

In order to increase the decellularization efficacy and reduce immunogenicity, selecting an appropriate access route for infusing decellularization agents is pivotal. The common way to whole organ decellularization is the use of the main blood supply vein and artery of the organ to achieve the optimum decellularized scaffold, but the blood circulation system of the liver is quite specific and unique to this organ. Unlike other organs, the liver possesses four major routes including three main blood vessels [the portal vein (PV) and hepatic artery (HA) as blood entry routes, and the hepatic vein (HV) as the only blood outlet], and bile duct (BD) network which originates from the depths of the liver tissue. The vascular network in the structural units of the liver (sinusoids) contains three branches of vessels and a biliary duct (BD) as part of the biliary system (12). The rapid penetration rate of decellularization agents in each part of the liver, which is critical for decellularization efficacy, depends on the administration route. The present study aims to demonstrate the success rate of whole rat liver decellularization by administration of decellularizing agents through different routes, including PV, HV and BD in similar conditions.

Material and Methods

Rat liver isolation

In this experimental study, adult male Sprague-Dawley rats (200-300 g) were used to provide the intact liver. The animals were kept under standard controlled environment conditions (12:12 hours. light/dark cycle) with free access to food and water. The rats were anesthetized by intraperitoneal injection (IP, 0.1 ml/kg) of ketamine/xylazine cocktail based on the guideline of the Institutional Animal Care and Use Committees (IACUC). After skin disinfection, animals were placed in an abdominal surgery position, and a U-shaped incision was performed to expose the abdominopelvic cavity. BD (26 G), PV (24 G), and HV (22 G) were cannulated by an intravenous catheter (Tabanmedic, IR). Besides, the hepatic artery and superior vena cava were ligated by a 4-0 silk suture. Subsequently, 0.5 ml of 200 IU/ml aqueous heparin (Daru Pakhsh, IR) solution was injected into the PV to prevent blood coagulation. Finally, the liver was removed from the abdominopelvic cavity and rinsed by 50 ml of sterile heparinized phosphate-buffered saline (PBS, 10 IU/ml) by a 0.5 ml/minute perfused flow rate and stored in PBS at 2-8˚C for starting the decellularization process.

Rat liver decellularization

According to previous studies, a chemical method consisting of a combination of detergent and enzymes was used for whole organ decellularization (13). The harvested liver was transferred to the main chamber of a home-designed decellularization bioreactor under the biological class B safety cabinet (Fig.1A). The bioreactor consists of four major parts: i. The main chamber: It is a chamber in which the liver is placed for decellularization. It has three inlet and outlet channels to connect to the routes of the liver. During the perfusion of decellularization solutions, one of the routes was selected for entry of the fluid and was connected to the perfusion inlet fluid valve and two other routes were used as fluid outlets. ii. Perfusion pumps: peristaltic pumps are designed to supply the required flow rate for decellularization solutions in the path of the inlet and outlet routes from 0.5 to 1.5 mL/minute in different steps. iii. Media reservation bottles: the chambers or bottles are installed for storage and perfusion of the solutions to the inlet route i and collection of the outlets' effluents. iv. Tubes, connectors and valves: different types and sizes of tubes, connectors and valves are designed to guide solutions into the liver at specific times and collect the effluents. Rat liver decellularization was done through one of the three different perfusion routes: BD, PV, and (HV) (Fig.1B); using a method consists of chemical detergents and enzymes.

The decellularization process was initiated by infusing Krebs-Henseleit buffer (PH=7.4) consisting of NaCl 118 mM (Merck, Germany), $NaHCO_3$ 25 mM (Merck, Germany), KCl 4.7 mM (Merck, Germany), KH_2PO_4 1.2 mM (Merck, Germany), $MgSO_4$ 1.2 mM (Merck, Germany), $CaCl_2$ 1.25 mM (Merck, Germany) and Glucose 11 mM (Merck, Germany) perfused at a 0.5 mL/minute flow rate for removing the remaining blood in the liver (14). Decellularization was continued by administrating different aqueous materials including Sodium dodecyl sulfate (SDS, Merck, Germany), Triton X100 (Merck, Germany), and sodium deoxycholate (SDC, Sigma-Aldrich, USA) with different concentrations, durations, and flow rates which are shown in Figure 1C.

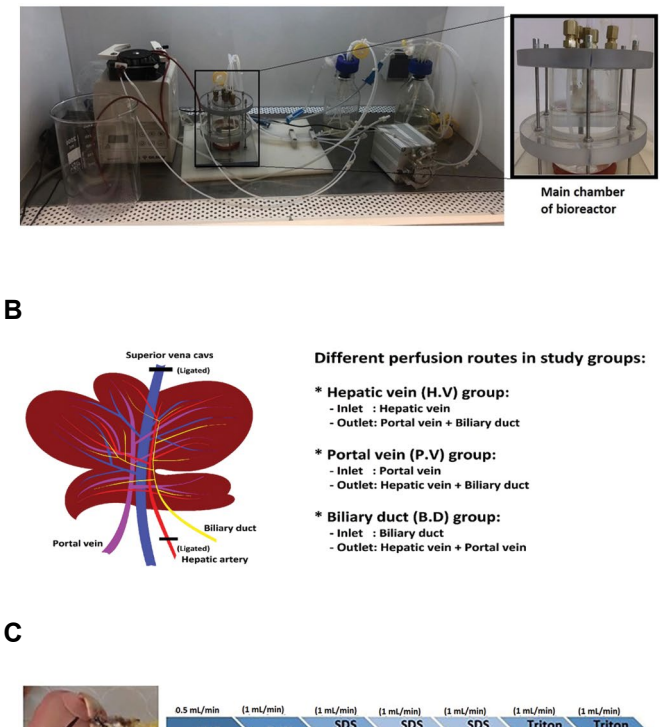

Fig.1: The bioreactor, perfusing routes and process of liver decellularization. **A.** Custom-designed whole rat liver decellularization bioreactor and its main chamber. The cannulated routes (HV, PV, and BD) of rat liver were connected to the main chamber valves letting the decellularization solutions to circulate in the liver by peristaltic perfusion pump. **B.** Schematic anatomical structure of the rat liver vascular network. **C.** Diagram of rat liver decellularization protocol illustrated by detailed information of each step, including ingredient, flow rate, and duration. The rat liver before and after the decellularization process is shown in the start and endpoint of the diagram. HV; Hepatic vein, PV; Portal vein, and BD; Biliary duct.

DNA content measurement

Measurement of total remaining DNA in the decellularized tissues was conducted for freeze-dried decellularized livers as well as the decellularization effluent during perfusion in all study groups, using the DNeasy Blood & Tissue Kit (QIAGEN, Germany). Briefly, total DNA was extracted from 1mL of effluent samples and 15mg of dried tissue according to the kit's instructions. DNA concentration was measured using a Nanodrop spectrophotometer (ND2000, Thermo, USA) at 260 nm. The data of DNA content was normalized to 1mL of effluent volume or 1mg of dried tissue weight. Equal volumes of the extracted DNA of the decellularized scaffold were loaded onto 1% (w/v) agarose gel and electrophoresed with a 100 bp DNA ladder (Invitrogen-15628019, USA) to investigate DNA fragments.

Histological evaluation of extracellular matrix structure

Freshly isolated and decellularized liver scaffolds were fixed by 10% formalin solution for 24-48 hours. After dehydration by a series of ascending ethanol concentrations (60-100% v/v) and immersion in Xylene (Merck, Germany), tissues were embedded in paraffin. The samples were cut into 5 µm thickness slides with a microtome (MICRO DS, 4055) and stained with standard Hematoxylin-Eosin (H&E). The sample slides were also stained with 300nM DAPI (4', 6-diamidino-2-phenylindole di-hydrochloride, Sigma-Aldrich, USA) solution to assess the removal of the nuclear components of the scaffold. The sections of decellularized liver samples were also stained by Masson Trichrome and Van Gieson for investigation of the ECM network structure.

Total protein measuring assay

To evaluate the total protein content of the decellularization effluents, we measured the total protein concentration by the Pyrogallol red assay kit (BIOREX diagnostic, UK) based on a colorimetric assay with optical absorbance at 600 nm. After each decellularization step, the effluent was sampled and the total protein content was evaluated after papain digestion, hydrolyzation, and neutralization as were described in the previous section. The total protein amount was normalized to 1 mL of effluent volume.

Extracellular matrix component measuring assay

For a detailed evaluation of ECM composition, the amounts of remaining collagen and GAGs in the decellularized tissue were measured. Intact and decellularized liver tissues were cut into small pieces and lyophilized. Subsequently, samples were weighed and digested with Papain (Sigma-Aldrich, USA, 150 µg/mL) at 60˚C overnight. The contents of the GAGs were evaluated according to Farndale et al. (15) with the colorimetric reaction between DMMB (1,6-dimethylmethylene blue, Sigma-Aldrich, US) and GAGs at 525 nm. Afterward, the collagen contents were quantified indirectly using a colorimetric assay to detect hydroxyproline, as described by Reddy and Enwemeka (16). Briefly, papain digested samples were hydrolyzed with 6 N HCL at 105˚C for 18 hours. The hydrolyzed samples were neutralized by 5 N NaOH and then oxidized with Chloramine-T (Merck, Germany). Finally, the samples were reacted with para-dimethylaminobenzaldehyde (Thermo Fisher, USA). The optical absorbance at 570 nm indicated the amount of hydroxyproline in the samples. Collagen values were calculated assuming 12.5% of collagen is hydroxyproline. The amounts of collagen and GAGs were normalized to 1mg of dried tissue weight.

Scanning electron microscopy

For ultrastructural investigation of the decellularized scaffold of rat liver, samples were fixed in a 2%

glutaraldehyde solution for 24-48 hours at room temperature. The samples were washed three times with fresh PBS. After the dehydration process by a series of ascending ethanol solutions (60-100% v/v), the samples were prepared for scanning electron microscopy (SEM) by a chromium-coated sputter. The ultrastructure of the ECM was visualized using a JEOL 7401F field emission electron microscope.

Immunohistochemical analysis

We performed immunohistochemistry (IHC) staining to determine the critical protein content of the decellularized liver scaffold. After processing the samples using the standard tissue protocol, same as for H&E staining, the samples were permeabilized, and antigen retrieval was done. The primary antibodies including rabbit anti-rat collagen type I (1:500, Millipore-AB755P, Germany), rabbit anti-rat collagen type II (1:250, Millipore-AB2036, Germany), goat anti-rat collagen type IV (1:100, Millipore-AB769, Germany), rabbit anti-rat laminin (1:200, Abcam-AB11575, USA) and rabbit anti-rat fibronectin (1:250, Abcam-AB2413, USA) were used in IHC staining.

Evaluation of cell proliferation on decellularized scaffolds

Cell proliferation on decellularized liver scaffolds was examined using the MTT assay. Both HepG2 (as a hepatocyte model) and HUVEC (as an endothelial cell model) cell lines were used separately in this investigation. The HV, PV, and BD decellularized liver scaffolds were cut into cubic form (5×5×5 mm) and kept overnight in 24-well plates in DMEM. Afterwards, the medium was renewed by DMEM medium containing 10% FBS, 1% penicillin/streptomycin, 100 mM sodium pyruvate, and 1.5 g/L sodium bicarbonate. The cells were suspended at a density of 2×10^6 cells per 50 µL (for each cubic decellularized scaffold), filled in a 0.5 mL insulin syringe, and released drop by drop onto the scaffolds. To allow cell attachment, the seeded scaffolds were placed in an incubator for 1 hour and followed by the addition of cell culture medium with a total volume of 1.2 mL per well on day 0. The same density of cells cultured in the culture plate was used as control. The MTT assay was performed at 1, 2, 3, and 7 days after cell culture by replacing the medium and adding 0.5 mg/ml MTT solution to each well and incubating at 37˚C for four hours. In the final step, all medium was slowly removed and 500 µL dimethyl sulfoxide (DMSO) was added to dissolve the formazan crystals. The absorbance of the well solution was measured at 570 nm using a microplate reader (Mindray plate reader MR-96A).

Statistical analyses

To achieve reproducible results, each independent decellularization group consisted of five samples, and all experiments were repeated at least three times. All statistical analyses were done using the Graph Pad Prism 8 software (GraphPad Software, USA) and were represented as mean ± standard deviation (SD). The results were compared by analyzing with one-way ANOVA and Tukey's tests to determine the significance of differences between groups were $P<0.05$ were considered statistically significant.

Ethics

This study was approved by research Ethics Committees of School Medicine, Shahid Beheshti University of Medical Sciences (IR.SBMU.MSP.REC.1398.756).

Results

Rat liver decellularization

Isolation and decellularization of rat liver were conducted using the decellularization protocol and selecting the infusion routes amongst the hepatic vein, portal vein, and biliary duct. The total decellularization time, including initial, middle and final washing steps, was less than 10 hours.

Macroscopic evaluations demonstrated that the decellularized scaffold was transparent with vascular network appearance in the PV and HV groups. No visible macroscopic difference was detected between these two groups, while the decellularized scaffold of the BD group had an opaque and unclear appearance, which showed incomplete liver decellularization (Fig.2A-C).

The H&E stained slides of intact and decellularized tissue revealed that selecting the HV and PV routes for decellularization led to removing all cellular contents. In addition, the remaining scaffolds had a fibrillary ECM structure. In contrast, in the BD group, cellular debris remained in parts of the scaffold, indicating that the decellularization process was incomplete (Fig.2D-F).

DNA content of extracellular matrix and effluents

Quantitative evaluation of the total DNA content of the decellularized liver scaffold in the three experimental groups demonstrated that total the DNA amounts in the HV, PV, and BD groups were 20.6 ± 5.4, 102.0 ± 11.1, and 602.8 ± 64.7 ng/mg of dry tissue, respectively (Fig.3A). These results exhibited that using the HV route for liver decellularization resulted in the lowest level of residual DNA content in the scaffold compared to the PV and BD routes. In the HV group the remaining DNA content was approximately 20.6 ng/mg of dry liver scaffold that was lower than 50 ng/mg dry weight as an accepted threshold level for approval of a tissue decellularization protocol. The DNA gel electrophoresis pattern is illustrated in Figure 3B. In the HV group, the fragment length of residual DNA was lower than 150 bp. However, a higher amount of DNA with a wide distribution of DNA fragments (approximately less than 200 bp) was seen in the PV group. On the other hand, higher amounts of DNA with longer lengths were observed in the BD group which is similar to the DNA electrophoretic pattern of intact liver. DAPI staining results also confirmed these results (Fig.3C-F).

Quantitative assessment of the effluents' total DNA revealed that the maximum amount of DNA removal occurred after using 1% and 0.5% SDS in the fourth step in the PV (1599 ± 137 µg/mL) and HV (2384 ± 413 µg/mL) groups. Besides, a significant difference ($P<0.001$) between the effluent DNA content of the HV and PV groups was observed in the maximal point at the 195th minute (Fig.3G). After that, the

effluents' DNA content in both groups decreased gradually until the last stage. In contrast, the total amount of DNA did not sharply peak at any decellularization step in the BD group; rather, relatively high amounts of DNA were removed from the liver during all stages continuously. A closer look at the last step DNA content of effluent in the HV and PV groups shows that the DNA content in the HV route reached zero faster than the PV route (Fig.3H).

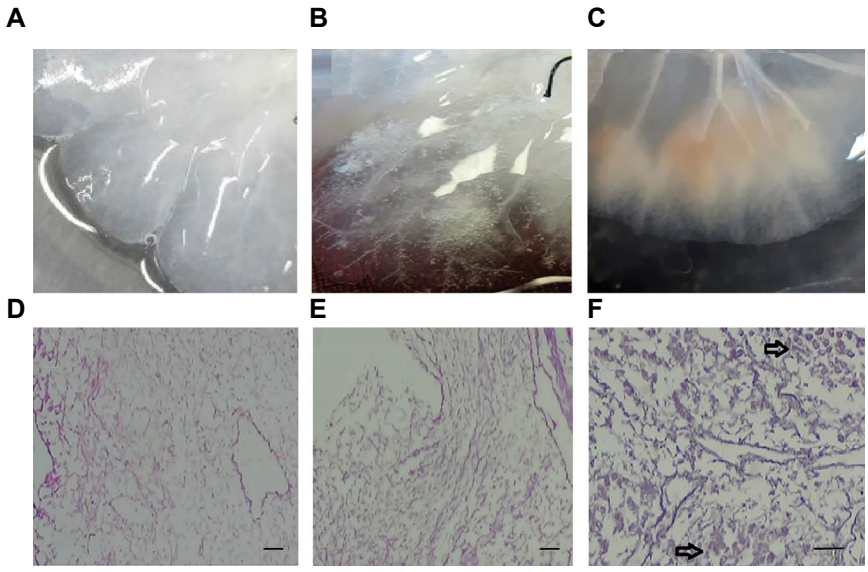

Fig.2: Macroscopic and histological evaluation of decellularizes livers. Macroscopic pictures of **A.** Decellularized liver with HV, **B.** PV and **C.** BD routes show complete decellularization in the HV and PV groups, but incomplete in the BD route group. Microscopic evaluation by H&E staining in all groups showed no cells in **D.** The HV and **E.** PV groups, but in **F.** The BD samples, some parts of the scaffold were not cleared of cells after decellularization which are shown with a black arrow in the picture (scale bar: 100 µm). HV; Hepatic vein, PV; Portal vein, and BD; Biliary duct.

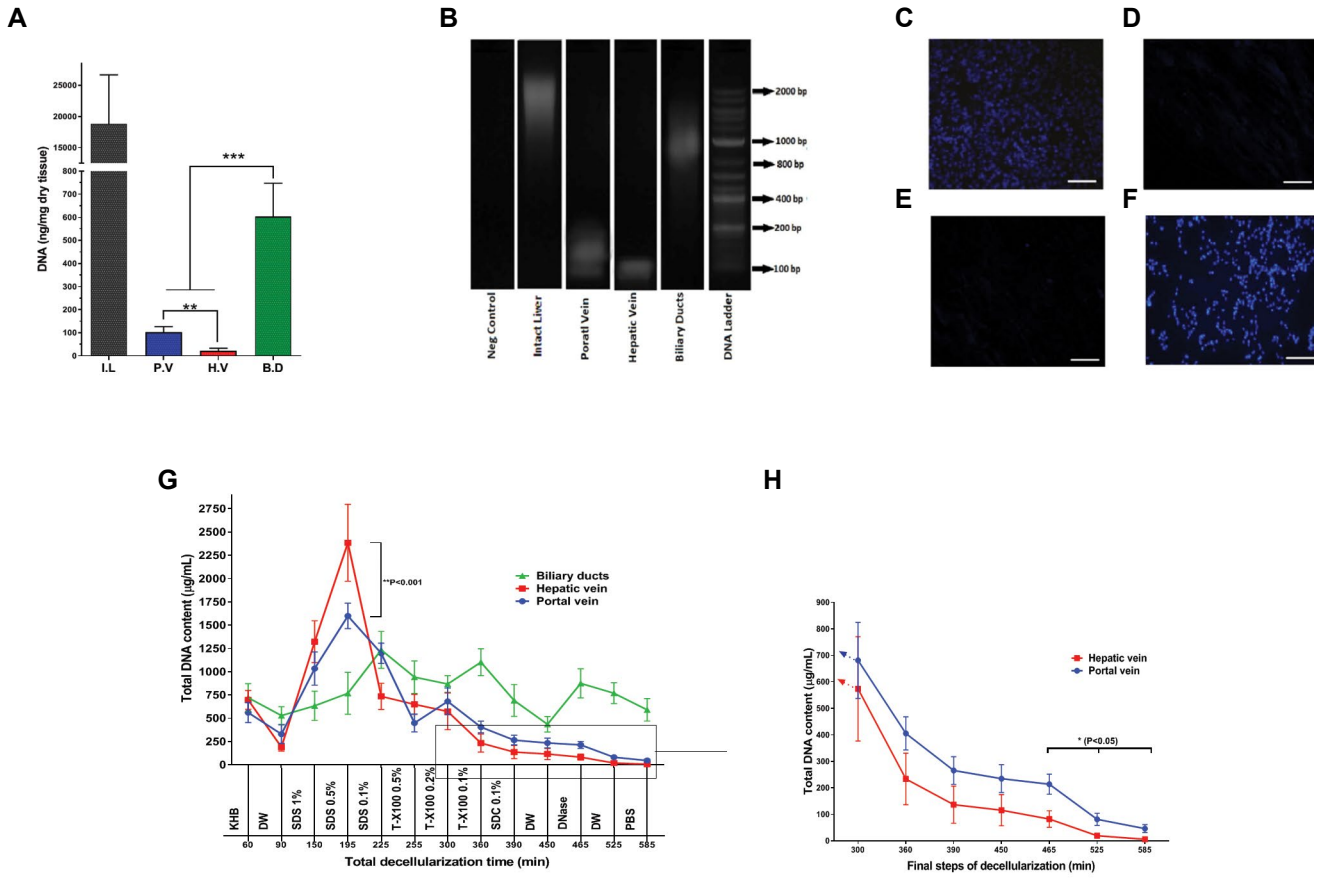

Fig.3: Evaluating the DNA content. **A.** Comparison of the DNA content of decellularized liver through the PV, HV, and BD routes with that of IL. **B.** DNA gel electrophoresis pattern in all experimental groups. **C-F.** DAPI staining in the IL, PV, HV and BD groups, respectively (scale bar: 100 µm). **G.** Effluent of the DNA content of the HV, PV, and BD groups during liver decellularization steps. **H.** Comparison of total DNA content of the decellularization effluent for the HV and PV routes at final steps. All quantitative data were analyzed through one-way ANOVA and by Tukey's tests and represented as mean ± SD (n=5). HV; Hepatic vein, PV; Portal vein, BD; Biliary duct, IL; Intact liver, *; P<0.05, **; P<0.01, and ***; P<0.001.

Total protein and extracellular matrix components of the decellularized scaffold

Data from total protein measurement demonstrated that the patterns of removing protein from the liver in all three experimental groups were relatively similar, even though there were differences among the protein concentrations and excretion times of the groups (Fig.4A). In the BD group, there was a significant delay in protein release. However, in the HV and PV groups, the protein content of the effluents were maximum after SDS solutions and subsequently decreased gradually in the next decellularization steps. The proteins excreted in the HV and PV groups were undetectable and significantly lower than the BD group in the final stages.

The results of specific methods for investigating the remaining extracellular proteins such as collagen and GAGs in decellularized scaffolds demonstrated that liver ECM proteins were affected during decellularization.

As Figure 4B shows, the total GAGs amount in the intact liver was 62.74 ± 7.28 µg/mg of dried tissue, while in the PV, HV, and BD groups, the amounts of GAGs were 25.48 ± 4.35 µg/mg, 28.36 ± 1.90 µg/mg and 43.94 ± 7.68 µg/mg, respectively. These data indicate that the total GAGs levels were diminished when cellular contents were eliminated from the liver. Although there was no difference between the PV and HV groups in GAGs levels, a significant decrease in liver GAGs amounts was seen in both mentioned groups compared with intact liver (P<0.001) and BD groups (P<0.05). Besides, the total collagen level in the intact liver (79.96 ± 7.96 µg/mg of dry tissue) was significantly lower than in the PV, HV, and BD groups (P<0.001). Total collagen levels in the decellularized scaffold by hepatic and PV routes were significantly higher (P<0.001) than the produced scaffold by the BD route (Fig.4C).

Extracellular matrix specific proteins detection

SEM images of the HV group showed that the decellularization process was successfully performed and the cells were completely removed while the ECM microstructure was preserved. (Fig.5A, B). Likewise, the images obtained from specific histological staining (Masson Trichrome and Von Geison) showed that major proteins of ECM were conserved in decellularized liver scaffolds and confirmed the absence of cells in the scaffolds (Fig.5C, D).

To better investigate the ECM protein components in the decellularized scaffold, we used IHC staining to evaluate the ECM specific proteins in the PV group as a better decellularized group according to the above results. IHC staining images revealed that the major and specific ECM proteins collagen type I, II, and IV, and laminin were preserved in the decellularized liver scaffold in the HV group (Fig.5E-H).

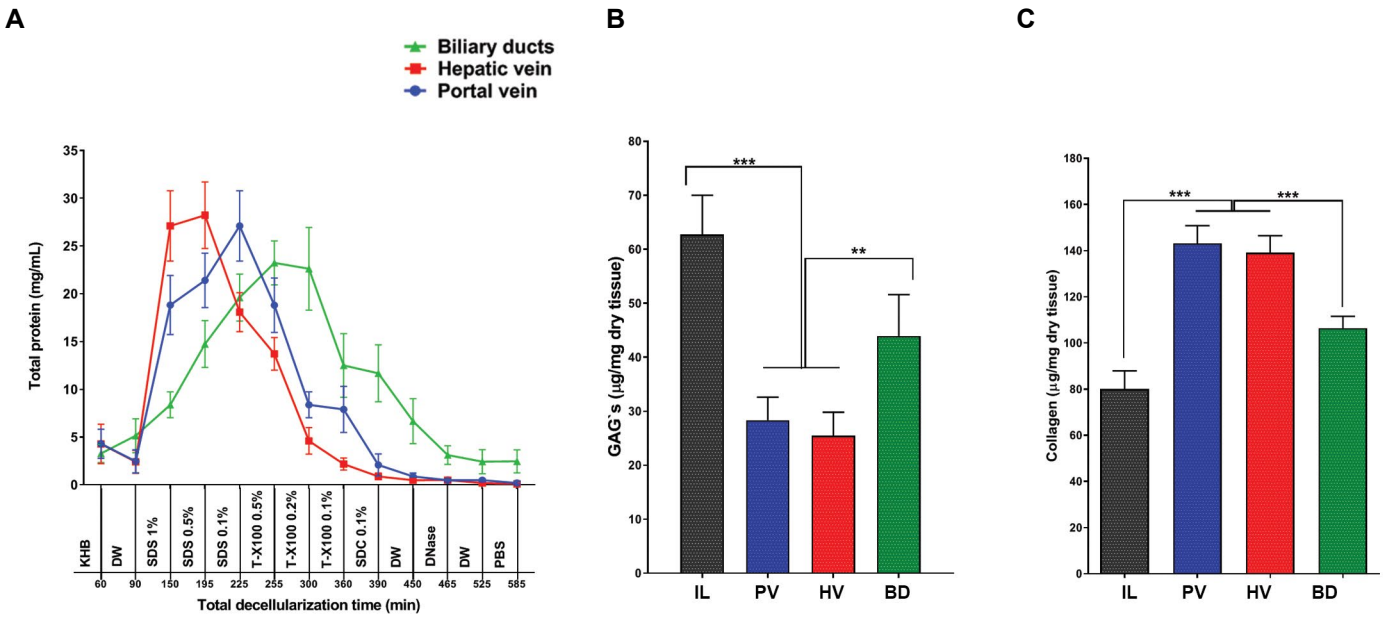

Fig.4: Quantitative comparison of ECM components. **A.** Total protein content of decellularization effluent via three different routes including the HV, PV, and BD during decellularization steps. Comparison of **B.** GAGs and **C.** Collagen contents after decellularization of rat liver via the PV, HV and BD versus IL. All data were analyzed through one-way ANOVA and by Tukey's tests and represented as mean ± SD (n=5). ECM; Extracellular matrix, HV; Hepatic vein, PV; Portal vein, BD; Biliary duct, GAGs; Glycosaminoglycans, IL; Intact liver, **; P<0.01, and ***; P<0.001.

Cytotoxicity and cell proliferation measurement

The MTT assay was used to evaluate the viability and proliferation of the cells on rat decellularized liver scaffolds at the end of days 1, 2, 3, and 7 after two cell lines culturing on the scaffolds. According to (Fig.6A), the difference between the viability of HepG2 cells in cultured plates (control) and the cells cultured on the HV, PV, and BD scaffolds was not significant during days 1 and 2. However, at days 3 and 7, the HepG2 viability for all scaffolds was significantly greater than the control group ($P<0.05$). Moreover, the viability of HepG2 cultured on scaffolds significantly increased at day 3 compared to day 2, as well as day 7 compared to day 3 ($P<0.01$ and $P<0.001$, respectively), which is an indication of cell proliferation after day 3 in the PV, HV, and BD groups.

As shown in Figure 6B, HUVEC cells viability assessment indicated a similar pattern to that of HepG2 proliferation except that in comparison with HepG2, proliferation of HUVEC cells at day 7 was more significant compared to day 3 ($P<0.0001$).

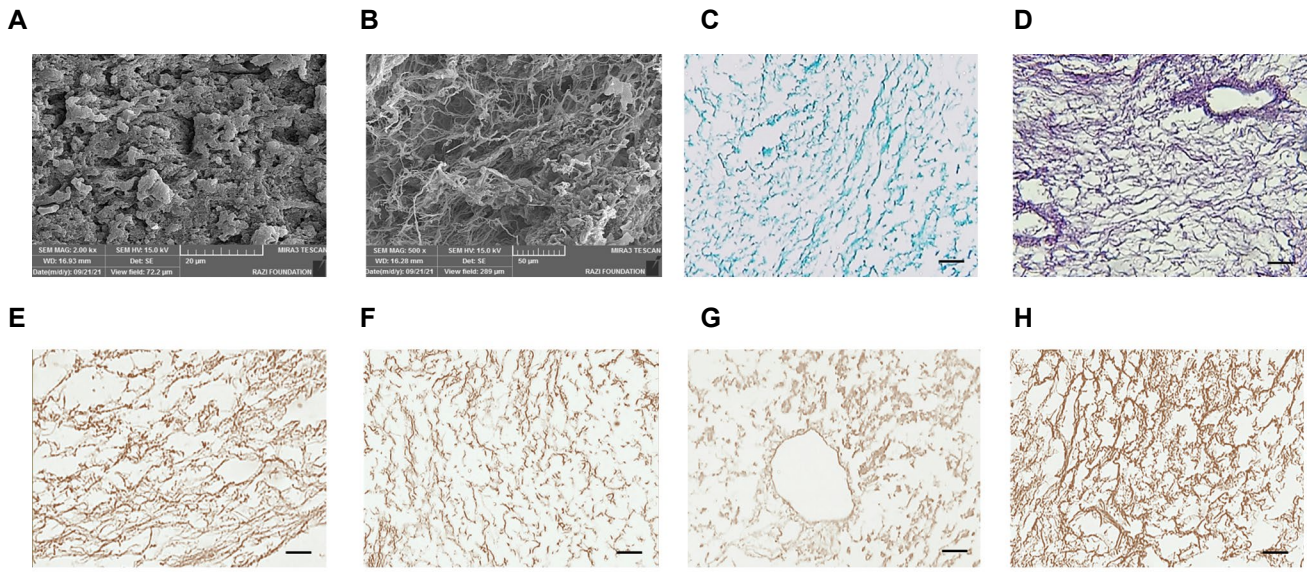

Fig.5: Evaluating the preservation of ECM component after decellularization. Representative SEM images of **A.** IL and **B.** Decellularized liver of HV group. **C.** Masson's Trichrome staining, **D.** Von Geison staining. **E.** IHC staining of collagen type I, **F.** Collagen type II, **G.** Laminin, and **H.** Collagen type IV, all for decellularized liver through the HV route (scale bar: 100 µM). ECM; Extracellular matrix, SEM; Scanning electron microscopy, IL; Intact liver, HV; Hepatic vein, and IHC; Immunohistochemical.

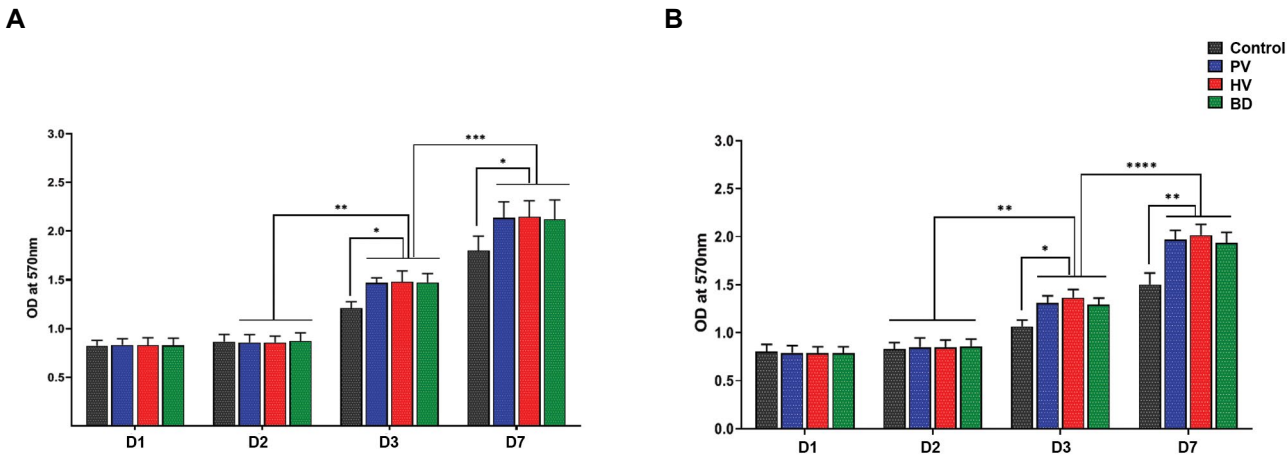

Fig.6: Cytocompatibility measurement of three types of decellularized scaffold. **A.** Evaluation of HepG2 and **B.** HUVEC viability and proliferation at days 1, 2, 3 and 7 of cell culture. All quantitative data were analyzed through one-way ANOVA and by Tukey's tests and represented as mean ± SD (n=5). HV; Hepatic vein, PV; Portal vein, BD; Biliary duct, *; $P<0.05$, **; $P<0.01$, and ***; $P<0.001$, and ****; $P<0.0001$.

Discussion

Decellularization of the whole organ has been a promising approach in tissue engineering in the recent years. This technique aims to achieve natural three-dimensional scaffolds from various allogeneic or xenogeneic origins with a preserved vascular network (17). The characteristics and quality of a decellularized scaffold are closely related to the decellularization method (18).

Many studies have evaluated different physical and chemical techniques to improve liver decellularization. For example, various detergents, different concentration of reagents, the flow rate of the solution, and perfusion conditions have been studied to improve the properties of the decellularized liver (19). But so far, there is no detailed study about the effect of the perfusion route on the outcome of the decellularization process. In this study, we evaluated the role of three different perfusion routes on rat liver decellularization.

The duration of decellularization plays an important role in the quality of the resulting scaffold. Prolonging the decellularization procedure destroys the components of the extracellular matrix, including collagen, GAGs and elastin, which leads to the weakening of the mechanical properties of the scaffold (20, 21). In this study, we reduced the decellularization time to about 8h that was enough for complete cell removal.

Tissue DNA content, visible nuclear components, and DNA fragments length are three of the most powerful tools for assessing the adequacy of tissue decellularization (22). Utilizing the PV or HV routes led to a similar pattern of DNA and protein contents in the effluents. However, this pattern was not observed in the BD route. Elution of the DNA and proteins from the liver in the PV and HV groups exhibited the effective disruption of the cellular and nuclear membrane in the first steps. Subsequently, decrease of DNA and protein contents in the middle stages indicated that most of the cells have been removed in the first stage. These results are consistent with previous decellularization studies which used the PV for liver decellularization (23, 24). In contrast, in the BD group, DNA and protein were not completely removed from the liver even during the final steps. This data revealed that decellularization through the BD was not completely successful.

One of the objects of the present study was the comparison between HV and PV routes for liver decellularization. Although there was no significant difference in the amount of the eluted proteins between these two groups, utilizing HV as the decellularization route led to a faster reduction in the amounts of DNA compared to the PV group. The DNA content in the last six decellularization steps with the HV group was significantly lower than the PV group. These results indicate that the HV is better than the PV for eluting DNA from the liver. These results demonstrate that during the decellularization process, the use of the HV route is more appropriate than the PV route in order to minimize decellularization time.

In accordance with the defined standards, the residual DNA amount should be less than 50 ng per 100 mg of the dry scaffold with no more than 200 bp length (25-27). The quantitative analysis of remaining DNA and nuclear components demonstrated that residual DNA content in the HV group was within this standard range. Furthermore, while the residual DNA length in the HV and PV groups is acceptable and DAPI staining confirmed lack of nuclear components in the decellularized scaffold in both groups, gel electrophoresis results revealed that compared to the PV group, the amount of residual DNA in the HV group is lower, DNA length is smaller, and DNA fragments length distribution is narrower. On the other hand, in the BD group we saw that higher amounts of DNA with a longer length remained, similar to the intact liver.

One of the main reasons for superiority of HV route for decellularization is the unique blood supply system of the liver, in which the PV supplies 70–75%, and the hepatic artery provides 25–30% of normal liver blood flow (28); but, total blood volume (100%) leaves the liver through the HV to maintain liver hemodynamic condition (29). Therefore, it can be concluded that the circulation capacity of the HV equals to that of the PV plus the hepatic artery. Considering the structure of liver sinusoids in which the central HV is surrounded by a triad including portal vein, hepatic artery, and biliary duct, the diameter and circulation capacity of the HV are higher than those of the PV (30). Accordingly, the time for flushing cellular debris out of the tissue was faster through the HV, so, it was better using the HV for liver decellularization.

Preservation of the ECM ultrastructure during decellularization is another critical challenge in tissue decellularization. Preservation of the structural proteins and mechanical properties of the decellularized scaffold is needed for successful production of a new engineered tissue (20). The results of IHC, specific staining of structural proteins, and electron microscopy confirmed that the ECM component and its network were preserved during decellularization through the HV or PV routes. Also, qualitative evidence of the remaining ECM proteins in the decellularized scaffold showed that in both HV and PV groups, the total GAGs and collagen levels were similar. Our data is similar to previous studies in which the total amounts of residual GAGs in the decellularized scaffolds significantly decreased in the HV and PV groups compared to the intact liver (31). It seems that this result is due to the high solubility of GAGs in aqueous solution and their removal from ECM during the decellularization protocol (31, 32). The greater collagen amount in the ECM of the HV and PV groups compared to the native and BD groups can be explained by considering the normalization method based on dry tissue weight. Intact tissues and incomplete decellularized scaffolds of the BD group mainly contain cells and insoluble collagen fibers. Thus, the weight ratio of collagen to tissue is lower than

decellularized liver. Complete decellularization mainly removes cells without insoluble collagen fibers, resulting in an increased ECM portion in dry tissue weight (9). It is necessary to consider the mentioned fact to explain controversial results from previous studies; different parameters of the decellularization protocols such as various types of detergents, concentrations, and tissues exposing time during decellularization, profoundly affect the preservation of ECM structure and content (31, 33, 34). Similar to other studies, our investigation with the IHC technique revealed that major ECM proteins, such as collagen type I, II, IV, and laminin were preserved in the HV decellularized scaffold as the best group with minimal residual DNA and maximal conserved ECM components.

Biocompatibility is the most important property of a scaffold. Studies have shown that residual decellularization agents such as SDS and Triton X100 can leave cytotoxic effects on the decellularized scaffold (35). Therefore, it is necessary to wash the tissue carefully at the end of the decellularization process. In this study, after the last step of decellularization, the decellularized tissue was thoroughly washed in two steps, with distilled water and PBS (each for one hour), respectively. Furthermore, for culture of the cells, the decellularized tissue pieces were incubated for 24 hours in DMEM to ensure the complete removal of reagents residues. Evaluating the cell viability of three types of decellularized scaffolds revealed that all scaffolds are biocompatible and suitable for cellular repopulation. These results confirmed that the decellularized liver could be used as a natural scaffold for liver regeneration (36, 37). The human liver carcinoma cell line (HepG2) is most commonly used because of the advantages of availability and maintenance, the features characteristic of normal hepatocytes (38). As well, human umbilical vein endothelial cells (HUVECs) are one of the most popular cell line used as an *in vitro* model for endothelial cells (39). We used these two different cell lines to assess cell proliferation on decellularized liver scaffolds because the liver is composed of many different cell types in which, hepatocytes and endothelial cells have some essential performances as two types of primary cells (non-parenchymal cells) (40).

More studies would be required to evaluate the recellularization efficiency of the scaffolds following different decellularization strategies. Besides, additional preclinical studies should investigate the liver function in animal models to enhance the translation of preclinical results to clinical practice.

Conclusion

The present study demonstrated that rat decellularized liver scaffold could be obtained from different decellularization routes such as the HV, PV, and BD. The results of these experiments revealed that the HV is a more suitable route than the PV for rat liver decellularization.

Acknowledgments

The authors keep alive the name and memory of the late Professor Peyravi. The authors would like to thank the staff of the Department of Pharmacology, School of Medicine, Shahid Beheshti University of Medical Sciences. Research reported in this publication is a part of a Ph.D. thesis, which was supported by Vice-Chancellor's in Research Affairs of Shahid Beheshti University of Medical Sciences, Tehran, Iran. Also, this research was supported by the Research Grant Committee from the National Institutes for Medical Research Development (NIMAD), Tehran, Iran, under award number of 963951. There is no conflict of interest in this study.

Authors' Contributions

B.J.N., H.N.; Contributed to conception and design. B.J.N.; Contributed to all experimental work, data and statistical analysis, interpretation of data, and drafted the manuscript which was revised by M.-M.K., T.T., A.B. M.-M.K.; Contributed to validation and formal analysis. T.T., A.B.; Participated in methodology and data analysis. H.N.; Was responsible for supervision. All authors read and approved the final manuscript.

References

1. Mazza G, Al-Akkad W, Rombouts K, Pinzani M. Liver tissue engineering: from implantable tissue to whole organ engineering. Hepatol Commun. 2018; 2(2): 131-141.
2. Jadlowiec CC, Taner T. Liver transplantation: current status and challenges. World J Gastroenterol. 2016; 22(18): 4438-4445.
3. Hillebrandt KH, Everwien H, Haep N, Keshi E, Pratschke J, Sauer IM. Strategies based on organ decellularization and recellularization. Transpl Int. 2019; 32(6): 571-585.
4. Zhou P, Huang Y, Guo Y, Wang L, Ling C, Guo Q, et al. Decellularization and recellularization of rat livers with hepatocytes and endothelial progenitor cells. Artif Organs. 2016; 40(3): E25-E38.
5. Wang X, Cui J, Zhang BQ, Zhang H, Bi Y, Kang Q, et al. Decellularized liver scaffolds effectively support the proliferation and differentiation of mouse fetal hepatic progenitors. J Biomed Mater Res A. 2014; 102(4): 1017-1025.
6. Keane TJ, Swinehart IT, Badylak SF. Methods of tissue decellularization used for preparation of biologic scaffolds and in vivo relevance. Methods. 2015; 84: 25-34.
7. Crapo PM, Gilbert TW, Badylak SF. An overview of tissue and whole organ decellularization processes. Biomaterials. 2011; 32(12): 3233-3243.
8. Gilpin A, Yang Y. Decellularization strategies for regenerative medicine: from processing techniques to applications. Biomed Res Int. 2017; 2017: 9831534.
9. Coronado RE, Somaraki-Cormier M, Natesan S, Christy RJ, Ong JL, Halff GA. Decellularization and solubilization of porcine liver for use as a substrate for porcine hepatocyte culture: method optimization and comparison. Cell Transplant. 2017; 26(12): 1840-1854.
10. Park KM, Park SM, Yang SR, Hong SH, Woo HM. Preparation of immunogen-reduced and biocompatible extracellular matrices from porcine liver. J Biosci Bioeng. 2013; 115(2): 207-215.
11. Hussein KH, Park KM, Kang KS, Woo HM. Biocompatibility evaluation of tissue-engineered decellularized scaffolds for biomedical application. Mater Sci Eng C Mater Biol Appl. 2016; 67: 766-778.
12. Abshagen K, Kuhla A, Genz B, Vollmar B. Anatomy and physiology of the hepatic circulation. In: Lanzer P, editor. PanVascular medicine. Berlin, Heidelberg: Springer Berlin Heidelberg; 2015: 3607-3629.
13. Gilbert TW. Strategies for tissue and organ decellularization. J Cell Biochem. 2012; 113(7): 2217-2222.
14. De Kock J, Ceelen L, De Spiegelaere W, Casteleyn C, Claes P, Vanhaecke T, et al. Simple and quick method for whole-liver decellularization: a novel in vitro three-dimensional bioengineering tool? Arch Toxicol. 2011; 85(6): 607-612.

15. Farndale RW, Buttle DJ, Barrett AJ. Improved quantitation and discrimination of sulphated glycosaminoglycans by use of dimethylmethylene blue. Biochim Biophys Acta. 1986; 883(2): 173-177.
16. Reddy GK, Enwemeka CS. A simplified method for the analysis of hydroxyproline in biological tissues. Clin Biochem. 1996; 29(3): 225-229.
17. Badylak SF, Taylor D, Uygun K. Whole-organ tissue engineering: decellularization and recellularization of three-dimensional matrix scaffolds. Annu Rev Biomed Eng. 2011; 13: 27-53.
18. Gilbert TW, Sellaro TL, Badylak SF. Decellularization of tissues and organs. Biomaterials. 2006; 27(19): 3675-3683.
19. Struecker B, Butter A, Hillebrandt K, Polenz D, Reutzel-Selke A, Tang P, et al. Improved rat liver decellularization by arterial perfusion under oscillating pressure conditions. J Tissue Eng Regen Med. 2017; 11(2): 531-541.
20. Gilpin A, Yang Y. Decellularization strategies for regenerative medicine: from processing techniques to applications. Biomed Res Int. 2017; 2017: 9831534.
21. Fazelian-Dehkordi K, Ardekani SFM, Talaei-Khozani T. Quality comparison of decellularized omentum prepared by different protocols for tissue engineering applications. Cell J. 2022; 24(5): 267-276.
22. Gilbert TW, Freund JM, Badylak SF. Quantification of DNA in biologic scaffold materials. J Surg Res. 2009; 152(1): 135-139.
23. Wang Y, Bao J, Wu Q, Zhou Y, Li Y, Wu X, et al. Method for perfusion decellularization of porcine whole liver and kidney for use as a scaffold for clinical-scale bioengineering engrafts. Xenotransplantation. 2015; 22(1): 48-61.
24. Wang LR, Lin YQ, Wang JT, Pan LL, Huang KT, Wan L, et al. Recent advances in re-engineered liver: de-cellularization and re-cellularization techniques. Cytotherapy. 2015; 17(8): 1015-1024.
25. Soto-Gutierrez A, Zhang L, Medberry C, Fukumitsu K, Faulk D, Jiang H, et al. A whole-organ regenerative medicine approach for liver replacement. Tissue Eng Part C Methods. 2011; 17(6): 677-686.
26. Mazza G, Al-Akkad W, Telese A, Longato L, Urbani L, Robinson B, et al. Rapid production of human liver scaffolds for functional tissue engineering by high shear stress oscillation-decellularization. Sci Rep. 2017; 7(1): 5534.
27. Sabetkish S, Kajbafzadeh AM, Sabetkish N, Khorramirouz R, Akbarzadeh A, Seyedian SL, et al. Whole-organ tissue engineering: decellularization and recellularization of three-dimensional matrix liver scaffolds. J Biomed Mater Res A. 2015; 103(4): 1498-1508.
28. Eipel C, Abshagen K, Vollmar B. Regulation of hepatic blood flow: the hepatic arterial buffer response revisited. World J Gastroenterol. 2010; 16(48): 6046-6057.
29. Lautt WW. Hepatic circulation: physiology and pathophysiology. San Rafael (CA): Morgan & Claypool Life Sciences; 2009.
30. Treyer A, Musch A. Hepatocyte polarity. Compr Physiol. 2013; 3(1): 243-287.
31. Taylor DA, Kren SM, Rhett K, Robertson MJ, Morrissey J, Rodriguez OE, et al. Characterization of perfusion decellularized whole animal body, isolated organs, and multi-organ systems for tissue engineering applications. Physiol Rep. 2021; 9(12): e14817.
32. Wu Q, Bao J, Zhou YJ, Wang YJ, Du ZG, Shi YJ, et al. Optimizing perfusion-decellularization methods of porcine livers for clinical-scale whole-organ bioengineering. Biomed Res Int. 2015; 2015: 785474.
33. Maghsoudlou P, Georgiades F, Smith H, Milan A, Shangaris P, Urbani L, et al. Optimization of liver decellularization maintains extracellular matrix micro-architecture and composition predisposing to effective cell seeding. PLoS One. 2016; 11(5): e0155324.
34. Willemse J, Verstegen MMA, Vermeulen A, Schurink IJ, Roest HP, van der Laan LJW, et al. Fast, robust and effective decellularization of whole human livers using mild detergents and pressure controlled perfusion. Mater Sci Eng C Mater Biol Appl. 2020; 108: 110200.
35. Gratzer PF, Harrison RD, Woods T. Matrix alteration and not residual sodium dodecyl sulfate cytotoxicity affects the cellular repopulation of a decellularized matrix. Tissue Eng. 2006; 12(10): 2975-2983.
36. Yang W, Xia R, Zhang Y, Zhang H, Bai L. Decellularized liver scaffold for liver regeneration. Methods Mol Biol. 2018; 1577: 11-23.
37. Hosseini V, Maroufi NF, Saghati S, Asadi N, Darabi M, Ahmad SNS, et al. Current progress in hepatic tissue regeneration by tissue engineering. J Transl Med. 2019; 17(1): 383.
38. Arzumanian VA, Kiseleva OI, Poverennaya EV. The curious case of the HepG2 cell line: 40 years of expertise. Int J Mol Sci. 2021; 22(23): 13135.
39. Cao Y, Gong Y, Liu L, Zhou Y, Fang X, Zhang C, et al. The use of human umbilical vein endothelial cells (HUVECs) as an in vitro model to assess the toxicity of nanoparticles to endothelium: a review. J Appl Toxicol. 2017; 37(12): 1359-1369.
40. Panwar A, Das P, Tan LP. 3D hepatic organoid-based advancements in liver tissue engineering. Bioengineering (Basel). 2021; 8(11): 185.

Cell J
Cell Journal(Yakhteh) Homepage: https://www.celljournal.org/
Original Article Vol 25, No 1, January 2023, Pages: 45-50

TIMPs Expression as A Maternal Cell Free Plasma Biomarker of Severe Preeclampsia: A Case-Control Study

Sara Seydabadi, M.Sc.[1], Habib Nikukar, M.D., Ph.D.[1], Fahimeh Ghotbizadeh Vahdani, M.D.[2], Fariba Ramazanali, M.D.[3], Maryam Shahhoseini, Ph.D.[4], Raha Favaedi, M.Sc.[4], Azadeh Ghaheri, Ph.D.[5], Elham Etesami, M.Sc.[1], Mohammadreza Zamanian, M.D., Ph.D.[4*]

1. Medical Nanotechnology and Tissue Engineering Research Center, Yazd Reproductive Sciences Institute, Shahid Sadoughi University of Medical Sciences, Yazd, Iran
2. Obstetrics and Gynecology Department, Tehran University of Medical Science, Tehran, Iran
3. Department of Endocrinology and Female Infertility, Reproductive Biomedicine Research Center, Royan Institute for Reproductive Biomedicine, ACECR, Tehran, Iran
4. Department of Genetics, Reproductive Biomedicine Research Center, Royan Institute for Reproductive Biomedicine, ACECR, Tehran, Iran
5. Department of Epidemiology and Reproductive Health, Reproductive Epidemiology Research Center, Royan Institute for Reproductive Biomedicine, ACECR, Tehran, Iran

Corresponding Address: P.O.Box: 16635-148, Department of Genetics, Reproductive Biomedicine Research Center, Royan Institute for Reproductive Biomedicine, ACECR, Tehran, Iran
Email: mrzamanian@royaninstitute.org

Received: 14/September/2021, Revised: 15/April/2022, Accepted: 22/May/2022

Abstract

Objective: Preeclampsia (PE) is a pregnancy related disorder with prevalence of 6-7%. Insufficient trophoblastic invasion leads to incomplete remodeling of spiral arteries and consequent decrease in feto-placental perfusion. Altered placental expression of tissue inhibitors of matrix metalloproteinase (TIMPs) is considered to be involved in this process while the balance between matrix metalloproteinases (MMPs) and TIMPs contributes to remodeling of the placenta and uterine arteries by degradation and refurbishing of extracellular matrix (ECM). Therefore, TIMPs, fetal expression pattern was evaluated with the aim of its potential to be used as a determinant for the (early) detection of PE.

Materials and Methods: In this case-control study, cell free fetal RNA (cffRNA) released by placenta into the maternal blood was used to determine expression patterns of *TIMP1, 2, 3* and *4* in the severe preeclamptic women in comparison with the normal pregnant women. Whole blood from 20 preeclamptic and 20 normal pregnant women in their 28-32 weeks of gestational age was collected. The second control group consisted of 20 normal pregnant women in either 14 or 28 weeks of gestation (each 10). cffRNA was extracted from plasma and real-time polymerase chain reaction (PCR) was done to determine the expression levels of *TIMP1, 2, 3* and *4* genes.

Results: Statistical analysis of the results showed significant higher expression of *TIMP1-4* in the preeclamptic women in comparison with the control group (P=0.029, 0.037, 0.037 and 0.049, respectively). Also, an increased level of *TIMPs* expression was observed by comparing 14 to 28 weeks of gestational age in the normal pregnant women in the second control group.

Conclusion: An increased cffRNA expression level of *TIMPs* may be correlated with the intensity of placental vascular defect and may be used as a determinant of complicated pregnancies with severe preeclampsia.

Keywords: Cell Free Fetal RNA, Gene Expression, Preeclampsia, Tissue Inhibitors of Matrix Metalloproteinase

Citation: **Seydabadi S, Nikukar H, Ghotbizadeh Vahdani F, Ramazanali F, Shahhoseini M, Favaedi R, Ghaheri A, Etesami E, Zamanian MR. TIMPs expression as a maternal cell free plasma biomarker of severe preeclampsia: a case-control study. Cell J. 2023; 25(1): 45-50. doi: 10.22074/CELLJ.2022.557259.1041.**

Introduction

Preeclampsia (PE), a multi-system disorder of pregnancy, is diagnosed by new onset of hypertension and proteinuria after 20 weeks of gestation in a previously normotensive woman. A systolic blood pressure>160 mmHg or diastolic blood pressure >110 mmHg defines severe preeclampsia. PE is one of the leading causes of maternal/fetal morbidity and mortality, which affects 6-7% of all pregnancies (1). The main etiology of PE is still unclear, but it seems that several factors such as placenta are largely involved. While there is not a general agreement on the amount of proteinuria to define the severity (2) although, several other symptoms such as edema, renal or liver failure and the hemolysis, elevated liver enzymes and low platelet counts (HELLP syndrome) may also develop based on organ involvement (1). PE can lead to early-onset of severe hypertension accompanied with a fetal growth restriction that requires pregnancy termination before 34 weeks of gestation. Late-onset mild hypertension that needs to terminate the conception or after 34 weeks of gestation with a normally grown fetus may also represent as a milder form of the disease (3). It is assumed that the poor cytotrophoblastic invasion in the PE leads to abnormal remodeling of the uterine arteries and inadequate oxygen delivery to developing utero-placental unit (4). This will consequently lead to placental endothelial dysfunction and oxidative stress (5). Delivery of the placenta and fetus is the only treatment to prevent maternal organ injury (6), while early detection of PE helps to plan appropriate monitoring and clinical

management (7).

The recent discovery of fetal cells and cell free fetal nucleic acids in the maternal blood has provided a new possibility for a non-invasive prenatal diagnosis (8). Analysis of fetal RNAs in the maternal plasma has also produced valuable information about the condition of gene expression in fetal tissues in the complicated pregnancies. The cell free fetal RNA (CffRNA) was not expected to be present in the plasma due to the presence and action of ribonuclease (RNAses) (8, 9). However, recent studies revealed an altered level of placental-specific mRNA coding for corticotrophin releasing hormone (CRH) in the PE (10). In addition, cell-free mRNA concentrations of CRH, PLAC1, and P-selectin are increased in the plasma of pregnant women with preeclampsia (11).Subsequently, it was postulated that the placental-expressed mRNAs were encapsulated within a syncytiotrophoblast-derived microvesicle (STBM), which provides RNase resistance to "cell free" fetal RNA in the maternal plasma in comparison with the maternal RNA (11). It is known that tissue inhibitors of matrix metalloproteinase (TIMPs) adjust the matrix metalloproteinases (MMPs) activity in different stages of pregnancy (12, 13). So during pregnancy, the level of MMPs/TIMPs activity plays an important role in the uterine spiral arteries remodeling through governing cytotrophoblastic invasion (14, 15). This suggests that MMP/TIMP imbalances could have an important role in the implantation failure and placental development (16).

Actually the expression pattern of *TIMPs* gene family has been previously evaluated in the PE using samples from placenta or whole RNA (but not the fetal component) from maternal plasma. In this study and for the first time, we used maternal blood and cell free fetal RNA to compare those with and without PE (fetal component) with the aim of its potential application for early and non-invasive prenatal screening/diagnosis.

Material and Methods

Samples were provided by the prenatal unit, Imam Khomeini Hospital Complex, Tehran, Iran. A written informed consent, approved by the Royan institutions' Ethical Committee of the Research Council, Tehran, Iran (IR.ACECR.ROYAN.REC.1394.24) was received from all the participants.

Study groups

In this pilot case-control study, twenty severe preeclamptic women that suffered of average proteinuria of 3+ and systolic blood pressure ≥ 160 mmHg or diastolic blood pressure ≥110 mmHg) participated and also, twenty normal pregnant women were included as a matched control group in their 28-32 weeks of gestational age. We also evaluated the second control group which consisted of 10 pregnant women in 14 and 10 other pregnant women at 28 weeks of gestational age as an additional investigation.

All participants aged 20 to 45 years old. Chronic hypertension before 20 weeks of pregnancy, history of gestational diabetes and kidney disease comprise our exclusion criteria. Actually, the normal control women were experiencing their first or subsequent pregnancies and all of them did not have any history of PE in their previous pregnancies. The sample size was based on the similar published works (17).

Plasma collection

To find out the probable variability of *TIMPs* cell free fetal expression level, as potential biomarkers for severe preeclampsia, we collected blood samples of the normal pregnancy at 14 weeks of GA and 28 weeks of GA.

Peripheral blood (10 ml) was collected from all 60 participants (20 PE cases, 20 normal pregnant gestational matched controls and 10+10 normal as a second control group at 14 or 28 weeks) in a K3EDTA tube (BD Biosciences, USA). Then, the tubes were centrifuged at 1600 g for 10 minutes at 4ºC. Plasma was carefully separated and transferred into 1.5 mL micro tubes (GUNSTER BIOTECH, TAIWAN). The plasma was re-centrifuged at 16000 g for 10 minutes and 4ºC. Then supernatants were transferred into 2 mL cryovials (SPL LIFE SCIENCES, Korea). The plasma samples were frozen in liquid nitrogen and stored at -70ºC.

Extraction of cell free fetal RNA and cDNA synthesis

The plasma samples were centrifuged at 16000 g for 5 minutes at 4ºC following melting at room temperature. Extraction of cffRNA was done from 3 mL of plasma according to manufacturer's protocol (Cat. No. 55114, QIAamp Circulating Nucleic Acid Kit, Qiagen, Germany). CffRNA was eluted in the AVE buffer (Cat. No. 55114, QIAamp Circulating Nucleic Acid Kit, Qiagen, Germany) and stored at -70ºC until later use. Using reverse transcription process (RT) and following manufacturer's protocol (Cat. No. 11754, SuperScript VILO cDNA Synthesis Kit, Invitrogen, USA.) complementary DNA (cDNA) was produced from each RNA template.

Real time polymerase chain reaction

Primers were designed by the Perl Primer (Table 1) and cell free fetal mRNA of *TIMP* genes were amplified. As housekeeping control gene, *18s* was employed. Real time polymerase chan reaction (PCR) was set up using SYBR green, according to the manufacturer's instructions (Cat No: 4367659, Applied Biosystems by Thermo Fisher Scientific, USA) in a reaction volume of 20 µL (each reaction contained: 5 µL SYBR green, 1 µL forward

and 1 µL reverse primer of 100 Pico mole/µL, 2 µL cDNA with concentration of 50 ng per µL and deionized water). Reactions were prepared in duplicate. In each PCR run, cDNA sample of preeclamptic women and their matched controls were examined under the same condition. cDNA samples from the second control group were evaluated in separate reactions. Real time PCR was carried out as follows: primary denaturation for 4 minutes at 95ºC, 10 seconds of denaturation at 95ºC followed by 1 minute of annealing/extension at 60ºC (repeated for 45 cycles), and ultimately the melt curve analysis for 15 seconds started at 95ºC. Normalization of data was performed using *18s* as housekeeping gene (ΔCt). The comparative threshold cycle method was used to calculate the changes in the relative gene expression ($2^{-\Delta\Delta Ct}$).

Table 1: Primer sequences for *TIMPs* real time polymerase chain reaction reactions

Gene	Primer sequences (5´-3´)	Product size (bp)
18s	F: GTAACCCGTTGAACCCCATT	151
	R: CCATCCAATCGGTAGTAGCG	
TIMP1	F: GAA GTC AAC CAG ACC ACC T	181
	R: TTC CAG CAA TGA GAA ACT CCT	
TIMP2	F: CGACATTTATGGCAACCCT	217
	R: GCACGATGAAGTCACAGAG	
TIMP3	F: CAAGCAGATGAAGATGTACCGA	228
	R: GTGATACCGATAGTTCAGCCC	
TIMP4	F: CTGCCAAATCACCACCTG	193
	R: CGATGTCAACAAACTCCTTCC	

Statistical analysis

The results were analyzed using SPSS software (Version 16.0, IBM, USA). Normalization of the result was validated by the one sample K-S test (normal distribution: P>0.05). T test was used to compare the relative expression of *TIMP* genes in preeclampsia, first and second normal groups. The P≤0.05 were considered as statistically significant.

Results

The main demographic and biophysical features of the study groups are summarized in Table 2. Totally, 60 samples were analyzed, including 20 preeclamptic and 40 normal pregnant women. We evaluated cell free expression patterns of *TIMP* genes of maternal plasma. The results indicated a significant increase in the *TIMPs* expression of the preeclamptic group in comparison with the matched normal group (P≤0.05, Fig.1).

To find out the probable variability of *TIMPs* cell free fetal expression level, as potential sever PE biomarkers, we collected blood samples of the normal pregnancy at 14 weeks, of GA and 28 weeks of GA. In second control group the results confirmed the presence of all *TIMP*s expression in both 14 and 28 weeks of normal pregnancies while the level of expression was relatively increased from 14 to 28 weeks of gestational age. Enhanced expression in 28 weeks compared to 14 weeks (along with the increase in the placental mass) confirms the placenta as the source of fetal cell free RNAs (Fig.2).

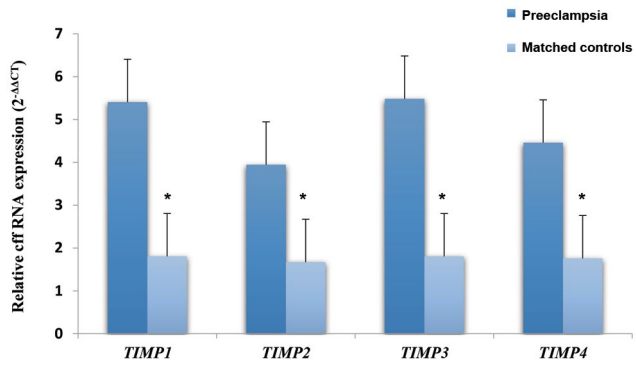

Fig.1: Plot of real-time polymerase chain reaction analysis of *TIMP1, TIMP2, TIMP3,* and *TIMP4* gene expression in maternal plasma of preeclamptic (PE) pregnancies versus their matched control group using cell free fetal RNA (cffRNA). All *TIMPs* showed significant increase in PE pregnancies compared to matched control. *; P=0.029, 0.037, 0.037, and 0.049, respectively.

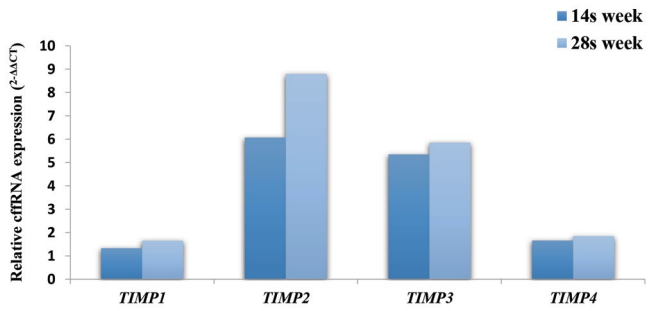

Fig.2: Plot of real-time polymerase chain reaction analysis of *TIMP1, TIMP2, TIMP3,* and *TIMP4* gene expression in maternal plasma of 14 weeks healthy pregnancies in comparison with 28 weeks normal pregnancies using cell free fetal RNA. Enhanced expression in 28 weeks compared to 14 weeks (along with the increase in the placental mass) indicates placenta as the source of detected cell free RNAs.

Table 2: Demographic and biophysical variables of case and control group

Charactristics	Normal pregnant women (matched control group)	Severe preeclamptic women (case group)
Sample size (n)	20	20
Age (Y)	28.2 ± 4.7	32.7 ± 5.2
Systolic blood pressure (mmHg)	112.0 ± 7.1	165.0 ± 14
Diastolic blood pressure (mmHg)	80.5 ± 6.0	111.5 ± 8.7
Proteinuria (1-4 plus), median (IQR)	-	+3 (+2 to +4)
Gestational age (weak)	30.4 ± 1.5	30.6 ± 1.5

Data are presented as mean ± SD. SD; Standard deviation and IQR; Interquartile range.

Discussion

PE, an important cause of prenatal morbidity, leads to at least 50 thousands of annual maternal deaths all around the world. It is clinically diagnosed by the de novo hypertension and proteinuria after 20 weeks of gestation (18). The trophoblastic cells invasion reduction is considered as the central process of the PE pathophysiology which in turn leads to an incomplete remodeling of maternal spiral arteries and ultimately, the poor placental invasion (5). Currently, the only treatment to prevent maternal organ injury is pregnancy termination as soon as possible and delivery of the placenta and fetus (6).

It is known that in the normal pregnancies, artery remodeling changes, including angiogenesis and trophoblastic invasion are maintained by the specific enzymes, MMP/TIMP (19). In pregnancies complicated by preeclampsia, an imbalance in MMP/TIMP activity may cause poor placental perfusion (13, 15). There are different TIMPs protein in human (TIMP1-4) which all act as endogenous inhibitors of active MMPs protein (20). TIMP proteins are crucial enzymes for the invasion processes of different types of cells, including cytotrophoblasts invading the uterus in human placentation (21).

There is not available, a clinically efficient screening test to accurately predict the occurrence of PE before its clinical onset (7). Discovery of placental/fetal mRNA in the maternal plasma may be a promising noninvasive biomarker (22). Cell free fetal mRNA unlike cffDNA is not dependent on the fetal gender and genotype (23). Also, a placenta derived mRNA, that is detectable in the maternal plasma at 4 weeks of gestation, is rapidly cleared after delivery (6).

Several studies have previously examined the expression patterns of *TIMP* genes at the protein level and reported significant changes in preeclamptic mothers (14, 24-26). To the best of our knowledge, there are no report to examine maternal plasma and fetal fractions of cell free RNA. The present study has provided a compilation of the cffRNA expression of *TIMP* genes ofthematernal plasma. Wecomparedit in the preeclamptic affected with thenormal pregnancies. Accordingly, wereport herefor the first time,a significant change in the degree of cffRNA expression in plasma of PE pregnancies.

TIMP1, a specific inhibitor of MMP9 and a proteolytic enzyme, mainly degrades the extracellular matrix (ECM). It also has an important role in a trophoblastic invasion (27). In pregnancies complicated with PE, an increased level of TIMP1 protein prevents the endothelial cell migration in the uterine vessels which may lead to an incomplete remodeling of spiral arteries (13, 14, 28). For the first time, we evaluated the expression of *TIMP1* gene in the maternal plasma using cffRNA, which showed a significant increase in the PE women in comparison with the normal matched control group. This is consistent with previous studies that reported an increased levels of TIMP1 protein in the placental cells of PE groups (29).

TIMP2, the specific inhibitor of MMP2 (30), acts as the first mediator of trophoblast invasion into the endometrium. It also participates in the remodeling of arteries and angiogenesis in early pregnancy (31, 32). In normal pregnancies, physiologic remodeling of the endothelial layer and degradation of elastic muscular-vascular tissues may increase the blood supply to the developing fetus (14). However, in preeclampsia, collagen aggregation reduces the vessel wall elasticity and blood supply to the fetus where ultimately hypoxic damage happens. Increased level of TIMP2 and or decreased amounts of MMP2 may lead to the collagen aggregation (14) which is the triggers of preeclampsia. According to our data, the expression level of *TIMP2* cffRNA in the PE group showed a significant increase in comparison with the normal matched control group. This is also in agreement with the results of previous studies of placenta samples (13, 14).

TIMP3 is expressed in various tissues, and shows highest expression in the placenta. TIMP3 is considered as an effective factor in the process of fetal implantation and decidualization through regulating trophoblast invasion (25). Increased expression of TIMP3 protein inhibits the ECM degradation which is necessary for an efficient implantation through inhibition of MMPs (28, 32). Also,

TIMP3 protein prohibits the trophoblast invasion and leads to a defective remodeling of spiral arteries in the PE women (25, 33). Our results confirm a significant increase in the *TIMP3* expression in maternal blood of the PE group in comparison to the normal matched control group, which is in accordance with the previous reports (24, 25, 29).

The present study also indicates a significant increase in the *TIMP4* expression of the plasma cffRNA content of the preeclamptic participants in comparison with our normal matched control group. This finding verifies the result of the only previous study that showed elevated plasma protein levels of TIMP-4 in the PE pregnancies in comparison with the chronic hypertensive cases (26). The relatively higher potency of TIMP4 action on the MMP2 pathway compared with other *MMPs* gene, suggests that *TIMP4* similar to *TIMP2* effects more specific on the *MMP2* gene (34). As important role players in the ECM, MMPs develop the endothelial cell migration and trigger angiogenesis. TIMP4 has an anti-angiogenesis activity and prevents formation of endothelial cell tube (35, 36). Therefore, the increased expression of *TIMP4* in PE could be a possible reason of the spiral arteries invasion limitation, which in turn will reduce the blood supply to the fetus and triggers hypertension in the pregnant women (14, 34).

Co-expression of *MMPs* and *TIMPs* in the trophoblasts suggests that the invasive and lytic properties of cells effects on the ECM depend on the MMPs/TIMPs balance (37). Increased expression of *TIMP*s can possibly reduce MMPs function which in turn may suppress matrix disintegration necessary for efficient implantation. This can also inhibit the trophoblast invasion that leads to an incomplete modification of spiral arteries. Particularly, an impaired remodeling of the spiral arteries have been considered as a major contributor to the PE (24, 25).

For a quite long time, non-invasive PE-specific markers have been introduced. For the first time in the present study, the *TIMPs* cffRNA expression of maternal plasma was evaluated and we observed a significant elevated expression in the PE patients in comparison with the normal matched control pregnancies. In addition, we detected the presence of *TIMP*s expression in the 14 weeks GA as well as 28 weeks GA in the healthy second control group pregnant women that showed a relative increase in the latter one. Our finding shows that *TIMPs* expression is detectable from early pregnancy due to the placenta origin of the cell free nucleic acid. An increase in gestational age associated with the subsequent placental size may be accompanied by higher amounts of cell free fetal RNA in the maternal plasma. Taking all together, the expression level of *TIMPs* cell free fetal may determine placental health and may reflect the severity of the preeclamptic disorders. Further studies are needed to give promise of biomarkers for early detection/prognosis of complicated pregnancies such as preeclampsia. Also, a follow-up case control study is needed to be able to clearly determine the cause and effect relationship. Although, due to the limitations in recruitment of the patients/controls, current setup was used. Therefore, further studies will be required to validate our results and to define the detection thresholds through integrated bioinformatics calculations.

Conclusion

Cell free fetal RNA derived from the placenta and released to maternal plasma creates a promising approach for noninvasive prenatal diagnosis independent of fetal gender and genotype. Here, we concluded that the pattern of fetal *TIMPs* expression within maternal plasma can be used as a potential PE biomarker in early pregnancy.

Acknowledgments

We thank all the patients and staff at Imam Khomeini Hospital (Tehran, Iran) and the Clinic of Royan Institute (Tehran, Iran) for their kind collaboration. This research was financially supported by the Shahid Sadoughi University of Medical Sciences, Yazd, Iran and the Royan Institute for Reproductive Biomedicine, Tehran, Iran. These costs included laboratory chemicals and materials. The authors declare that they have no conflicts of interest in this study.

Authors' Contribution

S.S.; In charge of practical lab works, drafting the manuscript, and was responsible for sample collection. H.N., M.Sh.; Involved in developing the concept and experimental design. F.Gh.V., F.R.; Involved in clinical management and sample collection. R.F.; Involved in the laboratory part of the project and helped in primer designing. A.Gh.; Involved in statistical analysis of data. E.E.; Involved in data generating helped in sample collection. M.Z.; Designed and supervised the project, data interpretation, and drafting and revision of the manuscript. All authors read and approved the final manuscript.

References

1. Malmström O, Morken NH. HELLP syndrome, risk factors in first and second pregnancy: a population-basedcohort study. Acta Obstet Gynecol Scand. 2018; 97(6): 709-716.
2. Webster K, Fishburn S, Maresh M, Findlay SC, Chappell LC; Guideline Committee. Diagnosis and management of hypertension in pregnancy: summary of updated NICE guidance. BMJ. 2019; 366: l5119.
3. Park HJ, Shim SS, Cha DH. Combined screening for early detection of pre-eclampsia. Int J Mol Sci. 2015; 16(8): 17952-17974.
4. Armaly Z, Jadaon JE ,Jabbour A, Abassi ZA. Preeclampsia: novel mechanisms and potential therapeutic approaches. Front Physiol. 2018; 9: 973.
5. Phipps E, Prasanna D, Brima W, Jim B. Preeclampsia: updates in pathogenesis, definitions, and guidelines. Clin J Am Soc Nephrol. 2016; 11(6): 1102.
6. Duhig K, Vandermolen B, Shennan A. Recent advances in the di-

agnosis and management of pre-eclampsia. F1000Res. 2018; 7: 242.
7. Mayrink J, Costa ML, Cecatti JG. Preeclampsia in 2018: Revisiting concepts, physiopathology, and prediction. ScientificWorldJournal. 2018; 2018: 6268276.
8. Kim SY, Kim HJ, Park SY, Han YJ, Choi JS, Ryu HM. Early Prediction of hypertensive disorders of pregnancy using cell-free fetal DNA, cell-free total DNA, and biochemical markers. Fetal Diagn Ther. 2016; 40(4): 255-262.
9. Hahn S, Rusterholz C, Hösli I, Lapaire O. Cell-free nucleic acids as potential markers for preeclampsia. Placenta. 2011; 32 Suppl: S17-S20.
10. Zhong XY, Gebhardt S, Hillermann R, Tofa KC, Holzgreve W, Hahn S. Parallel assessment of circulatory fetal DNA and corticotropin-releasing hormone mRNA in early-and late-onset preeclampsia. Clin Chem. 2005; 51(9): 1730-1733.
11. Han C, Han L, Huang P, Chen Y, Wang Y, Xue F. Syncytiotrophoblast-derived extracellular vesicles in pathophysiology of preeclampsia. Front Physiol. 2019; 10: 1236.
12. Palei AC, Granger JP, Tanus-Santos JE. Matrix metalloproteinases as drug targets in preeclampsia. Curr Drug Targets. 2013; 14(3): 325-334.
13. Rahat B, Sharma R, Bagga R, Hamid A, Kaur J. Imbalance between matrix metalloproteinases and their tissue inhibitors in preeclampsia and gestational trophoblastic diseases. Reproduction. 2016; 152(1): 11-22.
14. Palei AC, Sandrim VC, Amaral LM, Machado JS, Cavalli RC, Duarte G, et al. Association between matrix metalloproteinase (MMP)-2 polymorphisms and MMP-2 levels in hypertensive disorders of pregnancy. Exp Mol Pathol. 2012; 92(2): 217-221.
15. Espino Y, Sosa S, Flores-Pliego A, Espejel-Nuñez A, Medina-Bastidas D, Vadillo-Ortega F, et al. New insights into the role of matrix metalloproteinases in preeclampsia. Int J Mol Sci. 2017; 18(7): 1448.
16. Cabral-Pacheco GA, Garza-Veloz I, Castruita-De la Rosa C, Ramirez-Acuña JM, Perez-Romero BA, Guerrero-Rodriguez JF, et al. The roles of matrix metalloproteinases and their inhibitors in human diseases. Int J Mol Sci. 2020; 21(24): 9739.
17. Paiva P, Whitehead C, Saglam B, Palmer K, Tong S. Measurement of mRNA transcripts of very high placental expression in maternal blood as biomarkers of preeclampsia. J Clin Endocrinol Metab. 2011; 96(11): E1807-E1815.
18. Wu P, van den Berg C, Alfirevic Z, O'Brien S, Röthlisberger M, Baker PN, et al. Early pregnancy biomarkers in pre-eclampsia: a systematic review and meta-analysis. Int J Mol Sci. 2015; 16(9): 23035-23056.
19. Whitehead CL, Walker SP, Tong S. Measuring circulating placental RNAs to non-invasively assess the placental transcriptome and to predict pregnancy complications. Prenat Diagn. 2016; 36(11): 997-1008.
20. Arpino V, Brock M, Gill SE. The role of TIMPs in regulation of extracellular matrix proteolysis. Matrix Biol. 2015; 44-46: 247-254.
21. Mendes S, Timóteo-Ferreira F, Almeida H, Silva E. New insights into the process of placentation and the role of oxidative uterine microenvironment. Oxid Med Cell Longev. 2019; 2019: 9174521.
22. Tarca AL, Romero R, Erez O, Gudicha DW, Than NG, Benshalom-Tirosh N, et al. Maternal whole blood mRNA signatures identify women at risk of early preeclampsia: a longitudinal study. J Matern Fetal Neonatal Med. 2021; 34(21): 3463-3474.
23. Ashur-Fabian O, Yerushalmi GM, Mazaki-Tovi S, Steinberg DM, Goldshtein I, Yackobovitch-Gavan M, et al. Cell free expression of hif1α and p21 in maternal peripheral blood as a marker for preeclampsia and fetal growth restriction. PLoS One. 2012; 7(5): e37273.
24. Zhu J, Zhong M, Pang Z, Yu Y. Dysregulated expression of matrix metalloproteinases and their inhibitors may participate in the pathogenesis of pre-eclampsia and fetal growth restriction. Early Hum Dev. 2014; 90(10): 657-664
25. Xiang Y, Zhang X, Li Q, Xu J, Zhou X, Wang T, et al. Promoter hypomethylation of TIMP3 is associated with pre-eclampsia in a Chinese population. Mol Hum Reprod. 2013; 19(3): 153-159.
26. Sandrim V, Machado J, Tanus-Santos JE, Cavalli R. 41 Circulating level of TIMP-4 is elevated in preeclampsia: endothelial dysfunction, anti-angiogenic factors. Pregnancy Hypertension: An International Journal of Women's Cardiovascular Health. 2016; 6(3): 197.
27. Nikolov A, Popovski N, Hristova I. Collagenases MMP-1, MMP-13, and tissue inhibitors TIMP-1, TIMP-2: their role in healthy and complicated pregnancy and potential as preeclampsia biomarkers—a brief review. Appl Sci. 2020; 10(21): 1-13.
28. Tomimatsu T, Mimura K, Matsuzaki S, Endo M, Kumasawa K, Kimura T. Preeclampsia: maternal systemic vascular disorder caused by generalized endothelial dysfunction due to placental antiangiogenic factors. Int J Mol Sci. 2019; 20(17): 4246.
29. Zhang Y, Li P, Guo Y, Liu X, Zhang Y. MMP-9 and TIMP-1 in placenta of hypertensive disorder complicating pregnancy. Exp Ther Med. 2019; 18(1): 637-641.
30. Nissi R, Santala M, Talvensaari-Mattila A. The serum levels of circulating matrix metalloproteinase MMP-9, MMP-2/TIMP-2 complex and TIMP-1 do not change significantly during normal pregnancy: a pilot study. BMC Res Notes. 2021; 14(1): 31.
31. Seval Y, Akkoyunlu G, Demir R, Asar M. Distribution patterns of matrix metalloproteinase (MMP)-2 and-9 and their inhibitors (TIMP-1 and TIMP-2) in the human decidua during early pregnancy. Acta Histochem. 2004; 106(5): 353-362.
32. Nikolov A, Popovski N. Role of gelatinases MMP-2 and MMP-9 in healthy and complicated pregnancy and their future potential as preeclampsia biomarkers. Diagnostics (Basel). 2021; 11(3): 480.
33. Xie D, Zhu J, Liu Q, Li J, Song M, Wang K, et al. Dysregulation of HDAC9 represses trophoblast cell migration and invasion through TIMP3 activation in preeclampsia. Am J Hypertens. 2019; 32(5): 515-523.
34. Kuliczkowski W, Radomski M, Gąsior M, Urbaniak J, Kaczmarski J, Mysiak A, et al. MMP-2, MMP-9, and TIMP-4 and response to aspirin in diabetic and nondiabetic patients with stable coronary artery disease: a pilot study. BioMed Res Int. 2017; 2017: 9352015.
35. Masciantonio MG, Lee CKS, Arpino V, Mehta S, Gill SE. The balance between metalloproteinases and TIMPs: critical regulator of microvascular endothelial cell function in health and disease. Prog Mol Biol Transl Sci. 2017; 147: 101-131.
36. Majali-Martinez A, Hiden U, Ghaffari-Tabrizi-Wizsy N, Lang U, Desoye G, Dieber-Rotheneder M. Placental membrane-type metalloproteinases (MT-MMPs): key players in pregnancy. Cell Adh Migr. 2016; 10(1-2): 136-146.
37. Chen J, Khalil RA. Matrix metalloproteinases in normal pregnancy and preeclampsia. Prog Mol Biol Transl Sci. 2017; 148: 87-165.

Cell J
Cell Journal(Yakhteh) Homepage: https://www.celljournal.org/
Original Article Vol 25, No 1, January 2023, Pages: 51-61

The Synergistic Effect of Cold Atmospheric Plasma Mediated Gold Nanoparticles Conjugated with Indocyanine Green as An Innovative Approach to Cooperation with Radiotherapy

Sara Momeni, M.Sc.[1], Ahmad Shanei, Ph.D.[1]*, Ameneh Sazgarnia, Ph.D.[2]*, Neda Attaran, Ph.D.[3], Seyed Amir Aledavood, M.D.[4]

1. Department of Medical Physics, School of Medicine, Isfahan University of Medical Sciences, Isfahan, Iran
2. Medical Physics Research Center, Mashhad University of Medical Sciences, Mashhad, Iran
3. Department of Medical Nanotechnology, Science and Research Branch, Islamic Azad University, Tehran, Iran
4. Cancer Research Center, Faculty of Medicine, Mashhad University of Medical Sciences, Mashhad, Iran

**Corresponding Addresses: P.O.Box: 8174673461, Department of Medical Physics, School of Medicine, Isfahan University of Medical Sciences, Isfahan, Iran*
P.O.Box: 9177948564, Medical Physics Research Center, Mashhad University of Medical Sciences, Mashhad, Iran
Emails: Shanei@med.mui.ac.ir, sazgarniaa@mums.ac.ir

Received: 25/July/2022, Revised: 29/September/2022, Accepted: 29/October/2022

Abstract

Objective: The multimodality treatment of cancer provides a secure and effective approach to improve the outcome of treatments. Cold atmospheric plasma (CAP) has got attention because of selectively target and kills cancer cells. Likewise, gold nanoparticles (GNP) have been introduced as a radiosensitizer and drug delivery with high efficacy and low toxicity in cancer treatment. Conjugating GNP with indocyanine green (ICG) can develop a multifunctional drug to enhance radio and photosensitivity. The purpose of this study is to evaluate the anticancer effects of GNP@ICG in radiotherapy (RT) and CAP on DFW melanoma cancer and HFF fibroblast normal cell lines.

Materials and Methods: In this experimental study, the cells were irradiated to RT and CAP, alone and in combination with or without GNP@ICG at various time sequences between RT and CAP. Apoptosis Annexin V/PI, MTT, and colony formation assays evaluated the therapeutic effect. Finally, the index of synergism was calculated to compare the results.

Results: Most crucially, the cell viability assay showed that RT was less toxic to tumors and normal cells, but CAP showed a significant anti-tumor effect on melanoma cells with selective toxicity. In addition, cold plasma sensitized melanoma cells to radiotherapy so increasing treatment efficiency. This effect is enhanced with GNP@ICG. In comparison to RT alone, the data showed that combination treatment greatly decreased monolayer cell colonization and boosted apoptotic induction.

Conclusion: The results provide new insights into the development of better approaches in radiotherapy of melanoma cells assisted plasma and nanomedicine.

Keywords: Apoptosis, Cold Plasma, Indocyanine Green, Melanoma, Radiation Therapy

Citation: **Momeni S, Shanei A, Sazgarnia A, Attaran N, Aledavood SA. The synergistic effect of cold atmospheric plasma mediated gold nanoparticles conjugated with indocyanine green as an innovative approach to cooperation with radiotherapy. Cell J. 2023; 25(1): 51-61. doi: 10.22074/CELLJ.2022.559078.1097.**

Introduction

Cancer is a significant burden of disease on a global scale. Melanoma, a malignant tumor originating from melanocytes, is a rare disease and the most deadly type of skin cancers (1). Despite the fact that surgery is the main treatment option, radiotherapy (RT) is sometimes required for tumor size reduction, adjuvant therapy postoperatively, and lymph node or brain metastasis. Thus, a great number of studies have been conducted in an attempt to increase the sensitivity of radiotherapy-resistant cells and reduce side effects (2).

Photodynamic therapy (PDT) is a new therapeutic method with Food and Drug Administration (FDA) approval used to treat superficial tumors, such as skin cancer (3, 4). PDT uses a particular drug called photosensitizer along with light to cause oxygen-dependent destruction of cancer cells. Although they are not individually toxic, photochemical reactions produce highly reactive products called singlet oxygen ($^1O_2$), which can rapidly cause cell death via apoptosis and necrosis (5). However, PDT as an adjunct therapy offers several benefits, there are some limitations about PDT such as hypoxia induction due to oxygen consumption and vascular damage, not being tumor-specific method and etc. (6, 7).

The ionized plasma known as cold atmospheric plasma (CAP) may be employed as a new light source for PDT. CAP is an ionized gas contains electrons, ions, free radicals, reactive oxygen (ROS) and nitrogen species (RNS), and UV photons that exists at low temperatures. At atmospheric pressure, plasma is created by using a high voltage electric field (8). Because CAP is a potent generator of ROS, it may help to reduce some problems related to PDT and increase therapeutic effectiveness (9). In general, plasma is classified into two types: thermal plasma and non-thermal or cold plasma. In the past, only the thermal properties of plasma had biomedical uses in ablation, tissue cutting, and blood coagulation.

Recent research into the medical applications of CAP has revealed new areas of medical research. Some of the medical applications of CAP include wound healing (10), sterilization of medical devices , and induction of blood clotting during surgery (11). The anti-cancer effects of CAP were studied in various types of cancer, *in vitro* (12) and *in vivo* (13). The most noticeable feature of CAP is the ability to kill cancer cells selectively and protect healthy cells (14). Although the mechanism of contact between plasma and cell is not fully known, ROS seems to play a critical role in this process (15). More ROS diffuses into tumor cells because they have more AQPs (an aquatic channel that increases ROS diffusion through transmembrane) and more cholesterol in their cellular membrane than normal cells, resulting in higher oxidative balance disruption (16). Normal cells, on the other hand, are better at dealing with this disruption than tumor cells (17). The studies proposed various mechanisms of CAP effects containing oxidative stress, ROS generation and subsequently DNA double strands break (DSB), cell cycle arrest, activation of *p53* gene, and activation of p21 CKS inhibitor, necrosis, cell detachment and apoptosis via plasma-generated ROS (18-20).

Cancer treatment with integration of CAP and nanoparticles has shown to be lucrative. Gold nanoparticles (GNP) exhibit unique qualities among nanoparticles, including low toxicity, tumor-specific drug transporters, radiosensitizers, and changeable absorption peak from ultra-violet to infrared depending on particle shape and size (21). The benefits of cancer treatment with CAP and GNP are most likely ascribable to their more selectivity, rise in nanoparticles uptake, and better treatment efficiency (22, 23). Indocyanine green (ICG) is a low toxic amphilic dye with Food and Drug Administration (FDA) approval used for cancerous photothermal and PDT (24). ICG shows high absorbance in the treatment window (650-850 nm) where maximum light transmission to the tissue occurs that is not absorbed by the melanin of the skin or melanoma cells. It can be used as a photosensitizer along with GNP to evaluate the photodynamic effects evoked by CAP.

The impacts of combined radiation therapy (RT) with CAP were reported in some research. However, no study has been performed to investigate the composition of CAP as a pre-treatment of RT in the presence of a photo-radio sensitizer, with the hypothesis that it can amplify the radiation as well as photodynamic effects produced by the plasma. Besides, the point that is less considered in combination therapies is the sequence of treatments and its effect on the final result. It has generally been proven that different treatments can stop the cell cycle. Therefore, applying a treatment that stops the cells in the radiation-sensitive phase, followed by RT, increases the effectiveness of the treatment.

Hence, we evaluated new technique for treating melanoma cells *in vitro*. The radiosensitizing effect mediated by plasma-induced PDT in the presence of GNP@ICG on the DFW human melanoma cell line and HFF normal fibroblast cell line is the main aim of this study. In this case, GNP@ICG NPs were initially synthesized and their photophysical characteristics studied. Second, the effectiveness of GNP@ICG in PDT caused by CAP treatment on cancer and normal cells, as well as its selectivity, were assessed. Third, the radio-sensitization impact of GNP@ICG was investigated at various dosages. Fourth, treatments were carried out at 0 and 24 hours intervals to identify the optimal time between CAP and RT. Finally, the mechanism of death in combination therapy and each treatment alone was evaluated by flow cytometry to diagnose apoptosis.

Materials and Methods

Ethics approval for the current experimental study was given by the Ethics Committee at Isfahan University of Medical Sciences under a project number of IR.MUI.MED.REC.1399.947. Gold (III) chloride hydrate (99.995 %) was acquired by Alfa Asear (254169, USA). Fetal bovine serum (FBS) was acquired by Gibco (F7524, USA). ICG (228869) and dimethyl sulfoxide (DMSO, D8418) were acquired by Merck (Germany). Trisodium citrate dehydrate (6132-04-3), Roswell Park Memorial Institute (RPMI-1640, 51800-035) cell culture medium, Dulbeccos Modified Eagles Medium (DMEM, D6429), penicillin-streptomycin (P4333), trypsin-ethylene diamine tetra acetic acid (EDTA, 60-00-4), and 3–(4,5dimethylthiazol-2-yl)-2,5-diphenyltetrazolium bromide (MTT,TOX1) were acquired by Sigma-Aldrich Company (St. Louis, MO, USA). Apoptosis Detection Kit [Annexin V labeled with FITC/Propidium Iodide (PI)] was purchased from BD Biosciences (AB_2869082, USA).

Synthesis and physical characterization

GNP and GNP@ICG synthesis

GNP@ICG nanoparticles were synthesized in a two-step process. First step: GNP were synthesized as stated in Anshup et al. (25). All glassware was scrubbed with a 3:1 solution of HCl and HNO_3, after that washed with distilled water and drained. A solution containing HAuCl4 (5 ml, 0.2% w/w) and deionized water (90 ml) was refluxed under constant and vigorous stirring. When the solution reached boiling point, sodium citrate trihydrate (5 ml, 1% w/w) was rapidly infused into the HAuCl4 solution. The molar ratio of sodium citrate trihydrate to HAuCl4 was a major controlling factor in achieving the desired particle size. After changing the color from pale yellow to red, the solution was remained for 15 minutes. GNP produced were purified by centrifugation and repeated precipitation from distilled water. Second step: To conjugate ICG on the GNP surface, we added an aqueous solution of ICG (10 ml, 80 mg/L) to the GNP preparation solution (10 ml, 100 mg/L) and at room temperature stirred for 3 hours. After the completion time, the particles were centrifuged and precipitated twice from distilled water to give purified GNP@ICG nanoparticles.

Characterization of GNP and GNP@ICG

Particle size, size distribution, and polydispersity index (PDI) for GNP and GNP@ICG were obtained using the Malvern Zetasizer (Zetasizer, Malvern Ins., USA). To assess the stability of GNP and GNP@ICG, we performed dynamic light scattering (DLS) analysis of NPs at different time points. For this purpose, 125 µl of GNP and 90 µl of GNP@ICG were added to 875 and 910 µl of 10% fetal bovine serum (FBS) supplemented culture medium, respectively and DLS analysis was performed immediately and then 48 hours later. The results were compared to each other.

The optical properties of the GNP@ICG were recorded in the wavelength range of 300–1000 nm using UV-visible spectroscopy (UV 1700, Shimadzu Corp, Japan). The morphology of the GNP@ICG was determined using a scanning electron microscope (FE-SEM LMU TESCAN BRNO-Mira3, Czech Republic), operating at an acceleration voltage of 26 kV. TEM (Gatan model 791, Philips CM 12, Poland) was carried out to evaluate the morphology and size distribution of the GNPs. Infrared spectra were recorded with an FTIR spectrometer (AVATAR 370, Thermo Nicolet AVATAR 370 FTIR, USA) to investigate possible chemical interactions between ICG and GNP@ICG. X-ray diffraction (XRD) analysis (Bruker 9XS; G8ADVANCE, Germany) was performed to identify the crystallographic structure of GNP. Measurements were performed at voltage 40 kV and current 30 mA over the 2θ range of 20° to 80°.

Cell studies

Cell culture

DFW (human melanoma cell line, C496) and HFF (normal human foreskin fibroblast cell line, C163) were purchased from Pasteur Institute in Iran. DFW was cultured in RPMI-1640, and HFF was cultured in DMEM. All media were supplemented with 10% FBS and 0.5% penicillin-streptomycin. The cells were kept in a humidified incubator with a temperature of 37˚C and 5% CO_2. They were separated for passage using 0.25% trypsin-EDTA.

Cytotoxicity

To assess the toxicity of GNP@ICG on DFW and HFF cell lines, they were seeded in 96-well plates at densities of 10,000 and 7,000 cells/well, respectively, and incubated at 37˚C and 5% CO_2 for one day. The cells were probed for 24 hours at various concentrations (0-80 mg/L) of GNP@ICG added to the medium. Subsequently, to remove extra nanoparticles, the cells were rinsed with phosphate buffered saline (PBS) three times. Finally, the cell viability was analyzed by MTT assay after 24 hours.

Experimental treatments

The plasma device used in this study is a plasma jet (Satia knowledge based company; Semnan, Iran) consisting of two electrodes, A carbon center electrode connected to a high voltage power supply and a copper ground electrode attached to the ground. In this study, a high voltage power with a frequency of 13 kHz and a peak-to-peak voltage of 5 kV was given to the electrodes. Pure helium gas (99.999%) was also used to generate the plasma at a flow rate of 4-5 L/minutes. The length range of the plasma flame was set to 35-45 mm and the distance between the nozzle tip and the bottom plate was set to 25 mm. The gas temperature of the plasma jet was measured at 350 K. The biomedical application of CAP is primarily based on its ability to produce and form effective amounts of reactive species. Emission spectroscopy (OES) was used to confirm the presence of these species and their derivatives.

The cells were radiated with 8 MeV electron irradiation (linear accelerator Elekta Precise model, Germany) at a dose rate of 2 Gy/minutes with distance of 100 cm from the X-ray tube and gantry at 180 degrees position. Field dimensions were adjusted by using a 20*20 cm applicator and Perspex plates were used to set the build-up before the cells (15 mm thickness under the plate) as well as to remove the scatters from the plate (20 mm thickness on the plate). RT was performed at 1, 2, and 4 Gy.

Treatment groups consist of the following without and with 20 mg/L GNP@ICG (based on the cytotoxicity of GNP@ICG) for both cell lines: the control group (C), the plasma treatment groups (CAP and GNP@ICG+CAP), the radiotherapy groups (RT and GNP@ICG+RT), and the combined radiotherapy and plasma therapy groups (GNP@ICG+CAP+RT at various intervals 0 and 24 hours).

For all treatment groups, DFW and HFF cells were first seeded on 96 well plates and incubated overnight. Next, GNP@ICG (20 mg/L GNP@ICG containing 16 mg/L ICG and 20 mg/L GNP) was added to the cells. At the end of the incubation period, the cell plates were rinsed twice with PBS and replaced with a fresh medium. Afterward, in plasma treatment groups, the cell plates were treated with CAP at room temperature for different times (0, 15, 30, 60, and 90 seconds). In radiation therapy, cells irradiated with 8 MeV electron at various doses of 1, 2, and 4 Gy. To assess the efficacy of combined RT with CAP, the cells were first treated with CAP for 30 and 60 seconds, then irradiated with 2 Gy dose of radiation immediately and after 24 hours.

Evaluation of treatments

MTT assay

The MTT assay was used to identify the cytotoxicity of GNP@ICG and the effects of plasma and radiation therapy to find optimal concentrations of GNP@ICG and appropriate doses of RT and CAP, respectively. In this regard, the cells were assessed 24 hours after the end of treatments. Briefly, 100 µl of FBS-free medium

and 10 µl of MTT reagent (5 mg/mL in PBS) were added to all wells and incubated for 4 hours in the darkness. This test is based on the measurement of cell viability in terms of reducing activity as an enzymatic conversion of the tetrazolium to water-insoluble formazan crystals by dehydrogenase activity generated in the mitochondria of living cells. After that, the medium was removed and then for dissolving the formazan crystals, 200 µl of DMSO replaced. At the end, plates were shaken in the dark for 10 minutes. An ELIZA reader was used to measure the absorbance of the formazan solution at a wavelength of 570 nm as opposed to the reference wavelength of 630 nm. Finally, the relative cell viability rate was calculated by the absorbance ratio of the treatment group to the control group. All examinations were repeated more than three times.

Flow cytometry

To measure apoptosis and necrosis of cells treated with RT and CAP using the Annexin V-FITC/ PI flow cytometry kit, firstly, the cells were treated, incubated for 24 hours, rinsed with PBS, separated with trypsin, centrifuged at 1500 rpm for 5 minutes, then combined with the binding buffer. FITC-labeled Annexin V (2 µl) and PI (2 µl) were added to and pooled in 500 µl cell suspension. After 15 minutes of incubation in the dark, apoptosis/necrosis analysis was performed by flow cytometry (BD FACSCalibur, USA), and the data were analyzed by FlowJo software (version 7.6.1).

Colony formation assay

The colony formation assay (CFA) was accomplished to assess the ability of cells to develop as colonies after treatment. The cells were seeded in 6-well plates at a density of 600, 800, 1000, and 1200 cells/well for the control group, and a radiation dose of 1, 2, and 4 Gy. Following cell adhesion, they were treated in various groups according to the method described above. The groups contained control, GNP@ICG+RT, and GNP@ICG+CAP (60 seconds)+RT at 0 and 24 hours intervals. Then, colonies were allowed to form after 10 days of incubation. Finally, colonies were rinsed, fixed and stained with PBS, methanol, and Giemsa, respectively. It was calculated only colonies including more than 50 cells. The surviving fraction (SF) of each group was normalized to the plating efficiency (PE) associated to the control group. The SF was calculated by the below formula (26):

Plate efficiency (PE) = (number of colonies in the control group)/ (number of cultured cells)

Cell survival fraction = (number of colonies in the experimental group) / (number of cells in the experimental group × PE)

Synergistic index

We have defined a synergistic index (Syn) to determine if synergistic or additive effects have occurred in cell death (CD) caused by combined therapy including GNP@ICG+CAP+RT compared to CD of either treatment alone without interval (Syn.1) and 24 hours intervals (Syn.2) on melanoma and fibroblast cells.

Syn (1) = (CD (CAP + GNP@ICG + RT (2Gy)) 0 h) / (CD(CAP) + CD (GNP@ICG) + RT(2Gy))

Syn (2) = (CD (CAP + GNP@ICG +RT (2Gy)) 24 h) / (CD(CAP)+ CD (GNP@ICG) + RT(2Gy))

Statistical analysis

The results were completed by repeating the tests three times and stated as mean values ± standard deviation (SD). The Kolmogorov-Smirnov nonparametric test was used to assess the normality of the data. We ran a one-way ANOVA followed by Tukey's tests to compare the mean differences. P-values below 0.05 were regarded as statistically significant.

Results

Characterization of synthetic nanoparticles

The size distribution of GNP and GNP@ICG were measured by DLS analysis. The hydrodynamic diameter of GNP and GNP@ICG is 24.3 and 31.5 nm, respectively. The Zeta potential of GNP and GNP@ICG were -1.5 and -7.8 mV, which was engaged to validate the excellent reaction. According to the results, the zeta potential of GNP@ICG is higher negative than GNPs. This finding is that the SO_3^- group in the ICG induces a negative charge on the surface of NPs. By comparing the hydrodynamic size of the NPs based on the DLS results, it was observed that the size of the nanoparticles did not change after 48 hours, indicating good stability of the nanoparticles (Fig.S1, See Supplementary Online Information at www.celljournal.org).

Figure 1A shows the UV-Vis spectra of GNP, ICG, and GNP@ICG. UV-Vis spectrometry was employed to characterize the synthesized conjugated NPs. It is clear that the spectrum of the GNP shows the dispersion of GNP. The absorption spectrum of ICG shows strong absorption in 700-780 nm depending on the ICG concentration. GNP shows characteristic surface absorption at 520 nm, confirming that the GNP are spherical. In addition, GNP@ICG shows peaks at 520, 709, and 778 nm, indicating the presence of GNP and ICG in the conjugated nanoparticles. For surface analysis of the synthesized nanoparticles and compared with free ICG, the FT-IR spectra were obtained from dried GNP@ICG and ICG (Fig.1B). According to FT-IR spectra of ICG, the absorption bands around 3430 cm^{-1}, 1400 cm^{-1}, 1090 cm^{-1}, and 891 cm^{-1} can be assigned to O-H stretching vibration, SO_3H and C=C bond, sulfoxide, and C-H ring bending vibration, respectively, exhibiting the characteristic peaks of ICG. According to GNP@ICG, the characteristic peak at 1410 and 1590 cm^{-1} correspond to the symmetric and anti-symmetric stretching of COO^- related to citrate ion. These data confirm the interaction between citrate ions and GNP. In addition, the existence of absorption peaks of ICG (3430, 1400, 1090, and 891 cm^{-1}) in the IR spectrum of GNP@ICG can confirm that ICG was successfully conjugated on the GNP surface.

SEM images of GNP and GNP@ICG and their size distribution histogram obtained by ImageJ software are shown in Figure 1C-F. It can be observed that the nanoparticles are spherical shape with average diameters of 19.49 and 24 nm, respectively. Also, as shown in Figure 1G. The spherical structure of GNP can be observed clearly in the TEM image. The shape and mean diameter of GNP evaluated by TEM imaging (around 20 nm) were correlated to FE-SEM and DLS measurements. The XRD pattern of GNP is shown in Figure 1H. Crystalline nanoparticles structure specified through four peaks corresponding to standard Bragg reflections (111), (200), (220), and (311) of face centers cubic lattice. The intense peak at 38, 44.3, 64.5, and 77.7 nm determines preferential growth in the (111, 200, 220, and 311) direction.

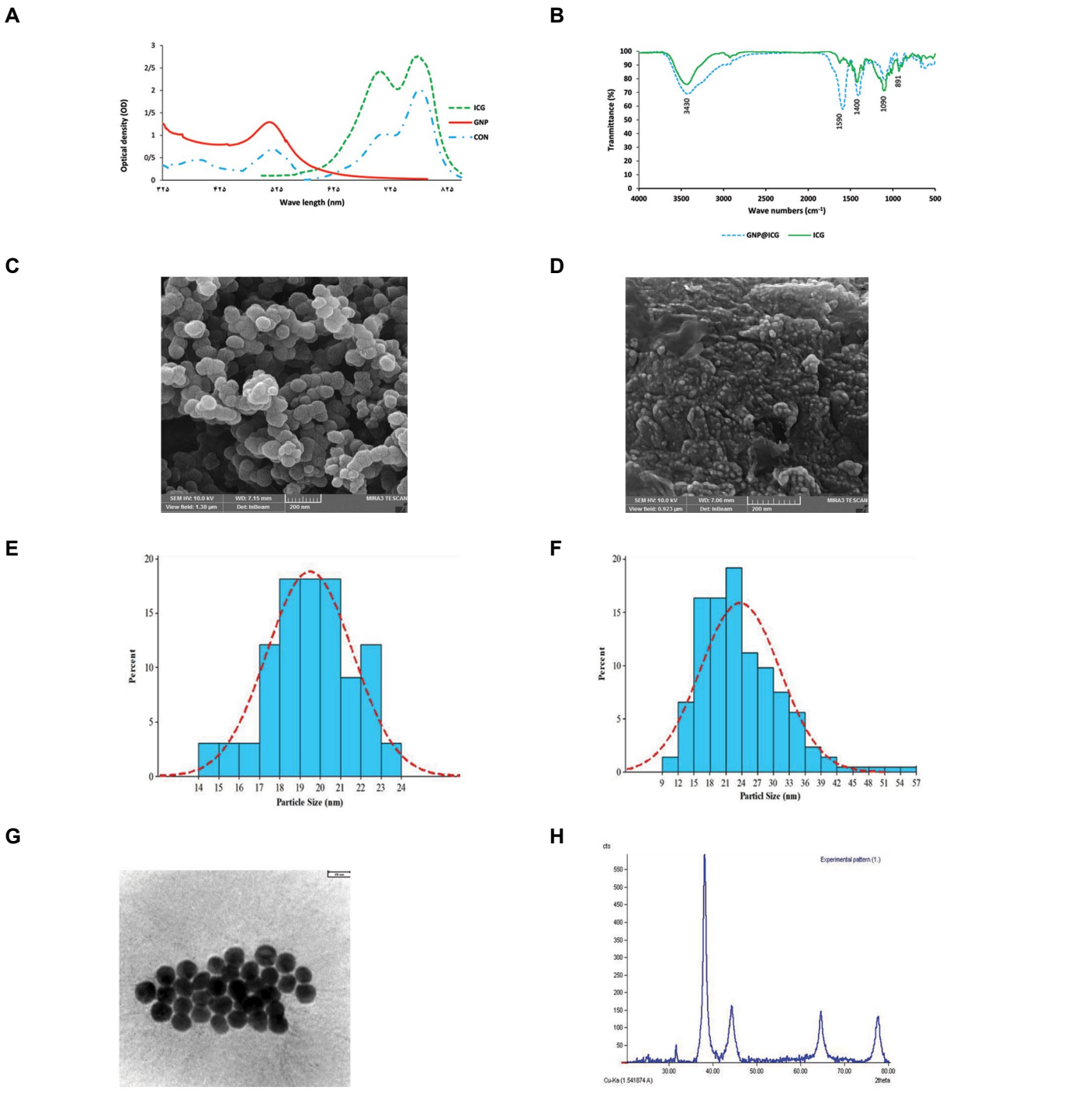

Fig.1: The specifications of synthesized nanoparticles. **A.** The UV-visible spectrum of GNP (20 mg/L), ICG (16 mg/L) and GNP@ICG (20 mg/L based on the concentration of GNP), **B.** The FT-IR spectra of GNP@ICG (20 mg/L based on the concentration of GNP) and free ICG (16 mg/L), **C.** Field Emission Scanning Electron Microscopy (FE-SEM) images of GNP (scale bar: 200 nm), **D.** FE-SEM images of GNP@ICG (scale bar: 200 nm), **E.** Hydrodynamic size distribution of GNP, **F.** Hydrodynamic size distribution of GNP@ICG, **G.** TEM image of the gold nanoparticle (scale bar: 20 nm), and **H.** XRD analysis of gold nanoparticles. GNP; Gold Nanoparticles, ICG; Indocyanine green, FT-IR; Fourier transform infrared spectroscopy, TEM; Transmission electron microscopy, and XRD; X-Ray diffraction analysis.

Spectroscopy analysis

The emission spectrum of CAP was obtained by spectroscopic analysis (Fig.2A). Figure 2B displays a schematic illustration of the CAP device used in this experiment. As shown in Figures 1A and 3, the absorption spectrum of the ICG is superimposed on the emission spectrum of the CAP. The most prominent emission peaks for CAP include 320, 330, 350, 391, 400, 460, and 707 nm. As one can see, the absorption peak of ICG at wavelengths 710 to 780 corresponds to the emission spectrum of the He-CAP.

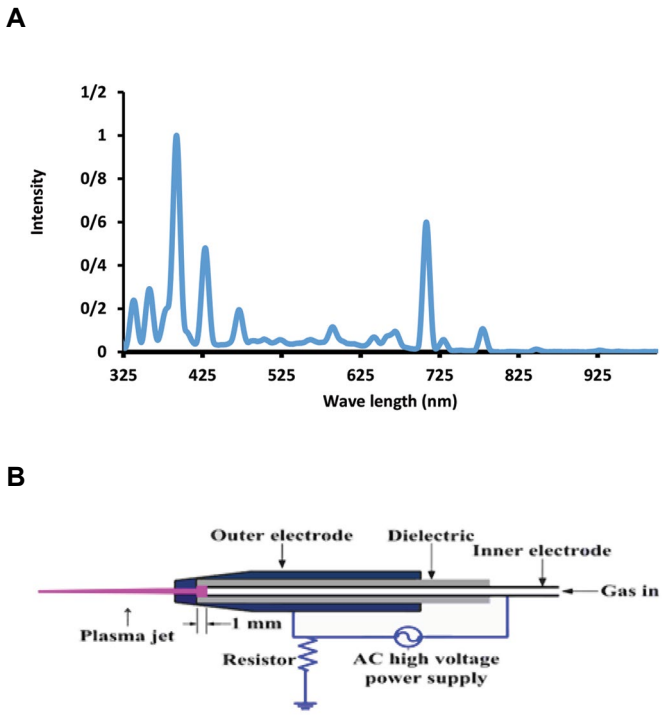

Fig.2: The characterization of CAP. **A.** The emission spectrum of CAP-He and **B.** Schematic illustration of the plasma jet. CAP-He; Cold Atmospheric helium plasma and AC; Alternating current.

MTT assay

To select an optimal concentration of GNP@ICG NPs and evaluate CAP treatment and radiation therapy, the MTT assay was carried out to measure the metabolic viability of DFW (cancer cells) and HFF (normal cells) in different treatment groups. After incubating cells with varied concentrations of GNP@ICG (0-80 mg/L) for 24 hours, it was shown that concentrations of GNP@ICG less than 20 mg/L had only a slight effect on both cells. It was concluded that 80 mg/L was the most toxic and killed nearly 51% and 72% of the melanoma and fibroblast populations, respectively (Fig.3A). The low toxic concentration of GNP@ICG (20 mg/L of GNP@ICG containing 16 mg/L ICG and 20 mg/L GNP) was used to evaluate the inhibition of cells proliferation in RT, CAP, and combined therapy groups. Treatments were performed as described in Material and Methods.

The RT results (Fig.3B) shows the radiation resistance of melanoma cells. Moreover, in both cells a significant difference was observed between RT and GNP@ICG+RT groups ($P<0.05$), which indicates the role of GNP@ICG as a radio-sensitizer.

Figure 3C shows the cell viability of DFW melanoma cells at different times of plasma irradiation as well as incubation with GNP@ICG. However, cell survival at 15 seconds treatment with CAP had no effect on cells, with increasing plasma irradiation time, cell survival percentage decreased significantly, so that in the 90-second group in the presence of GNP@ICG, the survival percentage reached 14% ($P<0.01$). Also, cell survival in plasma therapy with GNP@ICG was significantly reduced compared to the drug-free group, which can confirm the GNP@ICG optical sensitivity in PDT with CAP. In order to determine whether plasma therapy is selective for cancer cell lines, HFF cells were treated under similar conditions. The results showed that increasing the plasma time had no effect on the survival of HFF cells. The results were the same even in the treatment group that received GNP@ICG.

Based on these findings, doses of 30 and 60 seconds for CAP therapy and 2 Gy for RT were selected for irradiation in subsequent experiments. Synergistic enhancement was observed in DFW cells treated with combination therapy in a dose-dependent manner compared to either the control group or each modality alone. This means that pre-treated with CAP before RT promoted radiation effects on tumor cell death and amplified influence at higher doses. In contrast, no significant difference was measured between these groups for the HFF cell line ($P>0.05$). It is worth noting that plasma plays a crucial part in combining radiation therapy with CAP for a selective and effective therapy.

To evaluate the effect of interval in combined therapy, cells were exposed to RT immediately and 24 hours following CAP therapy. It was found that administration of RT 24 hours after CAP therapy can induce more cell death in DFW cells than the employment of these modalities immediately, whereas this discrepancy was not observed in HFF cells (Fig.3D).

Flow cytometry

Flow cytometric assays were used to evalute the induction of apoptosis and necrosis in various treatments of melanoma and fibroblast cell lines. The degree of apoptosis induction was quantified by Annexin V-FITC/PI staining. The flow cytometry experiment indicated a distribution pattern of cells treated with GNP@ICG, CAP, and RT alone and in combination treatment (GNP@ICG+CAP+RT) in sequences of 0 and 24 hours in Figure 4. As seen in Figure 4A, in melanoma cells, the percentage of apoptosis in combination RT with GNP@ICG was not significantly different from RT alone. While this difference made a significant difference in the treatment of CAP with GNP@ICG. In addition, the apoptosis rate was measured the highest amount in the combinatorial treatment group (GNP@ICG+RT+CAP), and it was established that the intervals between treatments did not induce apoptosis ($P<0.05$). We also evaluated the therapeutic effect on fibroblast (HFF) cell lines (Fig.4C). HFF cells were treated similarly to melanoma treatment. It was shown that RT, CAP, or combined CAP with RT did not induce significant apoptosis in fibroblast cells ($P>0.05$).

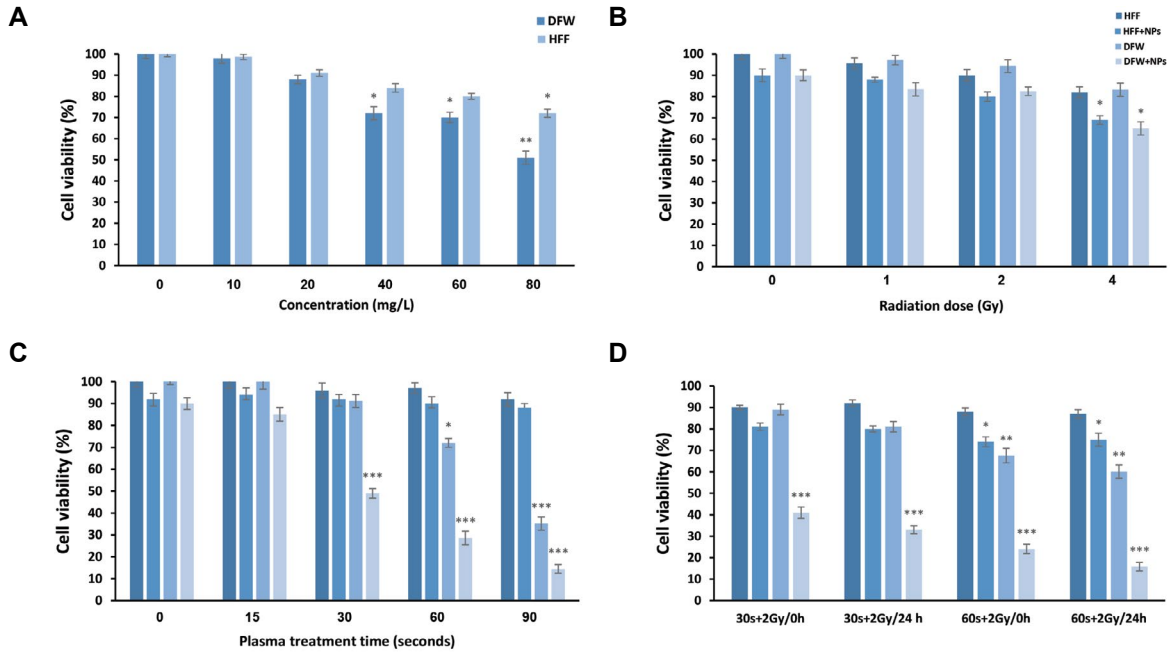

Fig.3: MTT assay results on melanoma (DFW) and fibroblast (HFF) cell lines at 24 hours. **A.** The survival rate of DFW and HFF cells incubated with different concentrations of GNP@ICG in 24 hours. The concentration of 10 µM which caused 10% cell death was selected for following treatments. **B.** The survival percentage of cells treated with radiotherapy. **C.** The survival percentage of cells treated with CAP. **D.** The viability of the cells treated to 2 Gy RT following NPs and CAP (30 and 60 seconds) immediately and 24 hours later. Data are shown as the mean ± SD (n=3). A comparison of the difference between each group and the control group was presented as *; P<0.05, **; P<0.01, and ***; P<0.001. CAP; Cold atmospheric plasma, NPs; GNP@ICG, RT; Radiotherapy, 30s+2Gy/0h; Combined therapy 30-seconds CAP and 2 Gy radiation immediately, 30s+2Gy/24h; Ccombined therapy 30-seconds CAP and 2 Gy radiation with 24 hours interval, 60 s+2Gy/0h; Combined therapy 60-seconds CAP and 2 Gy radiation immediately, and 60s+2Gy/24h; Combined therapy 60-seconds CAP and 2 Gy radiation with 24 hours interval.

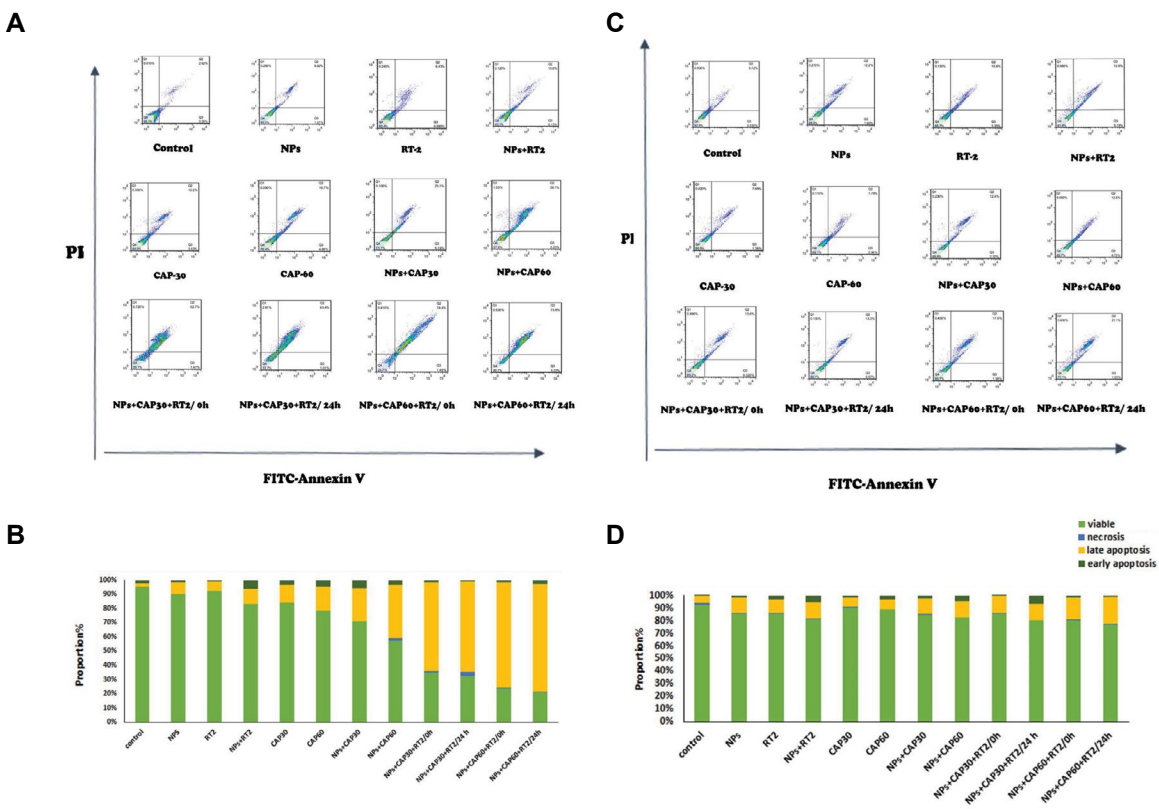

Fig.4: Flow cytometry results of DFW and HFF cell lines. **A.** The Annexin-V-FITC assay for detecting the apoptosis and necrosis of DFW cells, **B.** The diagram of the percentage of apoptotic and necrotic of DFW cells after treatment with different groups, **C.** The Annexin-V-FITC assay for detecting the apoptosis and necrosis of HFF cells, and **D.** The diagram of percentage of apoptotic and necrotic of HFF cells in different groups. DFW; Melanoma cell line, HFF; Health foreskin fibroblast, CAP; Cold atmospheric plasma, NPs; GNP@ICG, RT; Radiotherapy, 30s+2Gy/0h; Combined therapy 30-seconds CAP and 2 Gy radiation immediately, 30s+2Gy/24h; Ccombined therapy 30-seconds CAP and 2 Gy radiation with 24 hours interval, 60 s+2Gy/0h; Combined therapy 60-seconds CAP and 2 Gy radiation immediately, and 60s+2Gy/24h; Combined therapy 60-seconds CAP and 2 Gy radiation with 24 hours interval.

Colony formation assay

CFA was used to measure the ability of cells to maintain reproductive integrity over a long time after various treatments. CFA is the gold standard to identify reproductive cell death after ionizing radiation therapy. Figure 5 shows the effects of GNP@ICG and CAP (60 seconds) in different intervals and radiation doses on DFW melanoma cell lines in monolayer cultures. As can be concluded from the results, GNP@ICG alone had no significant effect on cell colonization compared to the control group ($P>0.05$). In the associated combined therapy, the reduction in SF was considerably more significant than in the control group receiving RT alone ($P<0.05$), which confirmed that CAP and GNP@ICG reduced radiation-induced clonogenic melanoma cell death in a dose-dependent manner. As can be seen in Figure 5A, in the combined treatment, the number of colonies and their size has decreased with increasing radiation dose, which indicates a decrease in the ability of cells to form colonies. The considerable difference between the combined treatment and control groups demonstrated that CAP plays a function in cancer cell synergy and radio-sensitivity. Furthermore, while combination treatment had the lowest cell viability, the gap between them did not produce significant effects, confirming the findings of the apoptosis experiment.

Synergistic index

The values of synergism index for combine therapy GNP@ICG+CAP+RT at 0 and 24 h intervals on melanoma and fibroblast cells were calculated in accordance with Formula. The synergistic indices were calculated more than 1 on melanoma cells (2.18 ± 0.02 and 1.65 ± 0.02 for 30 and 60 seconds, respectively treatment with CAP and 2 Gy radiotherapy immediately, and also 2.48 ± 0.03 and 1.82 ± 0.02 for 2 Gy radiotherapy following 30 and 60 seconds, respectively plasma treatment after 24 hours) which shows proposed treatment approaches had the synergistic effects. However, the synergistic index was calculated lower than 1 in all treatment groups on fibroblast cells.

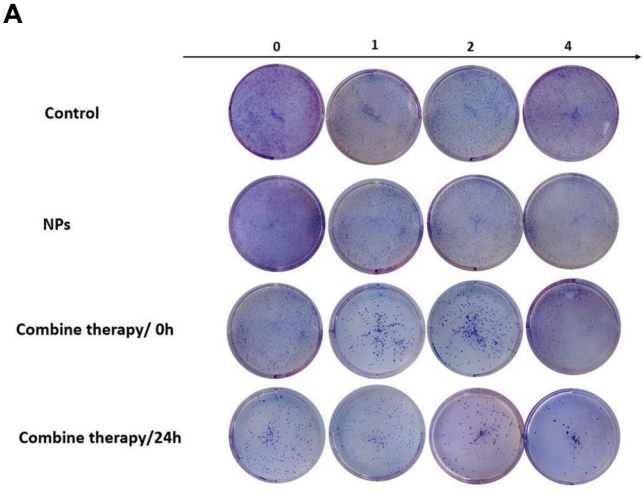

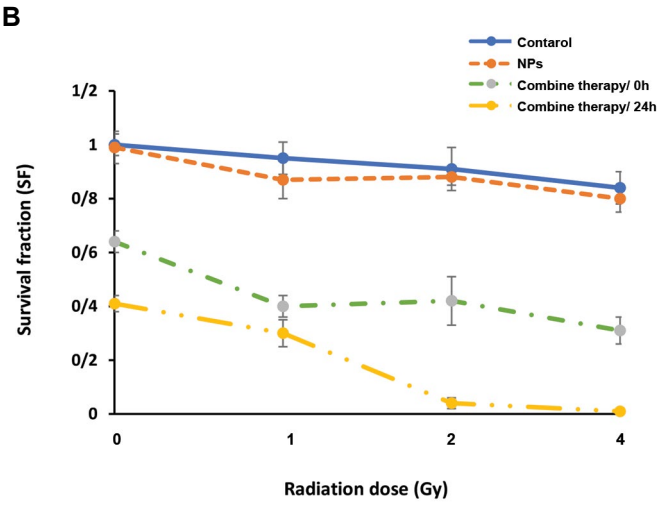

Fig.5: The treatment results via colony assay for DFW cells. **A.** The representative colony formation images of DFW cells in different treatments. **B.** Clonogenic cell survival curves. The surviving fraction in the colony-forming assay was calculated and normalized to that of the unirradiated control cells. Data were obtained from three independent experiments (mean ± SD, n=3). NPs; Gold nanoparticle conjugated with Indocyanine green, Combine therapy/0 hour; Treatment with 2 Gy radiotherapy immediately after 60 seconds cold plasma therapy, and Combine therapy/24 hours: treatment with 2 Gy radiotherapy 24 hours after 60 seconds cold plasma therapy.

Discussion

Melanoma accounts for just around 1% of all skin malignancies, yet it is responsible for the majority of mortality (1). Melanoma is difficult to treat because to its aggressive nature, resistance to established cancer therapies such as radiation therapy and chemotherapy, and poor response (2). Therefore, a new antitumor strategy is needed in this area. We have proposed an effective strategy for the DFW cell line derived from skin cancer to improve its radiation sensitivity and treatment efficiency.

CAP is a pioneering approach in cancer therapy. CAP contains different elements such as electrons, free radicals, charged particles, UV photons, and various excited molecules. The existence of different ingredients in plasma composition resulted in unique properties. For example, CAP is a potent generator of reactive oxygen species (ROS), which may be exploited to sensitize hypoxic malignancies to therapies (27). During plasma treatment, plasma introduces ROS into cells, disrupting oxidative equilibrium. By activating intracellular signaling pathways, excessive oxidative stress might lead to cell death (28). Moreover, CAP has several peaks in the emission spectra, so it is possible to use types of photosensitizers in CAP therapy. In addition, the difference between the cell membrane electric field and the CAP-induced transient electric field opens channels and increases the number of nanoparticles absorbed, resulting in improving processing efficiency (16).

Nanoparticles are being used in cancer treatment to take a more tailored approach. We created a novel conjugation that may be employed as a photo-radio-sensitizer to

improve treatment efficiency in this investigation. GNP have risen to the top of the list of metal nanoparticles used in bioanalytical studies. In this respect, gold nanospheres were successfully synthesized and conjugated with ICG as a photosensitizer. The results of photophysical properties analysis further confirmed that ICG could be conjugated by GNP. The existence of the characteristic absorption peak of ICG in the IR spectrum of GNP@ICG can confirm that ICG was successfully conjugated on the GNP surface. The size of GNP@ICG measured by DLS, TEM, and SEM was approximately 20 nm. Size 10-100 nm for GNP@ICG has been approved that is a suitable size to easily enter cells and increase uptake. The zeta potential calculated a good negative charge and confirmed the stability of GNP@ICG.

Due to the fact that RT for melanoma patients is performed with electrons as well as the advantages of electrons over photons (29) in this superficial tumor, we used electrons instead of photons in this study. MTT assay measured a considerable decrease in viability in treatment with radiation and GNP@ICG (20 mg/L). Since several studies have reported the radiosensitizing effect of GNP (30, 31) and Sazgarnia et al. (32) showed a low radiosensitizing effect of ICG, it is understood that the decrease in the cell viability measured is in terms of GNP in treatment.

In CAP therapy, according to the cell survival results after different treatment time, it can be found that plasma causes a notable inhibitory effect on DFW cells. The enhanced treatment efficacy by CAP was significantly improved in the presence of GNP@ICG, possibly in terms of the more absorption of GNP@ICG into cells following treatment with plasma. Our findings are in agreement with Zhu' research (4) observed that the combination of fluorouracil-loaded PLGA nanoparticles and CAP has enhanced efficacy for solid tumors treatment that inhibits synergistically cancer cell growth when compared individually. They also found that CAP promotes nanoparticle absorption while also lowering MMP2, MMP9, MTDH, and VEGF gene expression, all of which are linked to metastasis. Another explanation for plasma therapy's great effectiveness might be the photodynamic impact caused by ICG. Several studies have used different photosensitizers in CAP and evaluated the photodynamic effects of CAP on a variety of tumors. Karami used 5-ALA as a photosensitizer and observed the synergistic effect of CAP (33) and Wang et al. (34) treated melanoma cells with protoporphyrin IX and CAP. In a similar study, Vejdani Noghreiyan et al. (35) evaluated the PDT effects of CAP on ICG and PpIX at various concentrations (5-50 μM). The cells (HT-29 and MCF-7) were treated with CAP in 1 and 2 minutes irradiation. Results showed increased effectiveness of plasma treatment in the presence of ICG and PPIX. Furthermore, this effect was found to be cell line dependent.

The superiority of CAP over other treatment modalities is the ability of plasma to kill cancer cells selectively, while its effect on healthy cells is negligible. To evaluate the selectivity effect in CAP therapy, HFF cells were treated in conditions similar to DFW cells. Comparing the viability of the two cell lines showed that DFW cells were substantially more susceptible to plasma than HFF cells. Various studies have shown the selectivity of CAP treatment (14, 36). Lin et al. (37) evaluated the plasma inhibitory effects in different tumor cells (A549 and HeLa) and normal cells (HepG2 and GM0637) *in vitro* and *in vivo*. They observed that plasma exerted a more proliferation inhibitory effect on tumor cells than normal cells. Biscop et al. (38) proposed a hypothesis that the reason for CAP selectivity could be influenced not only by the tumor or normal condition, but also by the culture medium and cell type. In this regard, they examined different cancer cells (A549, Mame-3M, A375, and, and U87) with their non-cancer counterparts (HEMa, HA, and BEAS-2B) and other culture mediums (DCBM, RPMI1640, DMEM, BEGM, and AM). They found that plasma has caused a selectivity effect between tumor and normal cells, and cell culture and cell type have less impact on the results.

Various features of a standardized treatment approach should be reviewed and chosen based on the general characteristics of CAP attributes for the clinical application of combined CAP and RT. Although some research have looked at the efficacy of plasma in conjunction with other treatment such as hyperthermia (39), chemotherapy (40), and PDT, no studies have looked at the combination of radiation therapy with CAP plus multifunctional nanoparticles. Currently, photocytotoxic damage is known to be caused by singlet oxygen acting on the cell membrane, but nuclear DNA is the main target for cell killing by ionizing radiation. Since PDT and RT cause damage to different targets synergy between them to kill the cells may improve tumor control. Considering these findings, it seems particularly interesting to assess the antitumor effects of innovative combination treatments. Reducing the dose of ionizing radiation while maintaining the desired tumor suppressor effect is important because it minimizes the potential damage caused by RT to normal problems. We found that the combination therapy (GNP@ICG+CAP+RT) induces an important cytotoxic effects on the melanoma cell lines. Since such effects could not be induced by high-dose radiation or using GNP@ICG, it was proved that CAP caused a synergistic improvement in combination therapy. It is accordance with Lin study (37). Similar to our study, they used CAP (based on Ar/O2 gas) 24 hours after RT to increase radiosensitivity in the treatment of various types of cancer, and compared the results to the treatment results of healthy cells. It was founded CAP inhibits the growth of tumors and induces apoptosis. Moreover, the effect of CAP on cancer cells is more effective than on normal cells. ROS generation is the reason why combination therapy has a synergistic effect.

Apoptosis, or programmed cell death, determines a genetically encoded cell death program that is

biochemically and morphologically completely different from accidental or necrotic cell death. The flow cytometric assay was broadly used to assess apoptosis in a variety of experimental methods. It is based on the principle that apoptotic cells are characterized by DNA fragmentation and the absence of nuclear DNA content, among other normal properties. Using fluorescent dyes such as FITC and PI that can bind and label DNA, a flow cytometry analysis can quickly and accurately measure the DNA content of cells. The induction of apoptosis by DNA damage or lipid peroxidation of the cell membrane is the most significant mechanism of the cell-plasma interaction, thus a flow cytometry assay to determine the amount of impact is a good test. Besides, apoptosis was identified as an attractive cell death pathway in response to cancer treatment modalities compared to necrotic cell death in terms of the damage to adjacent healthy cells.

Flow cytometric results show that under RT and CAP irradiation, the majority of cell death in melanoma and fibroblast cells is caused by apoptosis, and significant levels of apoptosis occur, especially in the combination treatment group (GNP@ICG+CAP+RT). It showed that it did about 75% in the DFW cells with combined therapy. However, the number of necrotic cells was measured insignificant. The flow cytometric results confirmed the MTT results. Our results are in agreement with previous results, as CAP promoted unparalleled levels of apoptosis induction in cancer cells (40).

The minimum survival in cancer cells was attained when radiation therapy was given 24 hours after CAP therapy in the presence of GNP@ICG. Cell cycle arrest was proposed as a potentially effective technique for inhibiting cancer cell growth. As a result, cell cycle modulation is a mechanism that may improve RT sensitivity during CAP therapy. There hasn't been any research on the appropriate sequence and interval between CAP and RT for maximum therapeutic effectiveness. It might go better in as little as 24 hours or as long as a week.

The colony assay is the gold standard test for measuring cellular death induced by ionizing radiation. It was performed to evaluate the long-term effects of RT and combined therapy on the DFW cell line. The results of the colony test showed a very low curve slope for the control group, which confirms the radiation resistance of melanoma cells. It was found that GNP@ICG had no effect on colony formation, according GNP@ICG+CAP+RT), especially for the 24 hours interval, increased slope indicates a decrease in the number of colonies, thusly the effectiveness of combination therapy on radiation-resistant melanoma cells. Better results require more complementary *in vitro* and *in vivo* studies on various cancer and normal cell lines, and it needs to evaluate other physical parameters such as the voltage, gas and other CAP techniques.

Conclusion

Using non-ionizing cold plasma treatment along with RT reduces the side effects of ionizing radiation, such as secondary cancer risks and damage to sensitive tissues adjacent to the tumor, and improves treatment outcomes. The present study involved the combination of plasma treatment and RT in the presence of GNP@ICG, as a photo-radio sensitizer, on DFW and HFF cell lines. It was found that plasma alone or in combination with radiotherapy is able to reduce the survival of melanoma cells without significantly damaging healthy ones. Though plasma is a nascent technique and requires further *in vivo* and preclinical studies, multiple studies, including this one, confirm that it serves as an adjunctive therapy. The incidence of PDT with CAP was also reaffirmed. To our knowledge, it is also the first time we have seen proof that GNP@ICG has been proven effective in collaboration with plasma and radiation therapy. Furthermore, a 24 hours interval between the plasma and radiation remedies improves treatment results.

Acknowledgements

This study was funded by Isfahan University of Medical Sciences (Grant No. 399825), as part of the requirements for a Ph.D. dissertation. The authors declare that there is no conflict of interest in this study.

Authors' Contributions

S.M.; Participated in study design, data collection, drafting and statistical analysis. A.Sh., A.S.; Were responsible for overall supervision, data evaluation, and contributed to conception and design. N.A., S.A.A.; Contributed extensively in interpretation of the data and the conclusion. All authors read and approved the final manuscript.

References

1. Jenkins RW, Fisher DE. Treatment of advanced melanoma in 2020 and beyond. J Invest Dermatol. 2021; 141(1): 23-31.
2. Trappetti V, Fazzari JM, Fernandez-palomo C, Scheidegger M, Volarevic V, Martin OA, et al. Microbeam radiotherapy—a novel therapeutic approach to overcome radioresistance and enhance anti-tumour response in melanoma. Int J Mol Sci. 2021; 22(14): 7755.
3. Zhang L, Ji Z, Zhang J, Yang S. Photodynamic therapy enhances skin cancer chemotherapy effects through autophagy regulation. Photodiagnosis Photodyn Ther. 2019; 28: 159-165.
4. Zhu W, Lee SJ, Castro NJ, Yan D, Keidar M, Zhang LG. Synergistic effect of cold atmospheric plasma and drug loaded core-shell nanoparticles on inhibiting breast cancer cell growth. Sci Rep. 2016; 6: 21974.
5. Correia JH, Rodrigues JA, Pimenta S, Dong T, Yang Z. Photodynamic therapy review: principles, photosensitizers, applications, and future directions. Pharmaceutics. 2021; 13(9): 1332.
6. Li XY, Tan LC, Dong LW, Zhang WQ, Shen XX, Lu X, et al. Susceptibility and resistance mechanisms during photodynamic therapy of melanoma. Front Oncol. 2020; 10: 597.
7. Nakajima K, Ogawa M. Phototoxicity in near-infrared photoimmunotherapy is influenced by the subcellular localization of antibody-IR700. Photodiagnosis Photodyn Ther. 2020; 31: 101926.
8. Babington P, Rajjoub K, Canady J, Siu A, Keidar M, Sherman JH. Use of cold atmospheric plasma in the treatment of cancer. Biointerphases. 2017; 10(2): 029403.
9. Mohd Nasir N, Lee BK, Yap SS, Thong KL, Yap SL. Cold plasma inactivation of chronic wound bacteria. Arch Biochem Biophys. 2016; 605: 76-85.
10. Kleineidam B, Nokhbehsaim M, Deschner J, Wahl G. Effect of cold

plasma on periodontal wound healing—an in vitro study. Clin Oral Investig. 2019; 23: 1941-1950.
11. Keping YA, Qikang JI, Zheng C, Guanlei DE, Shengyong YI, Zhen LI. Pulsed cold plasma-induced blood coagulation and its pilot application in stanching bleeding during rat hepatectomy. Plasma Sci Technol. 2018; 20(4): 044005.
12. Mateu-Sanz M, Tornín J, Brulin B, Khlyustova A, Ginebra MP, Layrolle P, et al. Cold plasma-treated ringer's saline: a weapon to target osteosarcoma. Cancers (Basel). 2020; 12(1): 227.
13. Mirpour S, Piroozmand S, Soleimani N, Jalali Faharani N, Ghomi H, Fotovat Eskandari H, et al. Utilizing the micron sized non-thermal atmospheric pressure plasma inside the animal body for the tumor treatment application. Sci Rep. 2016; 6(1): 29048.
14. Yazdani Z, Mehrabanjoubani P, Biparva P, Rafiei A. Cytotoxicity effect of cold atmospheric plasma on melanoma (B16-f10), breast (mcf-7) and lung (a549) cancer cell lines compared with normal cells. J Mazandaran Univ Med Sci. 2020; 30(187): 38-48.
15. Sklias K, Santos Sousa J, Girard PM. Role of short- and long-lived reactive species on the selectivity and anti-cancer action of plasma treatment in vitro. Cancers (Basel). 2021; 13(4): 615.
16. Vijayarangan V, Delalande A, Dozias S, Pouvesle JM, Robert E, Pichon C. New insights on molecular internalization and drug delivery following plasma jet exposures. Int J Pharm. 2020; 589: 119874.
17. Bauer G, Graves DB. Mechanisms of selective antitumor action of cold atmospheric plasma-derived reactive oxygen and nitrogen species. Plasma Process Polym. 2016; 13: 1157-1178.
18. Mateu-Sanz M, Tornín J, Ginebra MP, Canal C. Cold atmospheric plasma: a new strategy based primarily on oxidative stress for osteosarcoma therapy. J Clin Med. 2021; 10(4): 893.
19. Kurita H, Haruta N, Uchihashi Y, Seto T, Takashima K. Strand breaks and chemical modification of intracellular DNA induced by cold atmospheric pressure plasma irradiation. PLoS One. 2020; 15(5): e0232724.
20. Hua D, Cai D, Ning M, Yu L, Zhang Z, Han P, et al. Cold atmospheric plasma selectively induces G0/G1 cell cycle arrest and apoptosis in AR-independent prostate cancer cells. J Cancer. 2021; 12(19): 5977-5986.
21. Fan J, Cheng Y, Sun M. Functionalized gold nanoparticles: synthesis, properties and biomedical applications. Chem Rec. 2020; 20(12): 1474-1504.
22. Aryal S, Bisht G. New paradigm for a targeted cancer therapeutic approach: a short review on potential synergy of gold nanoparticles and cold atmospheric plasma. Biomedicines. 2017; 5(3): 38.
23. Jawaid P, Rehman MU, Zhao QL, Misawa M, Ishikawa K, Hori M, et al. Small size gold nanoparticles enhance apoptosis-induced by cold atmospheric plasma via depletion of intracellular GSH and modification of oxidative stress. Cell Death Discov. 2020; 6: 83.
24. Chien YY, Wang TY, Liao PW, Wu WC, Chen CY. Folate-conjugaed and dual stimuli-responsive mixed micelles loading Indocyanine green for photothermal and photodynamic therapy. Macromol Biosci. 2018;18(6): e1700409.
25. Anshup A, Venkataraman JS, Subramaniam C, Kumar RR, Priya S, Kumar TR, et al. Growth of gold nanoparticles in human cells. Langmuir. 2005; 21(25): 11562-11567.
26. Hall EJ, Giaccia AJ. Radiobiology for the radiologist. 8th ed. Lippincottt William & Wilkins: 2018.
27. Szili EJ, Oh JS, Fukuhara H, Bhatia R, Gaur N, Nguyen CK, et al. Modelling the helium plasma jet delivery of reactive species into a 3D cancer tumour. Plasma Sources Sci Technol. 2018; 27: 14001.
28. Farooq MA, Niazi AK, Akhtar J, Farooq M, Souri Z, Karimi N, Rengel Z. Acquiring control: The evolution of ROS-Induced oxidative stress and redox signaling pathways in plant stress responses. Plant Physiol Biochem. 2019; 141: 353-369.
29. Momeni S, Bahreyni Toosi MT, Anvari K, Gholamhosseinian H, Soleymanifard S. Comparing two radiotherapy techniques of whole central nervous system tumors, considering tumor and critical organs' dose provided by treatment planning system and direct measurement. J Cancer Res Ther. 2020; 16(6): 1470-1475.
30. Zhang Y, Huang F, Ren C, Liu J, Yang L, Chen S, et al. Enhanced radiosensitization by gold nanoparticles with acid-triggered aggregation in cancer radiotherapy. Adv Sci (Weinh). 2019; 6(8): 1801806.
31. Vlastou E, Diamantopoulos S, Efstathopoulos EP. Monte Carlo studies in Gold Nanoparticles enhanced radiotherapy: the impact of modelled parameters in dose enhancement. Phys Med. 2020; 80: 57-64.
32. Sazgarnia A, Bahreyni-Toosi MH, Montazerabadi AR, Ahmadi A. Indocyanine green acts as a photosensitizer but not a radiosensitizer: combined chemo-, photo-and radiotherapy of DFW human melanoma cells. J Exp Ther Oncol. 2016; 10(3): 189-196.
33. Karami-Gadallo L, Ghoranneviss M, Ataie-Fashtami L, Pouladian M, Sardari D. Enhancement of cancerous cells treatment by applying cold atmospheric plasma and photo dynamic therapy simultaneously. Clin Plasma Med. 2017; 7: 46-51.
34. Wang M, Geilich BM, Keidar M, Webster TJ. Killing malignant melanoma cells with protoporphyrin IX-loaded polymersome-mediated photodynamic therapy and cold atmospheric plasma. Int J Nanomedicine. 2017; 12: 4117-4127.
35. Vejdani Noghreiyan A, Imanparast A, Shayesteh Ara E, Soudmand S, Vejdani Noghreiyan V, Sazgarnia A. In-vitro investigation of cold atmospheric plasma induced photodynamic effect by Indocyanine green and Protoporphyrin IX. Photodiagnosis Photodyn Ther. 2020; 31: 101822.
36. Keidar M, Walk R, Shashurin A, Srinivasan P, Sandler A, Dasgupta S, et al. Cold plasma selectivity and the possibility of a paradigm shift in cancer therapy. Br J Cancer. 2016; 105(9): 1295-1301.
37. Lin L, Wang L, Liu Y, Xu C, Tu Y, Zhou J. Non-thermal plasma inhibits tumor growth and proliferation and enhances the sensitivity to radiation in vitro and in vivo. Oncol Rep. 2018; 40(6): 3405-3415.
38. Biscop E, Lin A, Van Boxem W, Van Loenhout J, De Backer J, Deben C, Dewilde S, Smits E, Bogaerts A. The influence of cell type and culture medium on determining cancer selectivity of cold atmospheric plasma treatment. Cancers (Basel). 2019; 11(9): 1287.
39. Moniruzzaman R, Rehman MU, Zhao QL, Jawaid P, Takeda K, Ishikawa K, et al. Cold atmospheric helium plasma causes synergistic enhancement in cell death with hyperthermia and an additive enhancement with radiation. Sci Rep. 2017; 7(1): 11659.
40. Saadati F, Mahdikia H, Abbaszadeh HA, Abdollahifar MA, Khoramgah MS, Shokri B. Comparison of direct and indirect cold atmospheric-pressure plasma methods in the B16F10 melanoma cancer cells treatment. Sci Rep. 2018; 8(1): 7689.

Cell J
Cell Journal(Yakhteh)
Homepage: https://www.celljournal.org/
Original Article
Vol 25, No 1, January 2023, Pages: 62-72

In Silico Analysis of Neutralizing Antibody Epitopes on The Hepatitis C Virus Surface Glycoproteins

Raziyeh Zareh-Khoshchehreh, Ph.D.[1], Taravat Bamdad, Ph.D.[1]*, Seyed Shahriar Arab, Ph.D.[2], Mahdi Behdani, Ph.D.[3], Mahmoud Biglar, Ph.D.[4]*

1. Department of Virology, School of Medical Sciences, Tarbiat Modares University, Tehran, Iran
2. Department of Biophysics, Faculty of Biological Sciences, Tarbiat Modares University-TMU, Tehran, Iran
3. Department of Biotechnology, Biotechnology Research Center, Venom and Biotherapeutics Molecules Lab, Pasteur Institute of Iran, Tehran, Iran
4. Department of Pharmacy, Drug Design and Development Research Center, Tehran University of Medical Sciences, Tehran, Iran

**Corresponding Addresses: P.O.Box: 14155-4838, Department of Virology, School of Medical Sciences, Tarbiat Modares University, Tehran, Iran P.O.Box: 14155-6559, Department of Pharmacy, Drug Design and Development Research Center, Tehran University of Medical Sciences, Tehran, Iran*
Emails: BAMDAD_T@modares.ac.ir, mbiglar@tums.ac.ir

Received: 11/November/2021, Revised: 10/June/2022, Accepted: 08/August/2022

Abstract

Objective: Despite of antiviral drugs and successful treatment, an effective vaccine against hepatitis C virus (HCV) infection is still required. Recently, bioinformatic methods same as prediction algorithms, have greatly contributed to the use of peptides in the design of immunogenic vaccines. Therefore, finding more conserved sites on the surface glycoproteins (E1 and E2) of HCV, as major targets to design an effective vaccine against genetically different viruses in each genotype was the goal of the study.

Materials and Methods: In this experimental study, 100 entire sequences of E1 and E2 were retrieved from the NCBI website and analyzed in terms of mutations and critical sites by Bioedit 7.7.9, MEGA X software. Furthermore, HCV-1a samples were obtained from some infected people in Iran, and reverse transcriptase-polymerase chain reaction (RT-PCR) assay was optimized to amplify their E1 and E2 genes. Moreover, all three-dimensional structures of E1 and E2 downloaded from the PDB database were analyzed by YASARA. In the next step, three interest areas of humoral immunity in the E2 glycoprotein were evaluated. OSPREY3.0 protein design software was performed to increase the affinity to neutralizing antibodies in these areas.

Results: We found the effective in silico binding affinity of residues in three broadly neutralizing epitopes of E2 glycoprotein. First, positions that have substitution capacity were detected in these epitopes. Furthermore, residues that have high stability for substitution in these situations were indicated. Then, the mutants with the strongest affinity to neutralize antibodies were predicted. I414M, T416S, I422V, I414M-T416S, and Q412N-I414M-T416S substitutions theoretically were exhibited as mutants with the best affinity binding.

Conclusion: Using an innovative filtration strategy, the residues of E2 epitopes which have the best in silico binding affinity to neutralizing antibodies were exhibited and a distinct peptide library platform was designed.

Keywords: Broadly Neutralizing Antibody, Mutation, Peptide Library, Sequence Analysis

Citation: **Zareh-Khoshchehreh R, Bamdad T, Arab SSh, Behdani M, Biglar M. In silico analysis of neutralizing antibody epitopes on the hepatitis C virus surface glycoproteins. Cell J. 2023; 25(1): 62-72. doi: 10.22074/CELLJ.2022.253363.**

Introduction

Hepatitis C virus (HCV), a member of the genus Hepacivirus, of the *Orthornavirae* kingdom, is a positive-stranded RNA genome. The core embedded viral RNA is surrounded by a host-derived lipid envelope incorporated with two surface glycoproteins E1 and E2 (1).

These glycoproteins include a cluster of overlapping epitopes which involve in a viral attachment and a cell fusion as well as hypervariable regions (HVRs), stem regions, glycosylation sites**,** transmembrane domains (TMDs); disulfide bonds**,** heptad repeat and neutralizing antibodies response regions (2).

Among these areas, antibody binding sites are extremely immunogenic and contain a various range of interactions. For example, the virus can quickly escape with high variations in immunodominant epitopes of HVRs (3). The second group of immunogenic sites is defined as an antigenic domain B that includes conformational epitopes, which identify the majority of broadly neutralizing antibodies (bNAb) in various HCV genotypes (4, 5).

The bNAb epitopes can be targeted by a wide range of neutralizing antibodies which cause the infection inhibition. However, it is relatively difficult access to them on surface glycoproteins via the virion arrangement. So, it is possible that the virus escapes from the humoral immune system (6). A third group, an antigenic domain A, contains epitopes that lead to the non-neutralizing antibodies production (7, 8).

In the term of residue position, E1 residues, including 192-202 and 313-328, are interacted with weakly

neutralizing Ab H-111 and the bNAbs IGH505 as well as IGH526, respectively (9, 10). Furthermore, neutralizing Ab regions which are located on the E2 receptor include three areas. First, residues 412-423 are formed the Epitope I (EPI). This site encompasses the antigenic domain E related to a highly conserved linear epitope which participates in the bNAb response (11, 12). The second area is the Epitope II (EPII)/Domain B and D placed in the 434−446 residues that interact with some neutralizing monoclonal Abs (MAbs) (11, 13). The third area is the Epitope III (EPIII) in a part of Domain C (residues 538-540) that has limited neutralizing abilities and a part of Domain B (residues 523-535) which has bound by broadly neutralizing abilities (9, 13).

In general, in-silico techniques widely are used in the study of peptides and proteins (14-16). Moreover, the study of residue mutations, especially in protein critical sites has been very helpful in better understanding the function of proteins (17-19). One of the widely employed approaches in the epitope studies is to synthesize combinatorial libraries (20, 21). Totally, the peptide libraries are a powerful tool for protein-associated researches such as vaccines, drugs, and diagnostics studies (22, 23).

Different strategies can be used to produce peptide libraries. One of the most suitable methods is the "positional scanning library" that detects antibody epitopes. These types of libraries are particularly useful for peptide sequence optimization. In this strategy, the amino acid residue at a defined position is replaced by all other amino acids, one at a time. Then, activity measurement allows determining which amino-acid residue increases the peptide activity. In the Combinatorial Positional Peptide Libraries, two or more positions are changed at one time.

To aim of multi-epitope vaccines, novel antiviral drugs or new generation of detection kits design, this study focuses on the evaluating critical sites of HCV surface glycoproteins to design a distinct positional peptide library. This peptide library involves in the humoral immune responses.

Materials and Methods

This study protocol was confirmed by the Ethics Committee of Tarbiat Modares University (IR.MODARES.REC.1400.083).

Sample collection

In this experimental study, HCV-1a serum samples were obtained from fourteen Iranian patients who referred to the Keyvan Virology Medical Diagnostic Laboratory, Tehran, Iran. All of the patients had HCV-positive serological test results and no prior history of HCV treatment. We obtained a serum sample of both sexes in the age range from 20 to 70 years.

Reverse transcriptase-polymerase chain reaction and sequencing

Viral RNA was extracted from serum samples using a QIAamp viral RNA mini kit according to the manufacturer's instructions (Cat No:52904, Qiagen, Germany). Reverse transcriptase-polymerase chain reaction (RT-PCR) assay was optimized to amplify the E1 (576 bp) and E2 (1089 bp) genes of isolated viruses via four specific overlapping fragments that designed in this study. Primer pairs include:

HCV-

F1: 5′-TGTGCCCGCTTCAGCCTACCA-3′

R1: 5′-CTTCGCCCAGTTCCCCACCAT-3′

HCV-

F2: 5′-CCTGGCGGGCATAGCGTATTTCT-3′

R2: 5′-CAGCGGTGGCCTGGTGTTGTTA-3′

HCV-

F3: 5′-GTGGTGGGAACGACCGACAG-3′

R3: 5′-CCTCCGCTTGGGATATGAGTAACA-3′

HCV-

F4: 5′-AGCCTTGTCCACCGGCTCAT-3′

R4: 5′-CAGCGCCATTAACCCGACAAGAAC-3′ respectively.

Thermal conditions for all PCR assays were as follows: an initial denaturation step at 95°C for 8 minutes, 35 cycles at 95°C for 35 seconds, 60°C for 35 seconds, and 72°C for 45 seconds and a final extension step at 72°C for 10 minutes.

PCR reaction products were gel- purified, and their sequencing was determined via a bidirectional approach using the above primers. The accuracy of primary sequences was confirmed by the BLAST database (http://www.ncbi.nlm.nih.gov/BLAST/).

Sequence analysis

In addition to RT-PCR sequences, 100 sequences of HCV genotype 1a were retrieved from the GenBank of National Center for Biotechnology Information (NCBI) Databases (http://ncbi.nlm.nih.gov). The nucleotide alignment was performed for all sequences with the reference strains of the HCV genotype 1 (Accession numbers: NC_038882 and NC_004102). The Clustal W program that implemented in the Bioedit 7.7.9 and MEGA X (24) was used for the multiple alignments. Moreover, all 14 obtained sequences were deposited in the GenBank with accession numbers MW736574 to MW736578 for the E1 gene as well as the accession numbers MW736579 to MW736587 for E2.

Analysis of primary and secondary structure

All full length of E1 and E2 was evaluated to find the best neutralizing residues. At first, the active sites of the HCV-E1 and E2 structures were found from the recently published literatures (2, 25).

Then, 100 protein sequences of HCV surface glycoproteins were obtained from the UniProtKB/Swiss-Prot database (https://www.uniprot.org/statistics/Swiss-Prot). Moreover, the amino acid sequences were deduced from the nucleotide sequences of RT-PCR products. Then, missense and silent mutations were assessed in all sequences by the MEGA X software (24). Also, a selective pressure possibility was calculated to better understand of the substitution rate in the RT-PCR products. It was obtained using the methods of Nei and Gojobori in the Lanl database (https://www.hiv.lanl.gov).

Base of acquired information was selected bNAb epitopes as the appropriate sites for peptide library design that effectively in stimulation of immune response. Therefore, the online ExPASy ProtParam software and YASARA program (26) were employed for investigation and evaluation of primary and secondary properties of selected epitope structures, respectively. It was performed to acquire primitive data about peptide interaction with antibodies and presented for future *in vitro* and *vivo* studies. Moreover, the immune epitope database (IEDB) (27) was used to investigate the previous experimentally derived HCV bNAb epitope data.

The inclusion criteria for mentioning software were based on properties of amino acid sequences and exclusion criteria were based on defined criteria in software.

Three-dimensional structure analysis

All three-dimensional structures (3D-structure) of HCV-E1 and E2 glycoproteins, which were bound to antibodies were retrieved from Protein Data Bank (PDB) (https://www.rcsb.org) with Pdb Ids, including 4N0Y, 4UOI, 4DGV, 4DGY, 4G6A, 4GAG, 4GAJ, 4HS6, 4HS8, 4MWF, 4WHT, 4XVJ, 5EOC, 5FGB, 5FGC, 5VXR, 6BKB, 6BKD, 6BKC, 6BZU, 6BZY, 6BZW, 6BZV, 4WEB, 4JZN, 4JZO, 4HZL, 4Q0X, 4Z0X, 5ERW, 2KZQ, 5NPH, 5NPJ and 5NPI. All of them were investigated to find the most significant structure of the binding antigen and antibody determinants. Thus, structural coordinates for all retrieved Pdb files were analyzed and visualized by PDB viewer software YASARA and SPDBV.

Substitution frequency

In order to better understanding of most common HCV-1a, that circulating in the infected population worldwide, the amino acid substitution frequency in each position of the bNAb epitopes was determined. On average, we analyzed information about 90% of the UniProtKB/Swiss-Prot HCV-1a sequences through Homology-derived Structures of Proteins (HSSP) software (http://bioinf.modares.ac.ir/software). The reference sequence of HCV-1a (Accession numbers: NC_004102) used as our input to HSSP and the amino acid substitution percentage was considered as our output. Subsequently, these data were compared with our amplicons sequences.

This study was hypothesized that some of E2 epitopes mutants have a substantial effect on the neutralizing antibody binding affinity. Therefore, the substitution frequency step was considered to decrease the total of predicted mutants and acquire the more stable immunogenic peptides. This filtration approach was implemented to avoid confusing the immune system in the face of various immunogenic epitopes as a virus escape strategy that is very important in the success of vaccine projects.

Furthermore, to compare the mentioned area in the other genotypes of HCV, the other reference sequences of HCV were retrieved from NCBI, including NC_009823.1, NC_009824.1, NC_009825.1, NC_009826.1, NC_009827.1 and NC_030791.1, and a comparison was made.

Mutagenesis

In the step of in silico mutagenesis to predict a residue with the strongest binding affinity to antibodies in each position, OSPREY 3.0 (Open Source Protein REdesign for You) software (28) was used. The mentioned PDB files with the best interaction properties were used as the input files for OSPREY. Also, only the most frequent residues detected in the previous section were used in OSPREY and the mutants were predicted.

Furthermore, the energy landscape alteration of bound and unbound situations caused by amino acid substitutions and their conformational entropy was analyzed and calculated by OSPREY. Finally, selected mutants with the strongest binding affinity predicted as output of OSPREY and presented as PDB files. Then, a distinct positional peptide library was designed from HCV-E2 bNAb epitopes.

Results

The epitope regions and their common substitutions of the HCV-1a glycoproteins, E1 and E2, were evaluated to design a practical peptide library from the bNAb epitopes. Totally, one hundred HCV-1a isolates, of both E1 and E2, were retrieved from NCBI. Moreover, nine HCV-E2 and five HCV-E1 sequences were obtained from RT-PCR products.

Sequence analysis

Due to evaluation on the representation of complete HCV-E1 and E2 genes, multiple alignments were implemented. The missense and silent substitutions in critical epitopes of HCV-E1 and E2 regions were determined (Fig.1).

Because of more nucleotide diversity in the HCV-E2 regions, the selective pressure possibility was calculated in entire sequences obtained from patients. Its value was 0.19 which means a negative possibility in these sequences (Non-Synonymous/Synonymous <1).

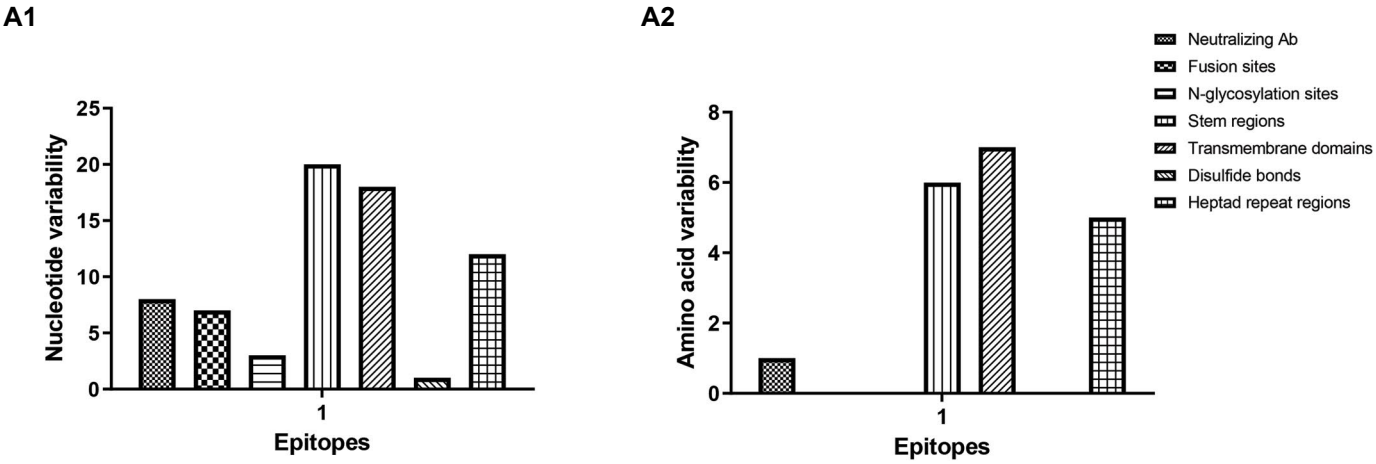

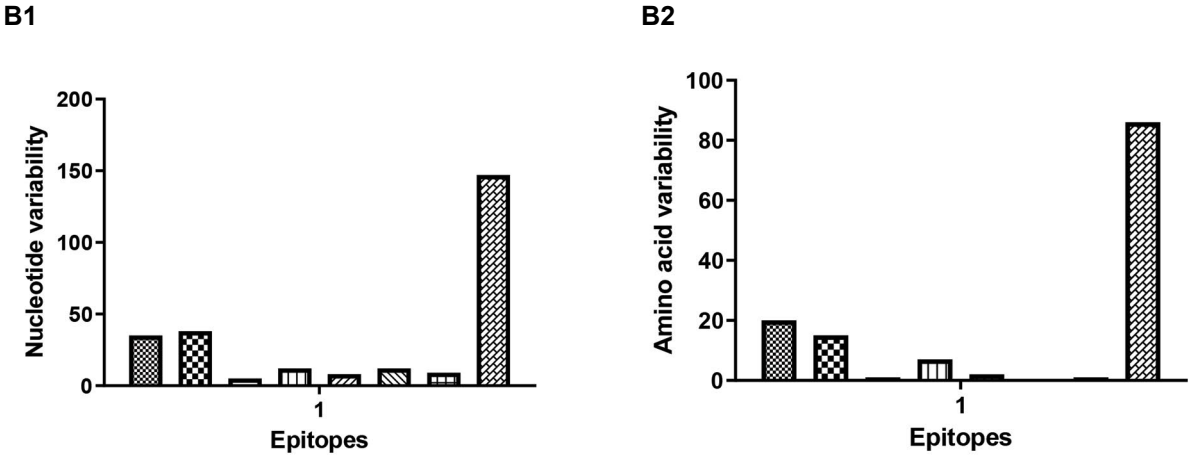

C

HCV-E1 192-202 (11 mer)	200
HCV REFSEQ (NC 004102)	YQVRNSSGLYH
Sample 1. HCV	.....
Sample 2. HCV	.....T....
Sample 3. HCV	.....
Sample 4. HCV	.....T....
Sample 5. HCV	.....

HCV-E1 313-328 (16 mer)	320
HCV REFSEQ (NC 004102)	ITGHRMAWDMMMNWSP
Sample 1. HCV	.....
Sample 2. HCV	.....
Sample 3. HCV	.....
Sample 4. HCV	.....
Sample 5. HCV	.....

D

HCV-E2 412-423 (12 mer)	420
HCV REFSEQ (NC 004102)	QLINTNGSWHIN
Sample 1. HCV.E2	.....
Sample 2. HCV.E2	.....
Sample 3. HCV.E2	.....
Sample 4. HCV.E2	.....
Sample 5. HCV.E2	.....
Sample 6. HCV.E2	.....R.L.
Sample 7. HCV.E2	.....L.
Sample 8. HCV.E2	..V.....
Sample 9. HCV.E2	.....

HCV-E2 434-446 (13 mer)	440
HCV REFSEQ (NC 004102)	NTGWLAGLFYQHK
Sample 1. HCV.E2	E.....Y..
Sample 2. HCV.E2	D.....H.N
Sample 3. HCV.E2	E.....H..
Sample 4. HCV.E2	H...V.....HYR
Sample 5. HCV.E2	D.....Y..
Sample 6. HCV.E2	K.....V.H..
Sample 7. HCV.E2	D.....H..
Sample 8. HCV.E2	D...I.....YN.
Sample 9. HCV.E2	D...V.....Y..

HCV-E2 523-540 (18 mer)	530 540
HCV REFSEQ (NC 004102)	GAPTYSWGANDTDVFVLN
Sample 1. HCV.E2	.V.....D.....
Sample 2. HCV.E2	.V...N..E.....
Sample 3. HCV.E2	.M.....E.....
Sample 4. HCV.E2	.....N..E.....
Sample 5. HCV.E2	.....N..E.....
Sample 6. HCV.E2	.....E.....
Sample 7. HCV.E2	.....N..E.....
Sample 8. HCV.E2	.....N..E.....
Sample 9. HCV.E2	.V.....E.....

Fig.1: The sequence variability of obtained HCV-E1 and E2 genes from the PCR products. The variability of **A1.** Nucleotide and **A2.** Amino acid sequences in different epitope regions of HCV-E1. The variability of **B1.** Nucleotide and **B2.** Amino acid sequences in different epitope regions of HCV-E2. **C.** Mutations in the E1 NAb epitopes of PCR products compared to reference sequence of HCV genotype 1a (NC_004102). **D.** Mutations in the E2 NAb epitopes of PCR products in comparison with the reference sequence of HCV genotype 1a (NC_004102). HCV; Hepatitis C virus and PCR; Polymerase chain reaction.

Epitope evaluation

We selected a cluster of epitopes related to humoral immune response from the reliable article (2), IEDB, and UniProtKB/Swiss-Prot databases. Of four bNAb epitopes, three epitopes (EPI, EPII, and EPIII) belonged to the HCV-E2, and one epitope belongs to the HCV-E1.

In the next step of epitope investigation, this cluster of epitopes was analyzed in terms of physicochemical properties using the ExPASy software and their stability was confirmed (Table 1). Their high aliphatic indexes indicate these epitopes are in a wide range of thermostability, although the EPI has the highest aliphatic indexes (90.50). Also, negative GRAVY values show that these molecules are nonpolar.

In the secondary structure, evaluation was indicated a suitable condition of atoms and residues placement. Also, it was shown β-Hairpin structures to binding to the antibody by YASARA. Thus, primary and secondary structures of mentioned epitopes were exhibited suitable for binding to neutralizing antibodies.

In general, according to integrated data it looked better to select EPI in the E2 glycoprotein for the following current study.

Mutation frequency

The percentage of mutation frequency was analyzed by using the HSSP databases for about 90% of E1 and E2 sequences in the NCBI. In this filtration strategy, five positions of the EPI, nine positions of the EPII, and eleven positions of the EPIII were detected as changeable and desirable sites of mutagenesis. We detected residues that could be substituted in these situations with high stability (Table 2). The bNAb site of E1 was highly conserved and limited number of mutations was observed among all the evaluated strains. Thus, E1 was excluded from this study.

These data were in accordance with the obtained results from Sequence Analysis section. The rare substitutions contained W420R, N434E and A524M. The HCV stable variants, specifically for these epitopes, that were observed in this study were too different of our result of database analysis.

The peptide sequences of seven reference genotypes were compared to evaluate the selected epitopes in the other HCV genotypes (Table 3). It was indicated that the EPI is the most conserved epitope among all HCV genotypes, but EPII and EPIII had clear variability.

Table 1: Physicochemical properties of bNAb epitopes in the HCV-E2 glycoprotein

Physicochemical parameters	EPI (12 mer)	EPII (13 mer)	EPIII (18 mer)
Start	412	434	523
End	423	446	540
Residue sequence of ref-eeq (NC_004102)	QLINTNGSWHIN	NTGWLAGLFYQHK	GAPTYSWGANDTDVFVLN
Molecular weight	1396.53	1534.74	1927.06
Theoretical pI	6.74	8.60	3.56
Total number of atoms	192	213	260
Aliphatic indexes	90.50	67.69	65.00
Extinction coefficients	5500	6990	6990
Instability index	33.39	58.45	-3.40
Grand average of hydropathicity (GRAVY)	-0.600	-0.431	-0.122

These analyses were performed by the online ExPASy ProtParam software.

Table 2: Percentage of mutation variability in the bNAb epitopes of the HCV-E2 glycoprotein

Epitope	Amino acid positions	Percentage of amino acid substitution							
EPI	412	Q 92%	H 3%	E 1%	N 1%	S 1%	G 1%		
	413	**L 100%							
	414	I 70%	V 29%	M 1%					
	415	N 94%	R 3%	K 1%	H 1%				
	416	T 91%	S 6%	A 3%					
	417	N 99%							
	418	G 99%							
	419	S 99%							
	420	**W 100%							
	421	**H 100%							
	422	I 94%	L 5%	V 1%					
	423	**N 100%							
EPII	434	N 47%	D 19%	H 12%	Q 12%	K 2%	T 1%	S 1%	
	435	T 99%	A 1%						
	436	**G 100%							
	437	W 61%	F 39%						
	438	L 36%	I 48%	V 15%	F 1%				
	439	A 99%							
	440	G 76%	A 18%	S 6%					
	441	**L 100%							
	442	F 80%	L 11%	I 8%	V 1%				
	443	Y 98%	H 1%						
	444	Q 1%	Y 38%	H 22%	T 15%	R 9%	S 4%	V 2%	F 1%
	445	H 54%	N 27%	Y 9%	R 5%	S 2%	K 1%	Q 1%	
	446	K 73%	R 17%	N 5%	S 4%	Q 1%			
EPIII	523	**G 100%							
	524	A 59%	V 31%	E 2%	N 2%	I 2%	T 1%	L 1%	
	525	P 99%							
	526	T 96%	A 4%						
	527	Y 94%	F 5%						
	528	S 21%	N 48%	T 19%	R 8%	G 1%	K 1%		
	529	W 99%	F 1%						
	530	**G 100%							
	531	A 21%	E 57%	G 7%	S 7%	D 5%	T 1%	V 1%	C 1%
	532	N 98%	K 1%						
	533	D 45%	E 48%	V 2%					
	534	T 96%	S 3%						
	535	**D 100%							
	536	V 99%							
	537	F 81%	L 18%						
	538	V 58%	L 37%	I 4%	M 1%				
	539	L 99%							
	540	N 81%	E 7%	K 3%	R 3%	T 2%	D 1%	Q 1%	

**; Some substitutions with a special score in the table, such as 100%, are extremely close to it but not exactly.

Table 3: Comparing three peptide regions (EPI, EPII, and EPIII in genotype 1) among seven reference genotypes of the HCV in the E2 glycoprotein

Peptide region	Genotype	Accession number of ref seq	Residues
EPI	1	NC_004102	QLINTNGSWHIN
	2	NC_009823.1	QL**V**NTNGSWHIN
	3	NC_009824.1	QL**V**NTNGSWHIN
	4	NC_009825.1	QLIN**S**NGSWHIN
	5	NC_009826.1	Q**FV**N**T**NGSWHIN
	6	NC_009827.1	QLINTNGSWHIN
	7	NC_030791.1	QLINTNGSWHIN
EPII	1	NC_004102	NTGWLAGLFYQHK
	2	NC_009823.1	**H**TG**FI**A**S**LFY**T**H**S**
	3	NC_009824.1	NTG**FI**AGLFY**Y**HK
	4	NC_009825.1	NTG**F**LA**S**LFY**T**HK
	5	NC_009826.1	**Q**TG**FI**AG**IM**Y**A**HK
	6	NC_009827.1	**Q**TG**FLSA**LFY**RSN**
	7	NC_030791.1	**Q**TG**F**LAA**L**FY**T**H**R**
EPIII	1	NC_004102	GAPTYSWGANDTDVFVLN
	2	NC_009823.1	GAPTY**T**WG**E**N**E**TDVF**L**LN
	3	NC_009824.1	G**V**PTY**T**WG**E**N**EK**DVF**L**LL**K**
	4	NC_009825.1	G**V**PTY**T**WG**E**N**E**TDVF**L**LN
	5	NC_009826.1	G**C**PTY**N**WG**S**N**E**TD**ILL**LN
	6	NC_009827.1	G**N**PTY**N**WG**E**N**E**TDVF**M**L**E**
	7	NC_030791.1	G**V**PTY**T**WG**E**N**ES**DVF**X**LN

Bold letter shows the substitutions.

Desirable substitutions prediction on the bNAb regions

The structural coordinates and characteristics within the 3D-structure of the HCV-E2 in a complex with neutralizing antibodies were analyzed and visualized by the PDB viewer software, YASARA and SPDBV. Two 3D-structures, PDB IDs were selected, including 4DGV for EPI and 4MWF for EPII and EPIII. Based on the most significant situation in binding between mentioned epitope and antibodies, we considered in this selection. 4MWF is the most complete 3-D structure of E2, which has been presented and use for EPII and EPIII analysis. However, a part of EPI was deleted in this PDB file. So, 4DGV for EPI evaluation was selected. It makes the best binding structure between EPI residues and antibody determinant.

Then, to design a worthy peptide library from the bNAb epitopes of E2, substitutions with the strongest affinity to neutralize antibodies were predicted using OSPREY 3.0. The obtained residues from the previous filtration step were used in this design (Table 4).

Score alteration based on the energy landscape of possible situations and their conformational entropies were calculated (Table 4). The results revealed the residue that had the strongest binding affinity to antibodies and a minimum score.

The integrated results showed that the EPI was the best region among bNAb epitopes of E2, although the EPII and EPIII had a slightly lower score than the EPI through OSPREY. These scores can be related to differences of selected PDB IDs.

On the other hand, Q412E substitution has the lowest score among EPI residues in the PDB ID 4DGV. But it was not reproducible among other PDB IDs. Thus, I414M was acquired an excellent score in the EPI region. Moreover, T416S and I422V substitutions were exhibited pleasant scores. Also, Q412H, I414V and I422L were demonstrated more circulating among the infected population (Table 2). For this reason, they are mostly neutralized by antibodies. It may be related to the virus escape strategies.

Moreover, EPII and EPIII were evaluated in PDB ID 4MWF by the following these methods. Then, their appropriate substitution was exhibited (Table 4). Due to the greater importance of the EPI, simultaneous mutations were also investigated in this epitope. Finally, a Positional Peptide Library from a cluster of the bNAb epitope of the HCV-E2 was mapped using obtained results (Fig.2).

Table 4: The binding scores of the bNAb epitopes on the HCV-E2 glycoprotein in complex with MAbs through OSPREY3.0

Epitope of E2 glycoprotein	PDB ID	Chain	Residue number	Residue(s) in ref seq	Altered residue	Score
EPI	4DGV	A	412	Q	E	-20.25
(412-423 aa)		A	414	I	M	-14.13
		A	415	N	H	171.68
		A	416	T	S	-12.59
		A	422	I	V	-9.82
		A	414, 415	I, N	M, H	158.46
		A	414, 416	I, T	M, S	-26.05
		A	412, 414, 416	Q, I, T	N, M, S	-45.38
		A	414, 416, 422	I, T, I	M, S, V	-35.44
EPII	4MWF	C	437	W	F	-29.11
(434-446 aa)		C	440	G	S	1104.13
		C	444	Q	R	-58.02
		C	445	H	N	-39.47
		C	446	K	R	-58.69
		D	437	W	F	-39.14
		D	440	G	A	211.27
		D	444	Q	R	-58.40
		D	445	H	S	-40.39
		D	446	K	R	-57.89
EPIII	4MWF	C	524	A	N	-46.69
(523-535, 536-540 aa)		C	526	T	A	-32.72
		C	527	Y	F	-37.32
		C	528	S	R	-58.53
		C	529	W	F	-42.91
		C	531	A	E	-47.91
		C	533	D	E	-45.22
		C	534	T	S	-39.75
		C	537	F	L	35.91
		C	538	V	M	-40.43
		D	524	A	N	-43.27
		D	526	T	A	-33.67
		D	527	Y	F	-36.02
		D	528	S	R	-59.46
		D	529	W	F	-44.55
		D	531	A	G	-28.16
		D	533	D	E	-44.74
		D	534	T	S	-40.50
		D	537	F	L	33.17
		D	538	V	M	-41.13

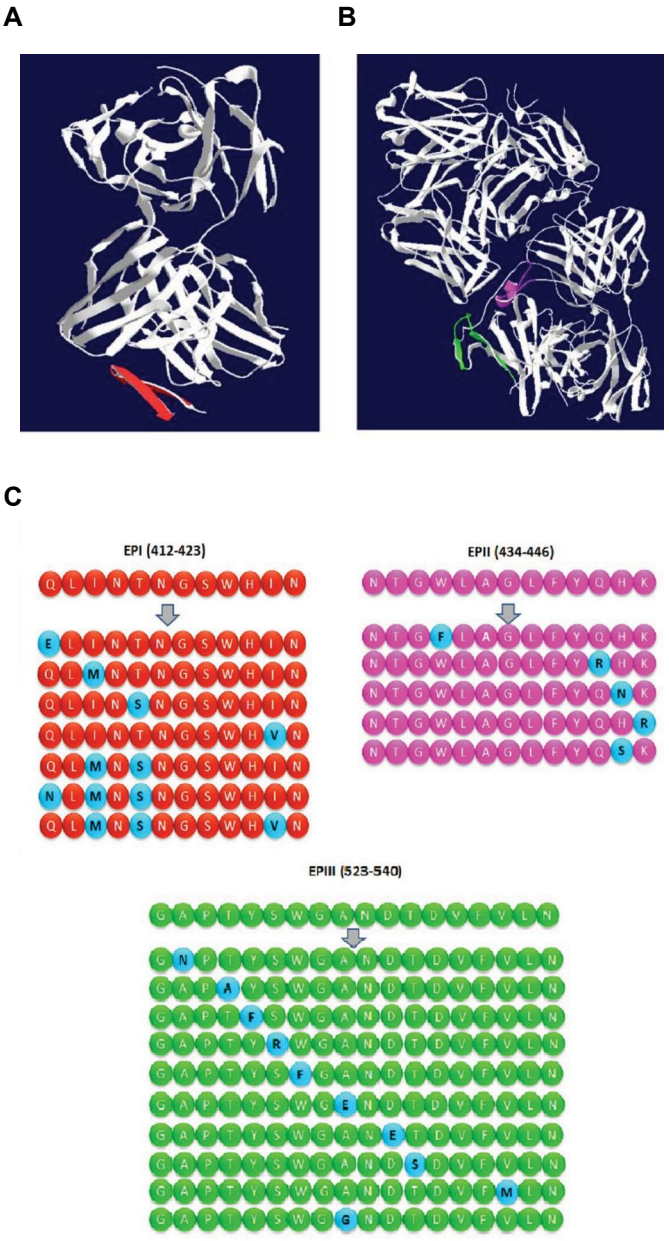

Fig.2: Designed positional peptide library from bNAb regions in the HCV-E2 glycoprotein. **A.** The crystal structure of EPI region (residues 412-423) in red (PDB ID: 4DGV). **B.** The crystal structure of the EPII region (residues 434-446) in purple and EPIII region (residues 523-540) in green (PDB ID: 4MWF). **C.** Designed positional peptide library from EPI, EPII, and EPIII of HCV-E2 glycoprotein from the most common substitutions circulating in the host HCV population using OSPREY. HCV; Hepatitis C virus and PCR; Polymerase chain reaction.

Discussion

One of the novel strategies of vaccine designing is implementing critical epitopes instead of using entire immunogenic protein. Many studies have been done on the mutagenesis of HCV epitopes and Multi-epitope vaccines until now (29, 30).

The ability of HCV in quick production of escape mutants is one of the considerable points of a vaccine production. The HCV contains a cluster of overlapping immunogenic epitopes in its surface glycoproteins that includes these escape mutants areas. This cluster is a suitable target for designing vaccines, novel drugs, or the new generation of detection kits.

To evaluate of immunogenic epitopes on the 3-D structure of HCV, PDB database was used. The results were demonstrated that the 4N0Y was the only 3-D structure of bNAb sites of E1 (residues 314-324). It was complex with the MAb IGH526 (10). Also, 4DGV and 4MWF detected as two of the best structures of E2 in investigation of binding affinity. These structures included bNAb epitopes in complex with Human neutralizing antibodies. These bNAbs named HCV1 and AR3c for 4DGV and 4MWF, respectively (31, 32).

According to integrated results, the cluster of E2 epitopes, influences B cell responses. So, E2 were picked out by focusing on bNAbs production as a key point.

In general, the results of the current study were shown that the substitution pattern of the obtained strains from Iran and the other sequences from NCBI were similar, although some mutations such as W420R are rare.

Previous studies have reported some substitution like L438V, which was visualized in the EPII of obtained sequences from PCR products, lead to the viral escape from monoclonal antibody (MAb) CBH-2 and reduce viral fitness in the cell culture by MAb HC-11 (33) or altering E2 receptor binding (34). But this substitution may be neutralized by the other neutralizing antibodies such as no-human MAbs (35). Therefore, there is a need for further studies using new strategies like what is suggested in this study.

In the current study, was shown that not only some residues are stably circulating in the host population, but also every substitution couldn't use for vaccine and immune stimulation. In fact, there was a specified pattern of substitutions, even in the protein sequences of a virus with the quasispecies ability. None of the mutagenesis studies relating to HCV has mentioned this issue in mutant production. According to previous studies, many experimentally-proven resistant mutants in peptide libraries were found rarely in the host population. In fact, 24% of them did not detect in any of the natural sequences (35, 36). Nevertheless, the residues that are great conserved in the host population mention a selection pressure to restrict mutation. Indeed, we believe that mutagenesis using common mutations in HCV strains of infected individuals can help to produce multi-epitope vaccines and development of effective immunity.

In the second step of filtration were detected the mutants with the strongest affinity to neutralizing antibodies by OSPREY. For instance, in position 414 located in EPI, a Methionine with the lowest score was detected by the most powerful connection among single mutations. Interestingly, N415 was determined inappropriate position for substitutions. However, there are several studies on mutagenesis in

this position (35). In addition to single substitutions, simultaneous mutations naturally were occurred in the special region of HCV strains. Consequently, combinatorial substitutions in unique peptide sequences are indicated. I414M-T416S with two substitutions was detected as the most stable combinatorial mutations in EPI by OSPREY.

The previous studies on conformational changes have been shown the alteration of protein function by mutation in critical binding sits (18, 19). Compared to previous HCV vaccine studies with multi-epitopes, our filtration strategy will enhance stable specific neutralizing antibody responses and reduce unwanted or non-neutralizing antibody responses. It is shown that EPI is the most conserved epitope among all HCV genotypes. Therefore, the predicted peptide library for EPI will be usable for all HCV genotypes. Hence, genotype five with three differentiations in amino acids may be an exception.

It might be predicted that a multi-epitope vaccine is reasonably type to produce a more specific induction of immune responses. Thus, it can be proposed that an approach of this study to design a peptide library and then multi-epitope vaccine for hypervariable pathogens can be useful by increasing in producing effective neutralizing antibodies.

The lack of a whole 3-D-structure for E1 and E2 glycoproteins and absence of E1 and E2 entire sequences from Iranian strains in NCBI were the limitations of the current study.

Generally, our results pointed to the design of a positional peptide library using replacement of filtered residues instead of all residues at the defined position. It theoretically to be effective against neutralizing antibodies was indicated. It was suggested to implement the mentioned strategy to design a peptide library as an innovative and cost-benefit procedure in the vaccine, drug, and diagnostic kits industry. To prove our hypothesis, the key point to design all vaccines is to induce and produce effective antibodies against the wild-type virus. This study was suggested epitopes with maximum coverage in wild-type viruses.

Conclusion

Here, we theoretically approached more stable and specific humoral immune response through an increase binding affinity of HCV mutants to neutralize antibody. Filtering many inefficient mutants of HCV that showed the best positional mutagenesis residues illustrated the significant role of positions 412, 414, 416, and 422 in the EPI of E2. Such platform may represent as a capable insight to design multi-epitope vaccines and/or novel medicine and/or diagnostics tools.

Acknowledgments

We acknowledge Fatemeh Hosseini for designing primers and helping in the RT-PCR assay as well as Zahra Sohbatzadeh. This study was performed as a part of the Ph.D. project granted by Tarbiat Modares University (Grant number: TMU-MED-4914). The authors declare that they have no conflict of interests.

Authors' Contributions

T.B.; Participated in the critical review of the manuscript and project administration. R.Z-Kh.; Conceived the study design, analyzed data and wrote the manuscript. S.Sh.A.; Introduced bioinformatics tools and contributed in silico data analysis. M.Be., M.Bi.; Were involved in the data collection and analysis. All the authors read and approved the final manuscript.

References

1. Lindenbach BD, Rice CM. The ins and outs of hepatitis C virus entry and assembly. Nat Rev Microbiol. 2013;11(10): 688-700.
2. Freedman H, Logan MR, Law JL, Houghton M. Structure and function of the hepatitis C virus envelope glycoproteins E1 and E2: antiviral and vaccine targets. ACS Infect Dis. 2016; 2(11): 749-762.
3. Shimizu YK, Hijikata M, Iwamoto A, Alter HJ, Purcell RH, Yoshikura H. Neutralizing antibodies against hepatitis C virus and the emergence of neutralization escape mutant viruses. J Virol. 1994; 68(3): 1494-1500.
4. Law M, Maruyama T, Lewis J, Giang E, Tarr AW, Stamataki Z, et al. Broadly neutralizing antibodies protect against hepatitis C virus quasispecies challenge. Nat Med. 2008; 14(1): 25-27.
5. Perotti M, Mancini N, Diotti RA, Tarr AW, Ball JK, Owsianka A, et al. Identification of a broadly cross-reacting and neutralizing human monoclonal antibody directed against the hepatitis C virus E2 protein. J Virol. 2008; 82(2): 1047-1052.
6. Keck ZY, Saha A, Xia J, Wang Y, Lau P, Krey T, et al. Mapping a region of hepatitis C virus E2 that is responsible for escape from neutralizing antibodies and a core CD81-binding region that does not tolerate neutralization escape mutations. J Virol. 2011; 85(20): 10451-10463.
7. Keck ZY, Xia J, Cai Z, Li TK, Owsianka AM, Patel AH, et al. Immunogenic and functional organization of hepatitis C virus (HCV) glycoprotein E2 on infectious HCV virions. J Virol. 2007; 81(2): 1043-1047.
8. Owsianka AM, Tarr AW, Keck ZY, Li TK, Witteveldt J, Adair R, et al. Broadly neutralizing human monoclonal antibodies to the hepatitis C virus E2 glycoprotein. J Gen Virol. 2008; 89(Pt 3): 653-659.
9. Keck ZY, Sung VM, Perkins S, Rowe J, Paul S, Liang TJ, et al. Human monoclonal antibody to hepatitis C virus E1 glycoprotein that blocks virus attachment and viral infectivity. J Virol. 2004; 78(13): 7257-7263.
10. Kong L, Kadam RU, Giang E, Ruwona TB, Nieusma T, Culhane JC, et al. Structure of hepatitis C virus envelope glycoprotein E1 antigenic site 314-324 in complex with antibody IGH526. J Mol Biol. 2015; 427(16): 2617-2628.
11. Keck ZY, Xia J, Wang Y, Wang W, Krey T, Prentoe J, et al. Human monoclonal antibodies to a novel cluster of conformational epitopes on HCV E2 with resistance to neutralization escape in a genotype 2a isolate. PLoS Pathog. 2012; 8(4): e1002653.
12. Potter JA, Owsianka AM, Jeffery N, Matthews DJ, Keck ZY, Lau P, et al. Toward a hepatitis C virus vaccine: the structural basis of hepatitis C virus neutralization by AP33, a broadly neutralizing antibody. J Virol. 2012; 86(23): 12923-12932.
13. Sautto G, Tarr AW, Mancini N, Clementi M. Structural and antigenic definition of hepatitis C virus E2 glycoprotein epitopes targeted by monoclonal antibodies. Clin Dev Immunol. 2013; 2013: 450963.
14. Bhardwaj VK, Singh R, Sharma J, Das P, Purohit R. Structural based study to identify new potential inhibitors for dual specificity tyrosine-phosphorylation- regulated kinase. Comput Methods Programs Biomed. 2020; 194: 105494.
15. Gopalakrishnan C, Kamaraj B, Purohit R. Mutations in microRNA binding sites of CEP genes involved in cancer. Cell Biochem Biophys. 2014; 70(3): 1933-1942.
16. Singh R, Bhardwaj VK, Purohit R. Potential of turmeric-derived compounds against RNA-dependent RNA polymerase of SARS-

CoV-2: an in-silico approach. Comput Biol Med. 2021; 139: 104965.
17. Tanwar G, Purohit R. Gain of native conformation of Aurora A S155R mutant by small molecules. J Cell Biochem. 2019; 120(7): 11104-11114.
18. Rajendran V, Gopalakrishnan C, Purohit R. Impact of point mutation P29S in RAC1 on tumorigenesis. Tumour Biol. 2016; 37(11): 15293-15304.
19. Rajendran V, Gopalakrishnan C, Sethumadhavan R. Pathological role of a point mutation (T315I) in BCR-ABL1 protein-A computational insight. J Cell Biochem. 2018; 119(1): 918-925.
20. De Berardinis P, Sartorius R, Fanutti C, Perham RN, Del Pozzo G, Guardiola J. Phage display of peptide epitopes from HIV-1 elicits strong cytolytic responses. Nat Biotechnol. 2000; 18(8): 873-876.
21. Li W, Li L, Sun T, He Y, Liu G, Xiao Z, et al. Spike protein-based epitopes predicted against SARS-CoV-2 through literature mining. Med Nov Technol Devices. 2020; 8: 100048.
22. Bozovičar K, Bratkovič T. Evolving a peptide: library platforms and diversification strategies. Int J Mol Sci. 2019; 21(1): 215.
23. Mink MA, Benichou S, Madaule P, Tiollais P, Prince AM, Inchauspe G. Characterization and mapping of a B-cell immunogenic domain in hepatitis C virus E2 glycoprotein using a yeast peptide library. Virology. 1994; 200(1): 246-255.
24. Kumar S, Stecher G, Li M, Knyaz C, Tamura K. MEGA X: molecular evolutionary genetics analysis across computing platforms. Mol Biol Evol. 2018; 35(6): 1547-1549.
25. Yechezkel I, Law M, Tzarum N. From structural studies to HCV vaccine design. Viruses. 2021; 13(5): 833.
26. Land H, Humble MS. YASARA: a tool to obtain structural guidance in biocatalytic investigations. Methods Mol Biol. 2018; 1685: 43-67.
27. Vita R, Mahajan S, Overton JA, Dhanda SK, Martini S, Cantrell JR, et al. The immune epitope database (IEDB): 2018 update. Nucleic Acids Res. 2019; 47(D1): D339-D343.
28. Hallen MA, Martin JW, Ojewole A, Jou JD, Lowegard AU, Frenkel MS, et al. OSPREY 3.0: open-source protein redesign for you, with powerful new features. J Comput Chem. 2018; 39(30): 2494-2507.
29. Bazmara S, Shadmani M, Ghasemnejad A, Aghazadeh H, Pooshang Bagheri K. In silico rational design of a novel tetra-epitope tetanus vaccine with complete population coverage using developed immunoinformatics and surface epitope mapping approaches. Med Hypotheses. 2019; 130: 109267.
30. Pierce BG, Keck ZY, Lau P, Fauvelle C, Gowthaman R, Baumert TF, et al. Global mapping of antibody recognition of the hepatitis C virus E2 glycoprotein: implications for vaccine design. Proc Natl Acad Sci USA. 2016; 113(45): E6946-E6954.
31. Kong L, Giang E, Nieusma T, Kadam RU, Cogburn KE, Hua Y, et al. Hepatitis C virus E2 envelope glycoprotein core structure. Science. 2013; 342(6162): 1090-1094.
32. Kong L, Giang E, Robbins JB, Stanfield RL, Burton DR, Wilson IA, et al. Structural basis of hepatitis C virus neutralization by broadly neutralizing antibody HCV1. Proc Natl Acad Sci USA. 2012; 109(24): 9499-9504.
33. Keck ZY, Olson O, Gal-Tanamy M, Xia J, Patel AH, Dreux M, et al. A point mutation leading to hepatitis C virus escape from neutralization by a monoclonal antibody to a conserved conformational epitope. J Virol. 2008; 82(12): 6067-6072.
34. El-Diwany R, Cohen VJ, Mankowski MC, Wasilewski LN, Brady JK, Snider AE, et al. Extra-epitopic hepatitis C virus polymorphisms confer resistance to broadly neutralizing antibodies by modulating binding to scavenger receptor B1. PLoS Pathog. 2017; 13(2): e1006235.
35. Rodrigo C, Walker MR, Leung P, Eltahla AA, Grebely J, Dore GJ, et al. Limited naturally occurring escape in broadly neutralizing antibody epitopes in hepatitis C glycoprotein E2 and constrained sequence usage in acute infection. Infect Genet Evol. 2017; 49: 88-96.
36. Keck Zy, Angus AG, Wang W, Lau P, Wang Y, Gatherer D, et al. Non-random escape pathways from a broadly neutralizing human monoclonal antibody map to a highly conserved region on the hepatitis C virus E2 glycoprotein encompassing amino acids 412-423. PLoS Pathogens. 2014; 10(8): e1004297.

Cell J
Cell Journal(Yakhteh) Homepage: https://www.celljournal.org/
Letter to The Editor Vol 25, No 1, January 2023, Pages: 73-75

Healthy Male Individuals Possess Higher Plasma HER-2 Level than Females

Sepand Tehrani Fateh, M.D.[1#], Abbas Behgozin, M.Sc.[2#], Farshid Yekani, Ph.D.[2#], Loabat Geranpayeh, M.D., Ph.D.[3], Asiie Olfatbakhsh, M.D., Ph.D.[4], Shiva Moghadam, M.D., Ph.D.[4], Ramin Sarrami-Forooshani, Ph.D.[5], Amir Salehi-Najafabadi, Ph.D.[2, 6*], Faezeh Shekari, Ph.D.[2, 7*]

1. School of Medicine, Shahid Beheshti University of Medical Sciences, Tehran, Iran
2. R&D Division, Tashkhis Fan Firoozeh (Firoozeh DiaTech), Tehran, Iran
3. Department of Surgery, Sina Hospital, Tehran University of Medical Sciences, Tehran, Iran
4. Breast Diseases Department, Breast Cancer Research Center, Motamed Cancer Institute, ACECR, Tehran, Iran
5. ATMP Department, Breast Cancer Research Center, Motamed Cancer Institute, ACECR, Tehran, Iran
6. Department of Microbiology, School of Biology, University College of Science, University of Tehran, Tehran, Iran
7. Department of Stem Cells and Developmental Biology, Cell Science Research Center, Royan Institute for Stem Cell Biology and Technology, ACECR, Tehran, Iran

#These authors equally contributed to this work.

Corresponding Addresses: P.O.Box: 1956836488, R&D Division, Tashkhis Fan Firoozeh (Firoozeh DiaTech), Tehran, Iran P.O.Box: 16635-148, Department of Stem Cells and Developmental Biology, Cell Science Research Center, Royan Institute for Stem Cell Biology and Technology, ACECR, Tehran, Iran
Emails: amirsalehi@ut.ac.ir, faezehshekari@royaninstitute.org

Received: 19/November/2022, Revised: 19/November/2022, Accepted: 14/December/2022

Abstract

Considering HER2 as one of the well-known biomarkers in the cancer field, and published articles regarding serum levels of HER2, in this paper we tried to highlight the issue that most studies don't stratify the HER-2 concentration of individuals in terms of gender. In this brief survey, healthy individuals with no prior non-communicable diseases were categorized as males (n=34) and females (n=43), and all samples were evaluated for plasma HER-2 levels at once. Surprisingly, the plasma level of HER-2 of healthy male individuals (mean= 2.28 ± 0.21 ng/mL) was significantly (P<0.0001) higher than the plasma level of HER-2 of healthy females (mean: 0.06 ± 0.09 ng/mL), with no overlap. Therefore, we suggest that more studies are required to re-check the cutoff values for HER-2 plasma levels based on gender since the clinical implications of a unique HER-2 cutoff for both genders may be seriously concerning.

Citation: **Fateh ST, Behgozin A, Yekani F, Geranpayeh L, Olfatbakhsh A, Moghadam Sh, Sarami Forroshani R, Salehi-Najafabadi A, Shekari F. Healthy male individuals possess higher plasma HER-2 level than females. Cell J. 2023; 25(1): 73-75. doi: 10.22074/CELLJ.2022.562589.1134.**

The overexpression of human epidermal growth factor receptor 2 (HER-2) has been reported in cancers including breast, gastric, gynecological, prostate, and pancreatic, also other diseases such as diabetes, and coronary artery disease, suggesting assessment of the level of HER-2 as an efficient diagnostic modality. Hence, the measurement of serum or plasma HER-2 level (1-4), along with Immunohistochemistry and Fluorescence In-Situ Hybridization (FISH) techniques is a growing field aimed to secure an accurate and less invasive approach for prognostic, diagnostic, and follow-up purposes. Recently, the importance of HER2-low and ultra-low positivity has been highlighted to transform the traditional binary HER2 scoring system (5-7). Patients with a low or very low level of HER2 expression are candidates for anti-HER2 antibody-drug conjugates therapies (5, 7, 8). It has been shown that the expression of HER-2 is regulated by various factors such as estrogen receptor, estradiol, progesterone, and sex-hormone profile which is expressed differently in males and females (9-13). Consequently, due to the physiological differences in males and females, a gender-related difference in HER-2 expression is expected. Therefore, we aimed to determine the significance of gender, as one of the most effective factors in the plasma level of HER-2.

We systematically searched for the studies from 2000 to 2021 in MEDLINE concerning the serum level of HER-2 or HER-2 ECD (extracellular domain) in different diseases compared to the control group (Supplementary Materials 1 and 2, See Supplementary Online Information at www.celljournal.org). Interestingly, 73.6% of included studies (n=19) were divided neither the patients nor the control group based on their gender regarding the HER-2 or HER-2 ECD serum level. However, a specified cutoff value for serum levels of HER-2 regarding the gender of patients is still undetermined yet of great importance. In this sense, we compared the serum level of HER-2 in healthy males and females. Herein, robust evidence

on the difference in serum levels of HER-2 in males and females is provided.

In this brief survey, healthy individuals with no prior non-communicable diseases were categorized as males (n=34) and females (n=43), and all samples were evaluated with an ELISA for HER-2 level at once (Supplementary material 3, See Supplementary Online Information at www.celljournal.org).

The human real samples were kindly provided by medical diagnostic laboratories of Sina Hospital, Farmanieh Hospital, and Motamed Cancer Institute in accordance with the ethical principles and the national norms and standards for conducting Medical Research in Iran (IR.ACECR.IBCRC.REC.1400.018).

We accepted only samples in ages (the 30 seconds to 50 seconds) with a declaration of absence of other underlying diseases, especially diseases related to the immune system and acute or chronic inflammations, specific systemic diseases (rheumatology, endocrine, cardiovascular, etc.), no chemotherapy or radiotherapy in the last six months, and absence of pregnancy. Surprisingly, the plasma level of HER-2 of healthy male individuals (mean=2.28 ± 0.21 ng/mL) was significantly ($P<0.0001$) higher than the plasma level of HER-2 of healthy females (mean: 0.06 ± 0.09 ng/mL), with no overlap (Fig.1). Although reported very limitedly in few studies (14-16), similar results have not attracted significant attention before, and no further discussion on the underlying causes or implications is provided in the literature.

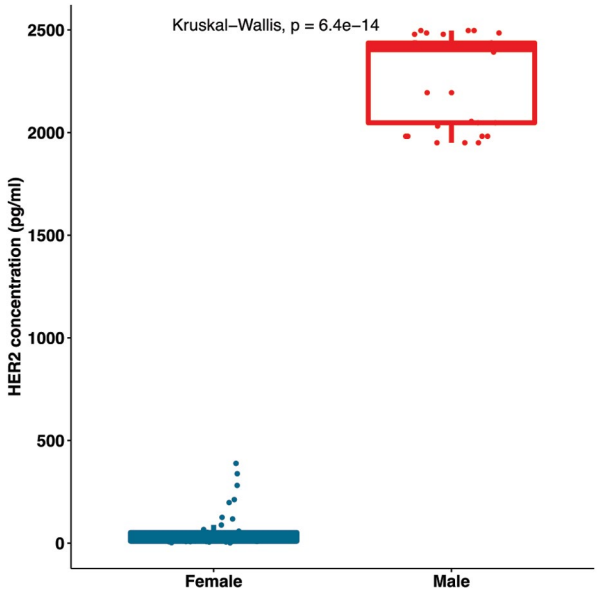

Fig.1: An Illustration of a comparison between serum HER2 level in plasma of healthy males and females (tested by sandwich ELISA procedure using prepared kit (invitrogen).

Clinical implications of the difference in HER-2 level between males and females:

We have observed that HER-2 plasma level is highly gender-related, and in healthy males is approximately 2-2.5 ng/ml, which is roughly 50 fold of the healthy female level. In the case of considering a cutoff value based on the general population, the HER-2 plasma level of perhaps all male individuals, either healthy or diseased one would be higher than the cutoff value; therefore, the prevalence of diseases screened by serum HER-2 may be overestimated in these individuals. The HER-2 plasma level may also differ between males and females in the patients' population; hence, male patients might have higher HER-2 levels due to their higher baseline HER-2 levels. The implications of this issue have been found significant in the interpretation of clinical data in some reports, although neglected by researchers (17-19). Through using average cutoff values, male and female patients might be over-treated and under-treated with HER-2-targeted therapies, respectively. Consequently, we strongly suggest more studies to define gender-specific cutoff values for HER-2 plasma levels in healthy and patient populations.

In conclusion, according to our observation, male individuals may have higher HER-2 plasma levels than females which might arise from the differences in sex hormones in males and females. The cutoff values for HER-2 plasma levels must be defined based on gender since the clinical implications of unique HER-2 cutoff for both genders such as overestimation and underestimation of diseases in males and females and inaccuracy of HER-2-targeted treatments are seriously concerning. However, more critical assessments are needed to find out if there were any nonspecific binding happened or the availability of gender-specific HER isoforms. Moreover, due to our limited group of studies, racial factors might also contribute to the observed difference in HER-2 plasma levels which necessitates similar investigations in other regions: with larger population involved.

Acknowledgments

There is no financial support and conflict of interest in this study.

Authors' Contributions

S.T.F.; Formal analysis, Writing - original draft. A.B, F.Y.; Data curation, Visualization. L.G., A.O., S.M., R.S.F.; Resources, Methodology. A.S.N.; Funding acquisition, and Supervision. F.S.; Conceptualization, Methodology, Supervision. S.T.F., A.B., F.Y., L.G., A.O., S.M., R.S.F., A.S.N., F.S.; Writing - review and editing. All authors read and approved the final manuscript.

References

1. Darlix A, Lamy PJ, Lopez-Crapez E, Braccini AL, Firmin N, Romieu G, et al. Serum HER2 extra-cellular domain, S100ß and CA 15-3 levels are independent prognostic factors in metastatic breast cancer patients. BMC Cancer. 2016; 16: 428.
2. Eppenberger-Castori S, Klingbiel D, Ruhstaller T, Dietrich D, Rufle DA, Rothgiesser K, et al. Plasma HER2ECD a promising test

for patient prognosis and prediction of response in HER2 positive breast cancer: results of a randomized study - SAKK 22/99. BMC Cancer. 2020; 20(1): 114.
3. Lee SB, Lee JW, Yu JH, Ko BS, Kim HJ, Son BH, et al. Preoperative serum HER2 extracellular domain levels in primary invasive breast cancer. BMC Cancer. 2014; 14: 929.
4. Shamshirian A, Aref AR, Yip GW, Ebrahimi Warkiani M, Heydari K, Razavi Bazaz S, et al. Diagnostic value of serum HER2 levels in breast cancer: a systematic review and meta-analysis. BMC Cancer. 2020; 20(1): 1049.
5. Atallah NM, Toss MS, Green AR, Mongan NP, Ball G, Rakha EA. Refining the definition of HER2-low class in invasive breast cancer. Histopathology. 2022; 81(6): 770-785.
6. Corti C, Giachetti PPMB, Eggermont AMM, Delaloge S, Curigliano G. Therapeutic vaccines for breast cancer: Has the time finally come? Eur J Cancer. 2022; 160: 150-174.
7. Venetis K, Crimini E, Sajjadi E, Corti C, Guerini-Rocco E, Viale G, et al. HER2 Low, Ultra-low, and novel complementary biomarkers: expanding the spectrum of HER2 positivity in breast cancer. Front Mol Biosci. 2022; 9: 834651.
8. Ferraro E, Drago JZ, Modi S. Implementing antibody-drug conjugates (ADCs) in HER2-positive breast cancer: state of the art and future directions. Breast Cancer Res. 2021; 23(1): 84.
9. Ajayi O, Charles-Davies M, Anetor J, Ademola A. Pituitary, gonadal, thyroid hormones and endocrine disruptors in pre and postmenopausal nigerian women with ER-, PR- and HER-2-positive and negative breast cancers. Med Sci (Basel). 2018; 6(2): 37.
10. Bagli L, Dittadi R, Zancan M, Panzini I, Monti F, Ravaioli A. HER-2/neu serum levels and menopausal status. Int J Biol Markers. 2001; 16(1): 69-70.
11. Miller S, Hung M. Regulation of her2/neu gene-expression (review). Oncol Rep. 1995; 2(4): 497-503.
12. Phipps AI, Malone KE, Porter PL, Daling JR, Li CI. Reproductive and hormonal risk factors for postmenopausal luminal, HER-2-overexpressing, and triple-negative breast cancer. Cancer. 2008; 113(7): 1521-1526.
13. Read LD, Keith D Jr, Slamon DJ, Katzenellenbogen BS. Hormonal modulation of HER-2/neu protooncogene messenger ribonucleic acid and p185 protein expression in human breast cancer cell lines. Cancer Res. 1990; 50(13): 3947-3951.
14. Di Gioia D, Dresse M, Mayr D, Nagel D, Heinemann V, Kahlert S, et al. Serum HER2 supports HER2-testing in tissue at the time of primary diagnosis of breast cancer. Clin Chim Acta. 2014; 430: 86-91.
15. Fernández-Real JM, Menendez JA, Frühbeck G, Moreno-Navarrete JM, Vazquez-Martín A, Ricart W. Serum HER-2 concentration is associated with insulin resistance and decreases after weight loss. Nutr Metab (Lond). 2010; 7: 14.
16. Späth F, Andersson U, Dahlin AM, Langseth H, Hovig E, Johannesen TB, et al. Pre-diagnostic serum levels of EGFR and ErbB2 and genetic glioma risk variants: a nested case-control study. Tumour Biol. 2016; 37(8): 11065-11072.
17. Al-Saad S, Al-Shibli K, Donnem T, Andersen S, Bremnes RM, Busund LT. Clinical significance of epidermal growth factor receptors in non-small cell lung cancer and a prognostic role for HER2 gene copy number in female patients. J Thorac Oncol. 2010; 5(10): 1536-1543.
18. Sui F, Sun W, Su X, Chen P, Hou P, Shi B, et al. Gender-related differences in the association between concomitant amplification of AIB1 and HER2 and clinical outcomes in glioma patients. Pathol Res Pract. 2018; 214(9): 1253-1259.
19. Wang HB, Liao XF, Zhang J. Clinicopathological factors associated with HER2-positive gastric cancer: A meta-analysis. Medicine (Baltimore). 2017; 96(44): e8437.